Transverse Emittance Measurements and Optimization for a Superconducting RF Photo Injector

Dissertation

zur Erlangung des Doktorgrades

an der Fakultät für Mathematik, Informatik und Naturwissenschaften

Fachbereich Physik

der Universität Hamburg

vorgelegt von

Shuai Ma

Hamburg
2022

Gutachter der Dissertation:	Prof. Dr. Wolfgang Hillert
	Dr. Jochen Teichert
Zusammensetzung der Prüfungskommission:	Prof. Dr. Sven-Olaf Moch
	Prof. Dr. Wolfgang Hillert
	Prof. Dr. Wolfgang Parak
	Dr. Jochen Teichert
	Dr. Mikhail Krasilnikov
Vorsitzende/r der Prüfungskommission:	Prof. Dr. Sven-Olaf Moch
Datum der Disputation:	29.11.2022
Vorsitzender des Fach-Promotionsausschusses PHYSIK:	Prof. Dr. Wolfgang J. Parak
Leiter des Fachbereichs PHYSIK:	Prof. Dr. Günter H. W. Sigl
Dekan der Fakultät MIN:	Prof. Dr. -Ing. Norbert Ritter

Abstract

As one of the most promising continuous wave (CW) injectors for high brightness electron beams, ELBE superconducting radio-frequency (SRF) gun has been developed and optimized. This gun can provide beams with good quality for the ELBE user facility. One important aspect is to measure the transverse emittance accurately and efficiently. This thesis contributes to the progress in this field and focuses on measuring and optimizing the transverse emittance for ELBE SRF gun. The slit-scan, quadrupole scan, and an advanced thermal emittance measurement method, called single shot cathode transverse momentum imaging, have been studied and applied at this SRF gun.

A fast slit-scan emittance measurement system consisting of a continuously moving slit and a yttrium aluminium garnet (YAG) screen has been developed. During the beamlet image processing, the machine learning (ML) algorithms have been integrated in order to improve the signal-to-noise ratio effectively. This is the first time to successfully apply the ML in such diagnostic methods. The measurement speed is improved about ten times and accuracy is also better than before. The errors of slit-scan emittance measurement, arising from slit position, beamlet intensity, center position and root mean square (RMS) width uncertainties, have been analyzed. The quadrupole scan emittance measurement method has been studied too. The influence of the space charge effect on quadrupole scan results has been revealed. The error of the quadrupole scan measurement has also been analyzed.

To compensate the transverse emittance due to space charge effect, a superconducting (SC) solenoid is placed as close as possible to the exit of the SRF cavity. Another important part in this thesis is the investigation and optimization of the SC solenoid. The spherical aberration of the SC solenoid has been analyzed. In order to decrease it, a new yoke geometry of SC solenoid for the next generation SRF gun has been designed. The multipole transverse field modes of the solenoid caused by an axis tilt have bean analyzed by means of simulations and experimental investigations using a formalism fitting method. The influences of the multipole modes, especially the quadrupole and sextupole fields on transverse emittance have been calculated. A pair of a normal quadrupole and a skew quadrupole, called correctors, have been adopted to compensate the influence of the quadrupole field on the emittance.

The cathode intrinsic emittance can contribute a non-negligible part to the transverse emittance. So in this thesis the cathode intrinsic emitttance is measured too. The single shot transverse momentum imaging method has been used to measure the cathode intrinsic emittance. A further advantage is that this method allows to determine the transverse momentum locally at different positions on the cathode.

Kurzfassung

Supraleitende Hochfrequenz-Elektronenquellen (SRF) stellen ein besonderen Typ der Elektroneninjektoren für die Erzeugung von Elektronenstrahlen mit hoher Brillanz dar, die ausserdem im kontinuierlichen Modus (CW) betrieben werden können. Eine solche SRF Gun mit hoher Brillanz bietet das Helmholtz Zentrum Dresden Rossendorf (HZDR) für den Nutzerbetrieb an. Ein wichtiger Aspekt ist die genaue und effiziente Messung der transversalen Emittanz. In dieser Arbeit werden daher Messungen an Slit-Scan und Quadrupol-Scan durchgeführt. Ebenso wird ein neuartiges Verfahren zur Messung der thermischen Emittanz an der HZDR SRF Gun, die so genannte Single-Shot-Transversalimpulsmessung, untersucht.

Ein schnelles und verbessertes Slit-Scan-Emittanzmesssystem, das auf einem sich kontinuierlich bewegenden Spalt und einem Leuchtschirm aus Yttrium-Aluminium-Granat (YAG) basiert, wurde im Rahmen dieser Arbeit entwickelt. Dafür wurde erstmals ein künstlichen Intelligenz (Machine learning) Alghorithmus in der Bildverarbeitung dieser Messmethode angewendet um Effizienz und Genauigkeit zu erhöhen. Der Gesamtfehler der Slit-Scan-Emittanzmessung, der sich aus den Fehlern der Position des Messspalts, der Beamlet-Intensität, der Mittelposition und der quadratischen Mittelwertsbreite (RMS) ergibt, wurde ebenfalls ermittelt. Bei diesem Verfahren werden die Einflüsse von Spaltbreite und Raumladungseffekt auf die Emittanz bewertet. Das Quadrupol-Scan-Emittanz-Messverfahren wurde zusätzlich untersucht und der Einfluss des Raumladungseffekts auf dessen Ergebnisse wurden diskutiert. Basierend auf einem magnetischen Strahlkorrektur und einem YAG-Bildschirm wurde eine einfache Methode zur Kalibrierung der Quadrupolstärke erfolgreich angewendet. Auch hier wurde der Messfehler des Quadrupolscans erfasst und analysiert.

Ein wichtiges Bauteil für die Verbesserung der transversalen Emittanz repräsentiert die supraleitende (SC) Solenoid-Linse. Ein zentraler Teil der Dissertation ist die Untersuchung und Optimierung dieses Solenoids. Dessen Öffnungsfehler wurde gefunden und daraufhin wurde eine öffnungsverkleinerung durch die Optimierung der Eisenjochgeometrie durchgeführt. Mit Hilfe von Computersimulation und experimentellen Messungen wurden die transversalen Multipolfelder mit einer neuen Methode ermittelt und ausgewertet. Die Ursache der Multipolfelder ist eine verkippte Mittelachse des Solenoids. Der Einfluss der Multipolkomponenten, insbesondere der Quadrupol- und Hexapolfelder, auf die transversale Emittanz wurden erfolgreich untersucht. Um den ungewünschten, negativen Effekt des Solenoids zu kompensieren, wird ein Quadrupol-Korrektorpaar, welches aus einem normalen und einem um 45° verdrehten Quadrupol besteht, angewendet.

Die Kathodeneigenstrahlung trägt einen erheblichen Teil zur Queremission bei und wird im Rahmen dieser Arbeit ebenfalls ermittelt und gemessen. Um die Strahlemittanz bei niedriger Pulsladung und die intrinsische Emittanz zu messen, wurde die Single-Shot-Transversalimpulsmessung angewandt. Der Transversalimpuls lässt sich mit dieser geeigneten Methode an unterschiedlichen Stellen auf der Kathode lokalisieren und bestimmen, welches ein bedeutender Vorteil dieser Methode ist.

Contents

List of figures

List of tables

Chapter 1

Introduction

Since the concept of synchrotron was first developed by Ed McMillian and Vladimir Veksler in 1945 [1, 2], dedicated synchrotron facilities have been built to generate tunable beams of electromagnetic radiation from the far infrared (IR) to the hard x-ray range. As a standard value to evaluate the quality of the synchrotron facility, the term brilliance is defined as

$$\text{Brilliance} = \frac{\text{photons/second}}{(\text{mm}^2 \text{ source area})(\text{mrad})^2(0.1\% \text{ bandwidth})} \tag{1.1}$$

giving the number of photons per second per unit bandwidth (0.1 %) passing through a unit source area and unit solid angle [3]. The analogous figure of merit for charged particle beams is [4]

$$\text{Brightness} \propto \frac{I_p}{\varepsilon_x \varepsilon_y}, \tag{1.2}$$

where I_p is the peak current of the beam, ε_x and ε_y are the beam emittances in the transverse planes and will be defined in section 2.2 of this thesis. People pursue the high brightness and coherence synchrotron radiation sources, because they provide outstanding tools to probe the structures and properties of materials with extreme precision in time and spatial resolution [5]. Four generations of radiation sources have been developed during the last several decades, increasing the peak brilliance from 10^{13} B.U. (B.U. = Brilliance unit = photons/s/mm^2/mrad^2/0.1% BW) on the basis of storage rings to 10^{33} B.U. based on free electron lasers (FEL) [6, 7, 8, 9, 10].

The FEL is based on a linear accelerator applying the interaction between the relativistic electron beam and the radiation field as the beam is passing through a periodic magnetic structure [11], and has transverse coherence, and extremely high temporal coherence. Generally, the linac-based FELs consist of an electron injector, the main linear accelerator with bunch compressors, and the undulators or wigglers. It is known that the emittance and bunch charge play a critical role in FELs to increase the brightness. Additionally, from uncertainty principle, the minimally achievable radiation wavelength, λ_{min}, has a limitation coming from the beam transverse normalized emittance, ε_n, as $\varepsilon_n \leq \lambda_{min}\gamma/(4\pi)$ [12, 13]. Here, for a good interaction of electron and photon beams it is required that the emittance of both beams are equal, and the emittance of the diffraction limited laser beam has been calculated from the uncertainty principle. However, the normalized emittance can not decrease in the accelerator from the

injector to the end. It will stay as a constant if the beam has a reversible process, or increase if the beam goes through an irreversible process [14]. So an excellent electron injector with high bunch charge and low emittance is necessary for FELs.

At present, direct current (DC) guns , normal conducting radio frequency (NCRF) guns and superconducting radio frequency (SRF) guns are the main candidates for electron injectors of FEL facilities. The DC gun can work in a reliable CW mode with high average current, up to 65-75 mA [15, 16, 17]. But the limitation is the DC voltage applied to the acceleration gap, up to 500 kV [18], which limits the electric field on the cathode and causes a faster beam emittance growth compared with higher fields. Compared to DC gun, the NCRF gun has a better performance, i.e. higher peak current, up to 100 A, higher beam energy, and lower emittance for given bunch charge [19]. But due to the ohmic wall losses in NC cavities, the water cooling limits the average RF power used for acceleration. The gun can only work at a low duty-cycle pulsed mode or at lower gradient in CW mode, ~ 0.8 MeV beam energy at gun exit [20]. The SRF gun has significant lower RF losses in the cavity, which means that this gun has the potential to operate at a high duty-cycle or CW mode with high accelerating gradient, so that it has the ability to provide beams with high bunch charge [21]. However, the SRF gun also has some challenges, such as the cavity processing, high quantum efficiency (QE) and long lifetime photocathodes, and the risk of cavity contamination [22, 23, 24]. To reduce the risk of cavity contamination and the cathode cooling problem in SC cavities, the hybrid gun, DC-SRF gun, has been developed. But in this gun the limitation is still the DC voltage [24, 25].

Located at Helmholtz-Zentrum Dresden-Rossendorf (HZDR) the radiation source ELBE operates a linac-based FEL radiation center. This user facility is open for international researchers and provides multiple secondary beams, both electromagnetic radiation and particles. The ELBE linac can operate in reliable CW mode for high average output power with two superconducting linac modules. It has two CW electron sources, a thermionic DC gun [26] and a SRF gun [27]. The DC gun operating at 235 kV voltage delivers beams with bunch charges up to 77 pC (maximum 100 pC) at 13 MHz repetition rate and about 450 ps length serving for the IR-FELs and other radiation production. The transverse normalized emittance is 10 mm $\cdot$ mrad in this operating case. However, some new challenging applications, for instance, the neutron time-of-flight experiments [28], high power THz experiments [29] and Thomson backscattering experiments [30] require beams with higher bunch charge. The advantage of a higher bunch charge is an improved signal-to-noise ratio and an increased intensity of the secondary radiation. For that reason the SRF gun has been developed and is now routinely applied for user operations at ELBE delivering bunches with up to 250 pC charge.

To improve the performance of the SRF gun, many efforts have been done in various fields: the cathode QE and lifetime, laser distribution and stability, RF stability, solenoid emittance compensation, and user beamline transport [27, 31, 32, 33, 34]. However, to access to a better performance and beam quality, besides the former work, the beam transverse emittance optimization is urgent. An effective and accurate emittance measurement and data analysis system is needed. Further studies of solenoid fields and their influence on emittance are necessary. A reliable intrinsic emittance map is helpful for the cathode research at the SRF gun.

In this thesis, the beam transverse emittance is optimized further from decreasing the SC solenoid spherical aberration, and correcting the multipole fields from the solenoid, especially

the quadrupole field. A fast slit-scan transverse emittance measurement system is built. To improve the accuracy and efficiency of the beamlet images processing, two algorithms based on machine learning are applied. The traditional method, quadrupole scan, is also analyzed. The single shot transverse momentum imaging is adopted to map the cathode intrinsic emittance.

The thesis is organized as the followings. Chapter 2 will introduce the basic linear concepts in accelerator physics. The main emittance sources are analyzed in this chapter. An overview of the SRF gun-II photo injector, including the cavity, cryomodule, RF system, cathodes, laser system and the diagnotic beamline is given in Chapter 3. The topics about the SC solenoid field aberrations including spherical aberration and multipole fields are analyzed in Chapter 4. The influence of spherical aberration and multipole fields from the SC solenoid on the transverse emittance is analyzed. To decrease the influence of spherical aberration, a new SC solenoid by extending the yoke and radius is designed. Additionally, a compact and reliable measurement method of solenoid fields and the simulation of this method in Comsol Multiphysics are given in this chapter. Three transverse emittance measurement methods, including quadrupole scan, slit-scan, and single shot transverse momentum imaging for the cathode intrinsic emittance measurements will be analyzed in theory and simulations in Chapter 5, and the experiment results will be given in Chapter 6. In the end, Chapter 7 will give the conclusions and outlook.

Chapter 2

Theory

2.1 Linear beam dynamics of charged particles

In a 3-D space, we need a 6-D phase space, $(x, \dot{x}, y, \dot{y}, z, \dot{z})$, to describe the motion of one electron, which is determined by Newton's second law as well known. Here the dot means the first derivative with respect to time. However, in accelerator physics one prefers to use a coordinate system which is easily adopted to the requirements of the design and analysis of particle accelerator systems. Thereby the z coordinate is in beamline direction, whereas x and y describe the transversal ones. Furthermore a central or reference trajectory and a reference particle with the momentum p_0 is defined. In a curved beamline this coordinate system is moving so that the z component is always the tangent of the reference trajectory. In these accompanying coordinates the motion of a particle is given by the vector

$$\mathbf{X} = \begin{pmatrix} x \\ x' \\ y \\ y' \\ \Delta z \\ \delta \end{pmatrix}, \tag{2.1}$$

where $x' = p_x/p_0$, $y' = p_y/p_0$ and $\delta = \Delta p/p_0$. Δp is the individual particle momentum difference from p_0, and Δz specifies the relative z position with respect to the reference particle.

In this thesis the focus will be on the examination of the transverse particle dynamics. It will be assumed that the transverse and longitudinal motions are independent, which allows us to reduce the vector in Eq. 2.1 to four components in the further treatment. If there is no coupling between x and y, the two directions can be considered separately and the complexity can be further reduced.

The motion of charged particles in electromagnetic fields results from the Lorentz force. For an electron the Lorentz force can be written as

$$\vec{F} = e\vec{E} + e(\vec{v} \times \vec{B}), \tag{2.2}$$

where e is the electrical charge, $\vec{v}$ is the electron velocity vector, $\vec{E}$ and $\vec{B}$ are the electric field vector and the vector of the magnetic flux density, respectively. Assuming there is no electric field (such as no cavity), and only a magnetic field with components in the transverse plane, then the equation of motion is

$$m_0\gamma v^2\vec{\kappa} + e(\vec{v}\times\vec{B}) = 0, \tag{2.3}$$

where γ is the Lorentz factor, m_0 is the electron rest mass, and $\vec{\kappa} = (\kappa_x, \kappa_y, 0)$ is the local curvature vector of the trajectory with

$$\kappa_{x,y} = \frac{1}{\rho_{x,y}}, \tag{2.4}$$

where $\rho_{x,y}$ is the local bending radius of the trajectory. In the orthogonal coordinate system, $\vec{B} = (B_x, B_y, 0)$ and for linear beam dynamics, only the zero and the first order of the magnetic fields are considered, such as:

$$\begin{aligned} B_x &= -B_{x0} + gy + O(2) \\ B_y &= B_{y0} + gx + O(2), \end{aligned} \tag{2.5}$$

where B_{y0} and B_{x0} are the dipole fields in horizontal and vertical directions, respectively, and g denotes the field gradient of normal quadrupole. Then with $p = \gamma m_0 v$

$$\begin{aligned} \kappa_x &= \frac{e}{p}B_y = \kappa_{0x} + kx + O(2) \\ \kappa_y &= -\frac{e}{p}B_x = \kappa_{0y} - ky + O(2). \end{aligned} \tag{2.6}$$

So the equations of motion in the transverse directions can be obtained:

$$u'' = -(1 + \kappa_{0u}u)\kappa_u + \kappa_0, \tag{2.7}$$

where u represents x or y, κ_{0u} is κ_{0x} or κ_{0y}, κ_u is the given as κ_x or κ_x. Combining the equations above and ignoring the high order terms, linear equation of motion or Hill equation is

$$u'' + Ku = 0, \tag{2.8}$$

where $K = k + \kappa_{0x}^2$ or $K = -(k - \kappa_{0y}^2)$, named the focusing function. This is a linear differential equation and the solutions can be written as:

$$\begin{bmatrix} u(z) \\ u'(z) \end{bmatrix} = \mathrm{M}(z \mid 0) \begin{bmatrix} u_0 \\ u_0' \end{bmatrix}, \tag{2.9}$$

$$\mathrm{M}(z \mid 0) = \begin{cases} \begin{bmatrix} \cos\sqrt{K}z & \frac{\sin\sqrt{K}z}{\sqrt{K}} \\ -\sqrt{K}\sin\sqrt{K}z & \cos\sqrt{K}z \end{bmatrix}, & K > 0,\ \text{focusing} \\ \begin{bmatrix} 1 & z \\ 0 & 1 \end{bmatrix}, & K = 0,\ \text{drift space} \\ \begin{bmatrix} \cosh\sqrt{-K}z & \frac{\sinh\sqrt{-K}z}{\sqrt{-K}} \\ \sqrt{-K}\sinh\sqrt{-K}z & \cosh\sqrt{-K}z \end{bmatrix}, & K < 0,\ \text{defocusing} \end{cases} \tag{2.10}$$

In the beamline, different elements have different matrices and their impact on the beam can be obtained by multiplication with these matrices. This method is very efficient and widely used in the beam transport analysis and design. There exists a strong condition that the determinant of the matrix is equal to one. This is a property coming from Eq. 2.8. Assuming that two independent solutions $u_1(z)$ and $u_2(z)$ of Eq. 2.8 form the Wronskian

$$W(z) \equiv u_1 u_2' - u_2 u_1'. \tag{2.11}$$

$W(z)$ is a constant because of $W(z)' = 0$. Performing a little expansion of Eq. 2.9:

$$\begin{bmatrix} u_1 & u_2 \\ u_1' & u_2' \end{bmatrix}_z = \mathrm{M}\left(z \mid z_0\right) \begin{bmatrix} u_1 & u_2 \\ u_1' & u_2'. \end{bmatrix}_{z_0} \tag{2.12}$$

and calculating the determinant on both sides of this equation, then $\det(W(z)) = \det(W(z_0))$ and

$$\det(\mathrm{M}) = 1, \tag{2.13}$$

because $W(z)$ is constant. The reason is that Eq. 2.8 satisfies the symplectic condition in mathematics [35]. This rule is essential, and will be discussed again in the next section dealing with the emittance concept.

2.2 Courant-Snyder formalism and emittance

In the Hill Eq. 2.8, the focusing function $K(z)$ is assumed to be a periodic function. In this case a solution can be written as:

$$u(z) = \sqrt{\varepsilon\beta(z)}\cos\left(\theta(z) + \theta_0\right). \tag{2.14}$$

This equation is the widely used Courant-Snyder formalism, and the parameters in it have their physical meanings: $\beta(z)$ is related to the amplitude of u at position z, and $\theta(z)$ is the phase function. The quantity ε is a constant and can be calculated from the initial condition. When Eq. 2.14 is inserted in Eq. 2.8, one obtains:

$$\begin{aligned} \frac{1}{2}\left(\beta\beta'' - \frac{1}{2}\beta'^2\right) - \beta^2\theta'^2 + \beta^2 K = 0, \\ \beta'\theta' + \beta\theta'' = 0. \end{aligned} \tag{2.15}$$

From Eq. 2.15, it is obvious that $\beta'\theta' + \beta\theta'' = (\beta\theta')'$, and then

$$\beta\theta' = constant. \tag{2.16}$$

Let us normalize this constant to be 1, and θ can be obtained from the $\beta(z)$ function:

$$\theta(z) = \int_0^z \frac{dz'}{\beta\left(z'\right)}. \tag{2.17}$$

It gives a method to determine the phase advance along the beamline at local position z and also the local betatron oscillation wavelength is obtained by $2\pi\theta(z)$. When we use Eq. 2.16 in

the first Eq. 2.15, it shows that $\beta(z)$ is only related to K and can be determined from

$$\frac{1}{2}\beta\beta'' - \frac{1}{4}\beta'^2 + \beta^2 K = 1. \tag{2.18}$$

Return to Eq. 2.14, the first derivative is

$$u' = \frac{1}{2}\beta'\frac{\sqrt{\varepsilon}}{\sqrt{\beta}}\cos(\theta+\theta_0) - \sqrt{\frac{\varepsilon}{\beta}}\sin(\theta+\theta_0). \tag{2.19}$$

Then these two functions are defined as:

$$\begin{aligned} \alpha &= -\frac{1}{2}\beta' \\ \gamma &= \frac{1+\alpha^2}{\beta}. \end{aligned} \tag{2.20}$$

One notes that $\beta\cdot\gamma - \alpha^2 = 1$. Combining Eq. 2.15 and Eq. 2.19, one can obtain:

$$u^2 + (\beta u' + \alpha u)^2 = \varepsilon\beta \tag{2.21}$$

or equivalently

$$\gamma u^2 + 2\alpha u u' + \beta u'^2 = \varepsilon. \tag{2.22}$$

The quantities β, α, and γ are named as Courant-Snyder parameters or the Twiss parameters. It is clear that the Eq. 2.22 is an ellipse function in the (u, u') plane and the area of this ellipse is defined as ε, named as emittance:

$$\int_{\text{ellipse}} \mathrm{d}u\ \mathrm{d}u' = \pi\varepsilon. \tag{2.23}$$

There is another way to derive Eq. 2.22, which is from the continuity equation in phase space. Ref. [36] gives further information of this method.

In phase space, according to Liouville's Theorem [35], the volume in 6-D phase space, together with all the particles contained in the volume, is a constant. In transverse phase space, i.e. in the 4-D phase space (x, x', y, y'), the emittance is a constant. The emittance conservation is ensured by Eq. 2.13 during the evolution of the beam along the beamline. However, in (x, x', y, y') the transport matrix is a 4-D matrix rather than a 2-D matrix. The emittance in 4-D phase space is conserved if and only if the determinant of the whole matrix is one. As the particles move, the shape of their ellipse evolves, but the emittance remains constant. Fig. 2.1 shows the ellipse in phase space with the coresponding Courant-Snyder parameters.

To compare the emittance of a beam with changing energy, the emittance can be replaced by the normalized emittance, which is defined as

$$\varepsilon_n = \frac{p_0}{m_0 c}\varepsilon, \tag{2.24}$$

and is independent of energy. c is the speed of the light.

In linear beam dynamics, the particles motion is determined by ε and start phase θ_0. Considering a normalized particle distribution of (u, u'), which has a uniform distribution of θ_0 and Gaussian

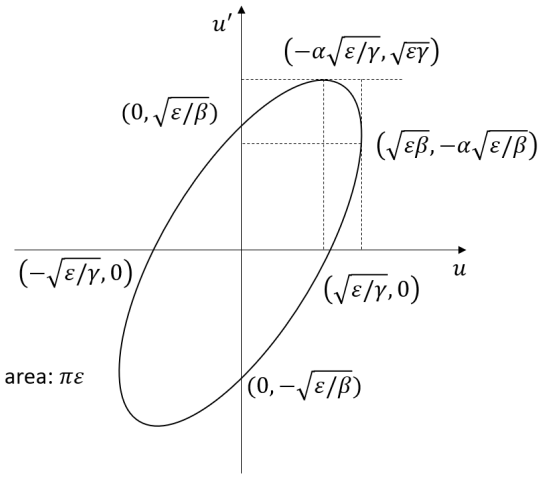

Fig. 2.1 Phase space ellipse. u and u' are x and x' or y and y'. ε is the beam geometric emittance, α, β and γ are the Twiss parameters as the former definitions.

distribution in (u, u'):

$$\begin{aligned}\Psi(u,u') &= \frac{1}{2\pi\varepsilon_{\mathrm{rms}}}\exp\left(-\frac{\varepsilon}{2\varepsilon_{\mathrm{rms}}}\right)\\ &= \frac{1}{2\pi\varepsilon_{\mathrm{rms}}}\exp\left(-\frac{\gamma u^2+2\alpha uu'+\beta u'^2}{2\varepsilon_{\mathrm{rms}}}\right)\\ &= \frac{1}{2\pi\varepsilon_{\mathrm{rms}}}\exp\left[-\frac{u^2+(\alpha u+\beta u')^2}{2\beta\varepsilon_{\mathrm{rms}}}\right],\end{aligned} \tag{2.25}$$

here ε_{rms} is named beam RMS emittance, and

$$\int_{-\infty}^{\infty}\int_{-\infty}^{\infty} dudu'\Psi(u,u') = 1. \tag{2.26}$$

Then one can calculate the second moments of this distribution and obtains:

$$\begin{aligned}\left\langle u^2\right\rangle &= \int_{-\infty}^{\infty}\int_{-\infty}^{\infty} dudu'u^2\Psi(u,u') = \beta\varepsilon_{\mathrm{rms}}\\ \left\langle uu'\right\rangle &= \int_{-\infty}^{\infty}\int_{-\infty}^{\infty} dudu'uu'\Psi(u,u') = -\alpha\varepsilon_{\mathrm{rms}}\\ \left\langle u'^2\right\rangle &= \int_{-\infty}^{\infty}\int_{-\infty}^{\infty} dudu'u'^2\Psi(u,u') = \gamma\varepsilon_{\mathrm{rms}},\end{aligned} \tag{2.27}$$

where the $\langle\ \rangle$ is the average over the distribution. So:

$$\varepsilon_{rms}^2 = \left\langle u^2\right\rangle\left\langle u'^2\right\rangle - \left\langle uu'\right\rangle^2. \tag{2.28}$$

The average of ε is:

$$\begin{aligned}\langle\varepsilon\rangle &= \int_{-\infty}^{\infty}\int_{-\infty}^{\infty} dudu'\varepsilon\Psi\left(u,u'\right) \\ &= \gamma\left\langle u^2\right\rangle + 2\alpha\left\langle uu'\right\rangle + \beta\left\langle u'^2\right\rangle \\ &= 2\varepsilon_{\mathrm{rms}}.\end{aligned} \tag{2.29}$$

The beam RMS emittance is the half of the average beam emittance. Defining $\sigma_u = \sqrt{\langle u^2\rangle}$ as the beam envelope and apply this in Eq. 2.22 yields:

$$\frac{d^2\sigma_u(z)}{dz^2} + K(z)\sigma_u(z) = \frac{\varepsilon_{\mathrm{rms}}^2}{\sigma_u^3(z)}. \tag{2.30}$$

This is the first order beam envelope equation ignoring the no-linear factors influence. One can define $\sigma_{11} = \langle u^2\rangle$, $\sigma_{12} = \langle uu'\rangle$, and $\sigma_{22} = \langle u'^2\rangle$. The covariance matrix of the beam in transverse phase space can be presented as:

$$\Sigma_{rms} = \begin{bmatrix} \sigma_{11} & \sigma_{12} \\ \sigma_{12} & \sigma_{22} \end{bmatrix} = \varepsilon_{rms}\begin{bmatrix} \beta & -\alpha \\ -\alpha & \gamma \end{bmatrix}. \tag{2.31}$$

From the definition of an ellipse in n-dimensions [36], and combining Eq. 2.22 with Eq. 2.9, finds that the evolution of the matrix Σ_{rms} from P_0 to P_1 can be calculated by:

$$\Sigma_{1,rms} = \mathrm{M}\Sigma_{0,rms}\mathrm{M}^T, \tag{2.32}$$

where M is the transport matrix from P_0 to P_1 and the superscript T means the transposed matrix. Although the treatment here is in 2-D, it can be extended to 4-D and 6-D treatments in linear beam dynamics.

2.3 Emittance sources in photo injectors

As discussed in the former section, the beam emittance is a conserved quantity in linear beam dynamics. However, after the photoelectrons are emitted from a cathode, the beam emittance increases during traveling through the injector due to non-linear effects. Fig. 2.2 shows the sources and process of emittance generation from the cathode through the injector [37].

This section gives an overview of the main sources of beam emittance growth in a photo injector. All components of the photo injectors, e.g. the photocathode, the RF cavity, as well as the gun solenoid, contribute. In this process, from the physical processes six main sources can be identified:

- cathode intrinsic emittance,
- RF field emittance,
- rough surface emittance
- space charge emittance,
- beam momentum spread emittance,

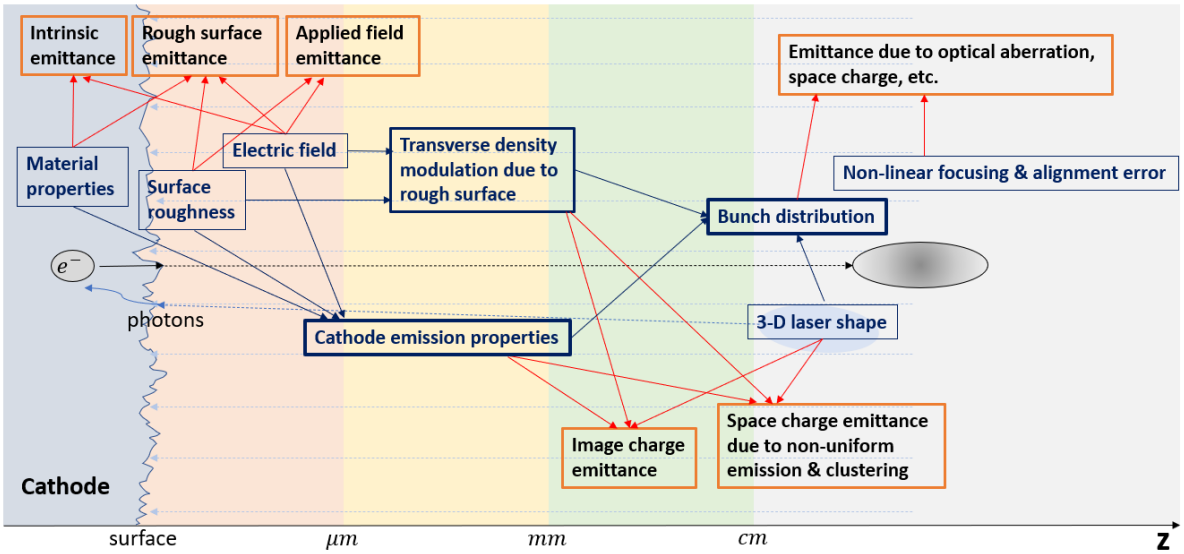

Fig. 2.2 Emittance evolution from the cathode through the photo injector. In the cathode, the material properties and the outside electric field determine the intrinsic emittance. Adding the surface roughness, it generates the rough surface emittance. Outside the cathode, the surface roughness and the modulated electric field causes the applied field emittance. In the range of micrometers to the millimeters from the surface, two more additional emittance contributions, such as the image charge emittance and the space charge emittance due to non-uniform emission and clustering, are generated influenced by the cathode emission properties, the transverse density modulation the rough surface, and the 3D laser shape. Also the bunch distribution is influenced by the transverse density modulation, the cathode emission properties, and the 3D laser shape. In the further range, of millimeters and beyond, the emittances due to optical aberrations, space charge and due to other effects arise and are determined by the bunch distribution, the non-linear focusing and alignment errors.

- solenoid aberrations and multipole fields induced emittance.

The first four sources will be discussed in detail in this section. The last two belong to the main investigations of this thesis and will be analyzed in detail in the Chapters 3 to 5.

2.3.1 Cathode intrinsic emittance

There are several methods to generate electrons from a cathode, such as thermionic emission [38], field-emission [39], and photo emission [40]. In a photo injector like the ELBE SRF gun the photo emission process is used, and the beam is generated from a metal (such as Cu, Mg) or semiconductor material (such as Cs_2Te) driven by an ultraviolet (UV) laser. The interaction of the laser with the cathode material and the electron emission process can be described in three steps, named Spicer's three-step model [40]. In this model, the first step is the photon absorbtion by electrons and the electrons jump into high-energy states. Then, the electrons at high-energy states move to the material surface. The last step is that the electrons escape into the vacuum if their energy is high enough. The effective work function depends on the material work function and its reduction by the Schottky effect due to the external field. At the cathode

surface the normalized emittance ε_n has no correlation term:

$$\varepsilon_n = \frac{1}{m_0 c}\sqrt{\langle x^2\rangle \langle p_x^2\rangle - \langle x p_x\rangle^2} = \sigma_x \frac{\sqrt{\langle p_x^2\rangle}}{m_0 c}. \tag{2.33}$$

We can define the dimensionless RMS momentum

$$\sigma_{p_x} = \frac{\sqrt{\langle p_x^2\rangle}}{m_0 c}, \tag{2.34}$$

then the normalized emittance becomes

$$\varepsilon_n = \sigma_x \sigma_{p_x}. \tag{2.35}$$

In theory, σ_{p_x} can be calculated for a metal as [41]:

$$\sigma_{p_x} = \sqrt{\frac{\hbar\omega - \phi_{\text{eff}}}{3 m_0 c^2}}, \tag{2.36}$$

where $\hbar\omega$ is the energy of the photons, and ϕ_{eff} is the effective work function.

2.3.2 RF emittance

In a RF cavity, the longitudinal electric field accelerates the electrons, whereas the electric radial component and the magnetic azimuthal component cause transverse forces on the electrons. Thereby the strongest contribution comes from the electric field at the cavity irises. Especially the exit iris acts as a strong defocusing lens. The time-dependence of the RF field causes different defocusing of the individual slices in the electron bunch and therefore increases the projected emittance by [37, 42]:

$$\Delta\varepsilon_{n,rf} = \frac{eE_{rf}}{2m_0c^2}\sigma_x^2\sigma_\phi\sqrt{\cos^2\phi_e + \frac{\sigma_\phi^2}{2}\sin^2\phi_e}, \tag{2.37}$$

where E_{rf} is the peak electric field of the cavity on axis and ϕ_e is the relative phase of the electron and the RF waveform when the electron arrives the exit of the cavity. σ_x and σ_ϕ are the beam RMS size and the bunch length in radian unit.

2.3.3 Rough surface emittance

The practical cathodes have bumps and hollows on the surface rather than smooth surface. These micro structures destroy the uniformity of the applied electric field on the cathode, and increase the local field enhancement factor and introduce the unexpected transverse field. The additional emittance resulting from these factors is the cathode rough surface emittance, evaluated as [43]:

$$\Delta\varepsilon^E_{roughness} = \sigma_{laser}\sqrt{\frac{X_g E}{3m_0c^2}}, \tag{2.38}$$

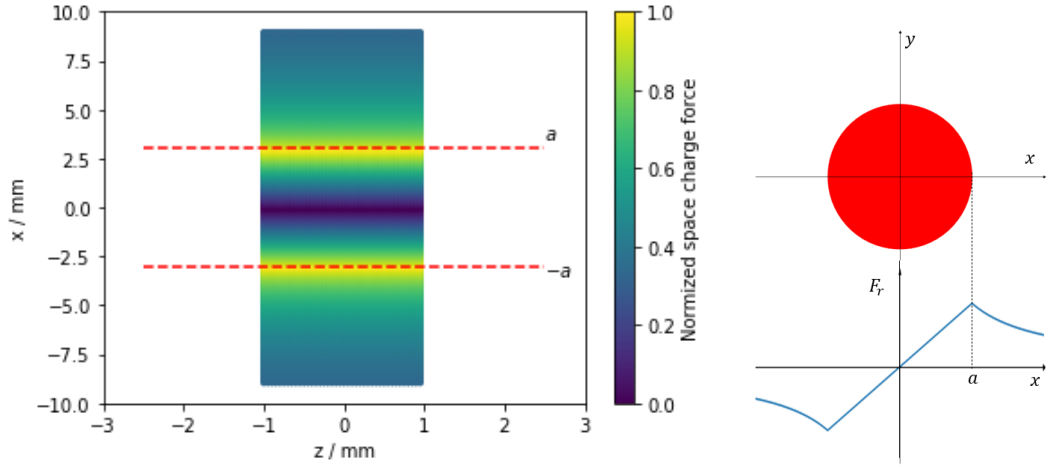

(a) (b)

Fig. 2.3 Beam with transverse uniform distribution (a) z-r 2-D distribution of space-charge force, (b) 1-D distribution of space-charge force vs beam radius.

where σ_{laser} is the laser spot RMS size on the cathode, X_g is the geometry factor related to the cathode roughness, E is the electric field amplitude.

2.3.4 Space charge effect emittance

The charged particles in a beam produce their own electromagnetic field, mentioned as the self-field. In electron injectors where the particle energy is still relatively low and the particle density is moderate, the dominant effect comes from the average Coulomb forces caused by the charge distribution of the beam. This effect is called the space charge effect. In order to estimate the strength of the space charge effect, the radial force on an electron inside a cylindrically-symmetric beam with an uniform or Gaussian [44] charge distribution can be calculated. For the uniform distribution with the longitudinal charge density λ_0, and radius a, the force is

$$\begin{aligned} F_r &= \frac{\lambda_0 e}{2\pi\epsilon_0 a^2} r - \frac{\mu_0 v^2 \lambda_0 e}{2\pi a^2} r \\ &= \frac{\lambda_0 e}{2\pi\epsilon_0 a^2} r(1-\beta^2) = \frac{\lambda_0 e}{2\pi\epsilon_0 a^2 \gamma^2} r \quad (r \leqslant a), \end{aligned} \tag{2.39}$$

$$F_r = \frac{\lambda_0 e}{2\pi\epsilon_0 a^2} r(1-\beta^2) = \frac{\lambda_0 e}{2\pi\epsilon_0 \gamma^2 r} \quad (r > a), \tag{2.40}$$

where β and γ are the Lorentz factors. ϵ_0 and μ_0 are the vacuum permittivity and vacuum permeability. Fig. 2.3 gives a radius space charge force distribution according to Eq. 2.39 and Eq. 2.40. For a Gaussian distribution, such as:

$$\rho(r,z) = \frac{Q}{(\sqrt{2\pi})^3 \sigma_z \sigma_r^2} \mathrm{e}^{-z^2/2\sigma_z^2} \mathrm{e}^{-r^2/2\sigma_r^2}, \tag{2.41}$$

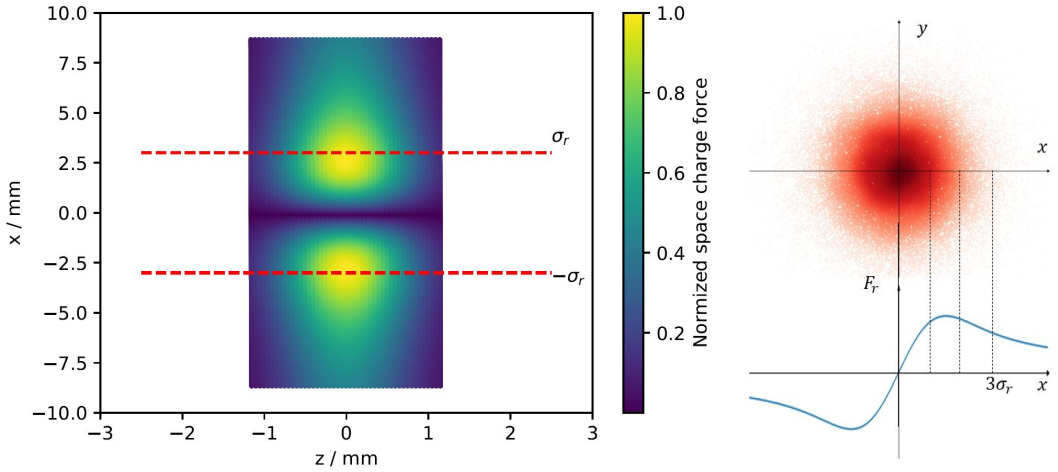

(a) (b)

Fig. 2.4 Beam with transverse Gaussian distribution (a) z-r 2-D distribution of space-charge force, (b) 1-D distribution of space-charge force vs beam radius.

the force is then

$$F_r = \frac{e}{2\pi\epsilon_0\gamma^2}\frac{Q}{\sqrt{2\pi}\sigma_z}\mathrm{e}^{-z^2/2\sigma_z^2}\left[\frac{1-\mathrm{e}^{-r^2/2\sigma_r^2}}{r}\right], \tag{2.42}$$

where Q is the bunch charge, σ_r and σ_z are the beam RMS size in radial and longitudinal directions, and the space charge force distribution is shown as Fig. 2.4. It can be seen that the radial space charge force decreases with γ^2. Thus near the cathode, the space charge effect is more serious than out of the cavity. Some investigations on the space charge emittance increase near the cathode due to non-uniform emission have been done at SLAC [37]. They developed a model to study the emittance growth due to the space charge. In this model, the beam with radius R is separated into small round beamlets with radius r_0 and arranged in a rectangular transverse pattern. The distance between the beamlets center is $4r_0$. The space charge emittance is given as:

$$\Delta\varepsilon_{n,sc} = \sigma_x\frac{4r_0}{\sqrt{\pi}R}\sqrt{\frac{I_p}{I_0}}, \tag{2.43}$$

where the I_p is the bunch peak current, and I_0 is the characteristic current which has a value of about 17 kA.

2.4 Simulation tools

2.4.1 ASTRA

In the thesis, one simulation tool, A Space Charge Tracking Algorithm (ASTRA) [45], is applied to study the beam dynamics. In ASTRA, different initial distributions of the macroparticles can be generated with various standard parameters. The users can input the external fields to build standard elements, such as cavities, solenoids, quadrupoles, and other components. The

grids are overlaid upon the macroparticles distribution. In most cases, the cylindrical symmetry in the space charge calculation is used to save computing time. However, for the beam with unsymmetric distribution, 3-D grids provide accurate results at the cost of more computing time. Maxwell's equations are solved in the grids based on a nonadapitve Runge-Kutta integration of 4^{th} order. Then the Lorentz force is adopted to every macroparticle to calculate the next simulation time step. The users can decide to switch on and off of space charge effect in the simulation. The 6-D parameters of the macroparticles in Cartesian coordinates and the beam properties parameters, such as emittance, energy, energy spread, bunch duration and so on are recorded in files for further processing.

2.4.2 COMSOL Multiphysics

In this thesis, the study of the solenoid field analysis is carried out with COMSOL Multiphysics [46]. It is a kind of finite element analysis software used in all fields of engineering, manufacturing, and scientific research. The module AC/DC, which can simulate low-frequency electromagnetics and electromechanical components, is applied in the solenoid field simulation. In general, six types of models can be selected to build the object profile, including 0-D, 1-D axisymmetric, 1-D and 2-D axisymmetric, 2-D, and 3-D. The symmetric settings can improve the calculation efficiency. The magnetic field part in the AC/DC module can compute magnetic fields and induced current distributions in and around coils, conductors, and magnets. The stationary, frequency-domain, small-signal analysis and time-domain modeling are supported in 2-D and 3-D. The physics interface solves Maxwell's equations using the magnetic vector potential.

Chapter 3

SRF photo injector at ELBE

3.1 Overview

From 2007 to 2014, the first SRF gun was developed and operated as the second CW injector for high bunch charge [47] at ELBE radiation center. The first version of SRF gun, called SRF gun I, was able to inject beams into the ELBE linac in the beginning of 2010 [48]. The basic components of the gun are a 1.3 GHz fine grain niobium cavity consisting of three cells with the TESLA cell shape and one velocity optimized half cell with a choke filter, a normal conducting photocathode, an UV drive laser, an a normal conducting solenoid in the beamline nearby the gun. An updated UV drive laser was installed in 2012. This laser can deliver pulses at four repetition rates, 13 MHz for low bunch charges as well as 500, 250, and 100 kHz for high bunch charges, which fulfills the application of FEL operation at ELBE. In 2013, the first lasing experiment with the far-infrared FEL at ELBE was completed using the beam from SRF gun I successfully [49]. It showed that L-band SRF guns can work in user facilities, but the performance should be improved.

The second version of the SRF gun, called SRF gun II, was installed at ELBE in 2014. This gun has an improved Nb cavity with higher performance and a superconducting solenoid which is situated close to the cavity inside the gun cryomodule. At present, SRF gun II can work stably with an acceleration gradient of 8.0 MV/m which corresponds to 20.5 MV/m peak field on axis. The beam exits the gun with a kinetic energy of 4 MeV. Tab. 3.1 gives the main parameters of SRF gun I and SRF gun II. After further improvements and optimizations, SRF gun II is working with high performance and stability for THz radiation production at ELBE since 2016 [27]. The work presented in the thesis is part of this optimization for SRF gun II.

This chapter will give a general view of SRF gun II from the following five parts: 1. cavity; 2. cryomodule; 3. RF system; 4. cathode and drive laser system; 5. diagnostic beamline and connection to ELBE linac.

Table 3.1 SRF gun I and SRF gun II main parameters.

Parameters	Values	
	gun I	gun II
Type of cavity	ellipical 3.5 cells	
Frequency	1.3 GHz	
Gun operation mode	CW	
Beam kinetic energy at gun exit (MeV)	3.0	4.0
Acceleration gradient E_{ecc} (MV/m)	6	8
Peak field on axis (MV/m)	16.2	20.5
Cathode field (MV/m)	7	14.5
DC bias at cathode (kV)	-5	
Liquid He temtuperature (K)	2	
Dynamic He load at max. E_{acc} (W)	-	10
Derive laser wave length (nm)	262	
Photo cathodes	Cs_2Te	Mg and Cs_2Te
Quantum efficiency (%)	1	0.1-0.3 and 1

3.2 Cavity

As a core part of the SRF gun II, the 3.5 cell cavity was fabricated and tested in Thomas Jefferson National Accelerator Facility (TJNAF). The final RF performance is $Q_0 \approx 8 \cdot 10^9$ for $E_{acc} = 14$ MV/m in 2013 [50]. In May 2014, after installing in HZDR, the values are $Q_0 \approx 5 \cdot 10^9$ for $E_{acc} = 10$ MV/m [32]. At the half cell the field gradient is about 80% of the peak gradient. To suppress the multipacting emission of the secondary electrons, a DC field is usually applied on the cathode. Fig. 3.1 shows an example the on-axis DC and RF field distributions of the cavity.

3.3 Cryomodule

The purpose of the cryomodule is to cool the superconducting Nb cavity down to 2 K and to enable RF operation in CW mode. Fig. 3.2 shows a computer aided design (CAD) cross section view of the cryomodule with labeled main components. The vacuum vessel of the cryomodule is of cylindrical shape with 0.7 m diameter, 1.3 m length and the height with parts on top is 0.9 m. The helium port and the liquid nitrogen (LN) port are on the top of the cryomodule. A LN reservior keep the thermal shielding at 77 K. A warm magnetic shield, made of μ-metal, is used to mitigate the background magnetic field in the cryomodule. The cavity is surrounded by superfluid helium enclosed in a titanium vessel. The helium loading power is up to 40 W (or 2 g/s), in which 7 W are static loss from the finite thermal isolation and up to 33 W are dynamic loss from the RF. The SC solenoid is located at about 0.7 m downstream of the cathode to focus the beam, compensate space charge force and thus reduce the transverse projected emittance.

A challenging task is to make the normal conducting photocathode work in the superconducting environment of the cavity. A sub-cooling system is designed to solve this problem, shown as Fig. 3.3. The photocathode is cooled down with liquid nitrogen to keep it at 77 K during operation.

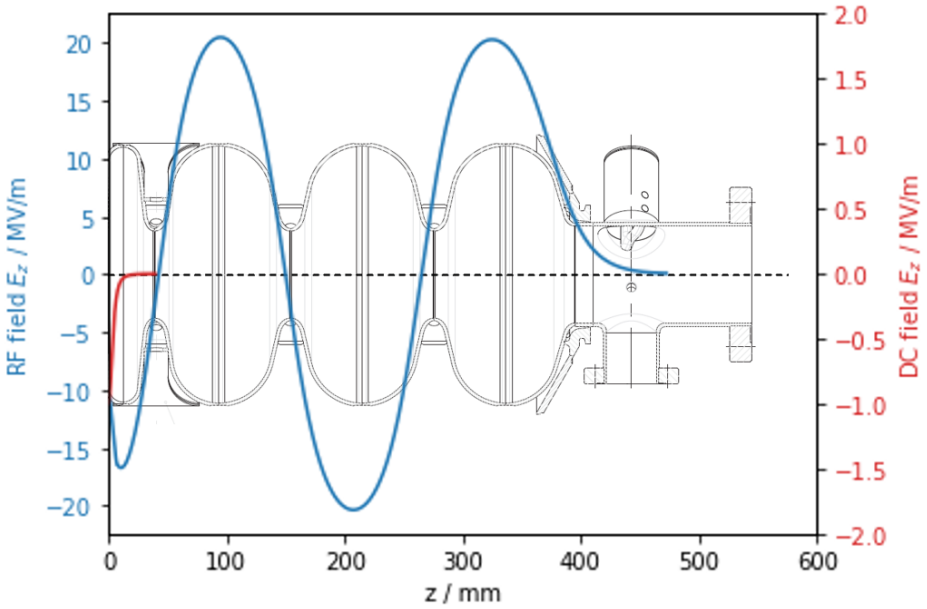

Fig. 3.1 Example output of the combined DC and RF field in the cavity used for the tracking in ASTRA: The average accelerating field was set to 8 MV/m and the DC voltage to -5 kV. The blue curve is the RF field and red curve is the DC field.

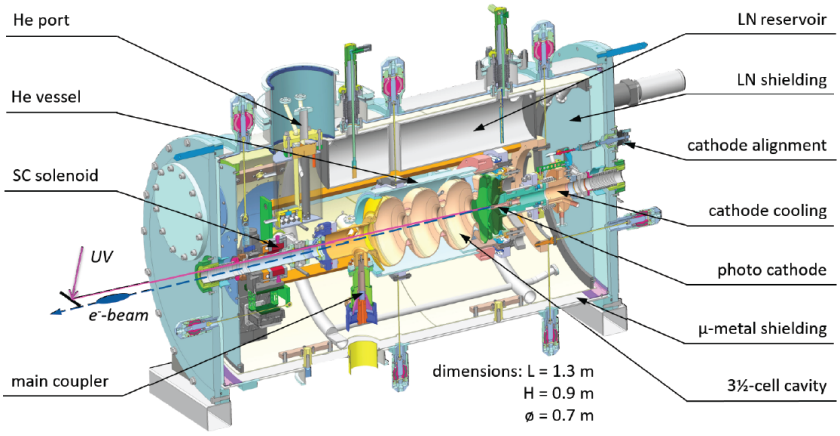

Fig. 3.2 SRF gun II cryomodule.

The cathode is isolated from the cavity and easily exchangeable. Furthermore the cathode can be adjustable with high precision within an positioning range of ± 0.6 mm with respect to the cavity for the best RF focusing. Additionally, a DC bias can be applied to suppress the multipacting which especially occurs at low gradient when the RF is ramped up.

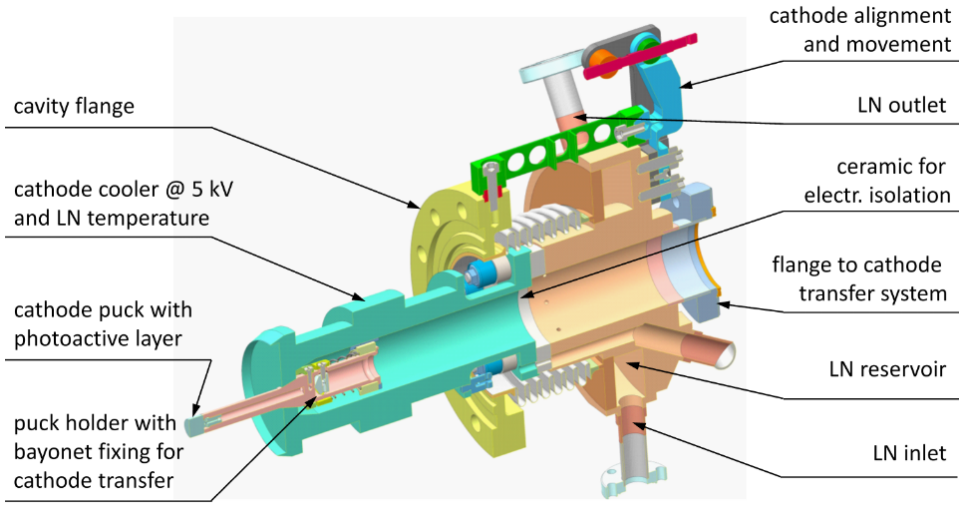

Fig. 3.3 Photocathode holder and cooling system.

3.4 RF system

The RF couplers of the cavity are one coaxial fundamental mode power coupler (FPC) and two TESLA type higher order mode (HOM) dampers. The coupling factor of the FPC is fixed from 6×10^6 to 3×10^7. The coupler has two heat sources. One is from the RF loss between the coaxial and the rectangular waveguide. The other one is the quartz glass window located in the waveguide to keep the vacuum of coupler free of atmosphere. Some copper thermal anchors are used between the HOM and the helium vessel in order to improve the heat conduction. Also, the thermal conductivity between inner conductor of the coaxial line can become higher due to the sapphire RF feedthroughs of the HOM couplers. These methods can decrease the thermal drift during the gradient changes and improve CW capability of the cavity.

As a user facility, to guarantee the stability of timing and beam quality generated from the gun, the RF researchers at ELBE has developed two control system [27, 51]. The first is the analog low level RF controller to keep the amplitude and phase of RF field stable for acceleration. It is an active feedback loop. The amplitude control loop stability can reach RMS 2×10^{-4} and the phase stability RMS 0.01° between 10 Hz to 10 MHz. The second is for the synchronization between the RF system and the derive laser to the ELBE master clock to reduce the locking noise and jitter.

3.5 Cathode and drive laser system

A robust photocathode with high QE is critical for the beam quality and stability of injector operation. The ELBE SRF gun II has applied three kinds of cathode materials: Cu, Mg and Cs_2Te [23]. The metal cathodes are not sensitive to the environment and the vacuum requirement is about 10^{-9} Torr [52]. The work functions of Mg and Cu are 3.6 eV and 4.6 eV, respectively [53]. Even for UV light, metal cathodes have low QE, such as 0.2% to 0.3% for

Mg [54, 55], and in the range of 10^{-5} for Cu [56]. Compared to metal cathodes, semiconductor cathodes have high QE, such as Cs_2Te has up to 10% using UV light [57]. But semiconductors require a higher quality of the vacuum, about 10^{-11} Torr [52]. From 2014 to 2016, the SRF gun II used a Cu cathode. Then Mg cathodes with higher QE were used to deliver higher bunch charges for user operation at ELBE. [27]. Since mid-2019, the Cs_2Te has been used for user beam shifts with high bunch charge [58].

The drive laser system for the SRF gun II was developed by Max Born Institute Berlin (MBI), shown as Fig. 3.4. The infrared laser pulses are generated from the oscillator with repetition rate of 54 MHz. The pulse selector and Pockels cells are used to couple out the laser pulses at repetition rate of 13 MHz with 3 ps pulse FWHM length for bunch charge of 77 pC and of 10, 20, 50, 100, 250 and 500 kHz with 5 ps pulse FWHM length for high bunch charges [27]. The laser power is enlarged by the main multi-pass amplifier. After the amplifier, the infrared laser wavelength is converted from 1048 nm to green with 524 nm by a LBO crystal, and then to 262 nm by a BBO crystal. The output average laser power is up to 0.5 W with Gaussian distribution in transverse and with RMS length of 2.3 ps. The distance between the laser table to the cathode is about 13.5 m. Three sizes of apertures, 0.2 mm, 0.5 mm and 1.5 mm, can be used to shape the laser, called beam shape aperture (BSA). The ratio of laser size on the cathode and the aperture size is 2.5. The laser position on the cathode is remote controlled by a mirror and about 5% of laser intensity is split to a virtual cathode with a CCD camera.

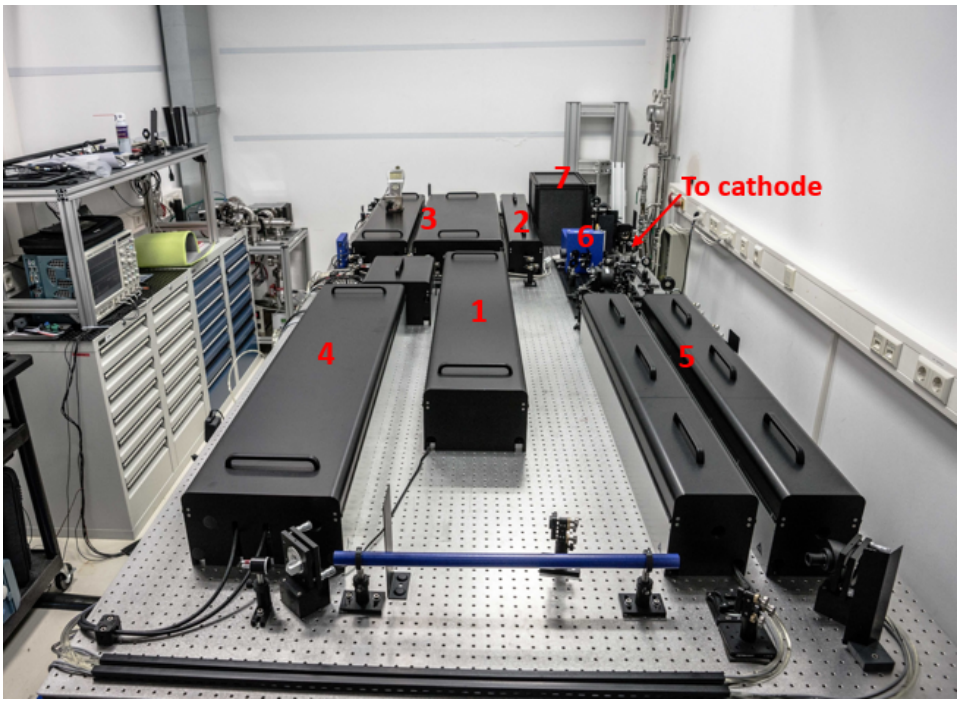

Fig. 3.4 MBI laser system for SRF gun II.

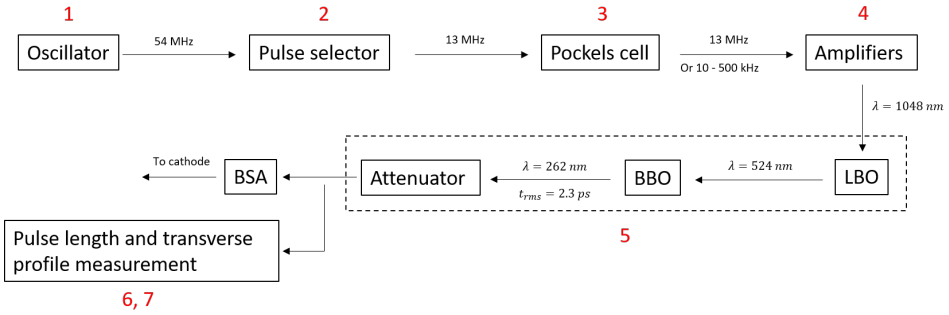

Fig. 3.5 MBI laser flowchart.

3.6 Diagnostic beamline and connection to ELBE linac

For beam characterization a diagnostic beamline is directly connected to the SRF gun as shown in Fig. 3.6. This beamline was designed for SRF gun I in 2008 [59], but is still being used for SRF gun II. A number of upgrades have been performed, especially the no longer needed, heavy normal conducting solenoid could be omitted. As mentioned before, the cathode part, cavity and the SC solenoid are combined in the cryomodule. Nearby the gun, at screen station 1 a retractable Faraday cup allows beam current and dark current measurements. Following the beam direction, three quadrupoles and a 45° bending magnet for beam injection into the ELBE linac are installed. In the straight direction, the slit-scan emittance measurement system is situated which consists of the moving slit in screen station 2 and the screen in screen station 3. A 180° spectrometer magnet used for the beam energy measurement is installed after the screen station 3. Screen station 4 and 5 are in straight and 180° directions following the spectrometer magnet. All screen stations are equipped with a YAG screen, a screen that produces Optical transition radiation (OTR) and a calibration screen.

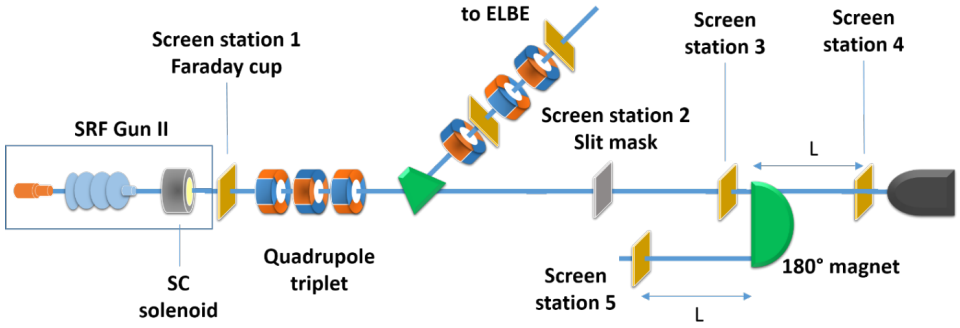

Fig. 3.6 The diagnostic beamline of ELBE SRF gun II.

Chapter 4

SC solenoid

4.1 The influence of solenoid field on transverse emittance

As a significant part of an electron injector, a solenoid provides proper focusing and preserves the beam projected emittance. The normal-conducting injector system has a main focusing solenoid and bucking coil to zero the longitudinal magnetic field at the cathode position. The emittance compensation of a focusing field, such as created by a solenoid, was firstly described by Carlsten in 1989 in simulation [60]. Then Serafini and Rosenzweig expanded this treatment to bunch plasma frequency explaining the projected emittance oscillations for space-charge dominated beams in 1997 [61]. Later Ferrario et al. directly observed the emittance oscillations in experiments and confirmed this theory in 2007 [62]. Rao and Dowell have given a summary of emittance compensation theory in reference [63]. At ELBE SRF gun group, Hannes Vennekate studied the emittance compensation for SRF photo injectors using a SC solenoid installed downstream the cavity in the cryomodule from 2012 to 2017 [64]. Figure 4.1 shows beam transverse phase space changes during the emittance compensation process along the beamline.

There are three issues we should consider about the solenoid when we use it at the beamline: chromatic aberration, spherical aberration and the anomalous multipole field of solenoid [63]. They all can increase the beam projected emittance.

4.1.1 Solenoid chromatic aberration

The solenoid's focal strength depends on the beam energy and the on-axis radial magnetic field component as defined in the following Eq. 4.1 which is valid in thin-lens approximation:

$$\frac{1}{f_{sol}} = \frac{1}{4}\left(\frac{e}{p}\right)^2 B_s^2 L_s. \tag{4.1}$$

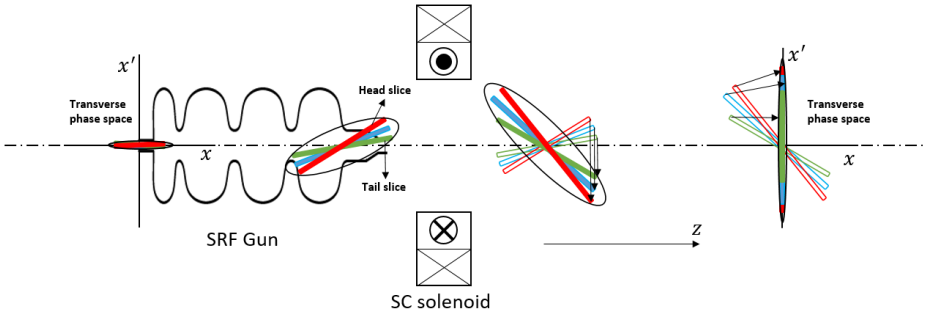

Fig. 4.1 Beam transverse phase space changes during the emittance compensation at the beamline. From the cathode, the emittance is small with little divergence, and the space charge gives different kicks to the slices during accelerating and drifting. The red, green and blue lines represent the head, tail, and middle slices. x and x' are the coordinate system in transverse phase space, and z is the longitudinal direction in which the electron beam drift direction. The ellipse shows the area of the beam phase space.

Here L_s is the effective length of the solenoid with the definition in Eq. 4.2, e is the electron charge, and p is the beam momentum, and B_s is the maximum value of the field on axis:

$$L_\mathrm{s} = \frac{\int B(z)^2 \cdot dz}{B_s^2}. \tag{4.2}$$

As linear transport theory in the former section, the beam RMS matrix is:

$$\sigma \equiv \begin{pmatrix} \langle x^2 \rangle & \langle xx' \rangle \\ \langle xx' \rangle & \langle x'^2 \rangle \end{pmatrix} \equiv \begin{pmatrix} \sigma_{11} & \sigma_{12} \\ \sigma_{12} & \sigma_{22} \end{pmatrix}. \tag{4.3}$$

The transport matrix for a solenoid in thin lens approximation is:

$$\mathrm{M}_{sol} = \begin{pmatrix} 1 & 0 \\ -\frac{1}{f_{sol}} & 1 \end{pmatrix}. \tag{4.4}$$

After the solenoid lens, the beam RMS matrix is:

$$\sigma(s) = \mathrm{M}_{sol}\sigma\mathrm{M}_{sol}^T = \begin{pmatrix} 1 & 0 \\ -\frac{1}{f_{sol}} & 1 \end{pmatrix} \begin{pmatrix} \sigma_{11} & \sigma_{12} \\ \sigma_{12} & \sigma_{22} \end{pmatrix} \begin{pmatrix} 1 & -\frac{1}{f_{sol}} \\ 0 & 1 \end{pmatrix}, \tag{4.5}$$

and becomes:

$$\sigma(s) = \begin{pmatrix} \sigma_{11} & \sigma_{12} - \frac{\sigma_{11}}{f_{sol}} \\ \sigma_{12} - \frac{\sigma_{11}}{f_{sol}} & \sigma_{22} + \frac{\sigma_{11}}{f_{sol}^2} - \frac{2\sigma_{12}}{f_{sol}} \end{pmatrix}. \tag{4.6}$$

Considering a momentum spread δp, the derivative of $\sigma(s)$ with respect to p gives

$$\delta\sigma(s) = \begin{pmatrix} 0 & \frac{\sigma_{11}}{f_{sol}^2}\frac{d}{dp}(f_{sol}) \\ \frac{\sigma_{11}}{f_{sol}^2}\frac{d}{dp}(f_{sol}) & \cdots \end{pmatrix} \delta p. \tag{4.7}$$

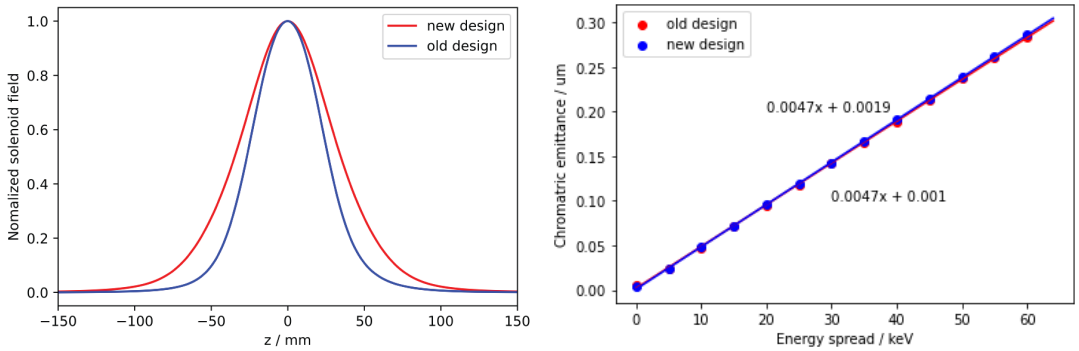

(a) (b)

Fig. 4.2 The solenoid field normalized distribution and the emittance from chromatic aberration with the energy spread in ASTRA simulation. In simulation, the beam RMS size is 1 mm, beam kinetic energy is 3.5 MeV, and the solenoid focal length is 1.56 m.

That delivers the extra geometrical emittance

$$\Delta\varepsilon_{chro} = \sqrt{det(\delta\sigma(s))} = \frac{\sigma_{11}}{f_{sol}^2}\frac{d}{dp}(f_{sol})\delta p; \tag{4.8}$$

With equation 4.1 into Eq. 4.8 one obtains finally:

$$\Delta\varepsilon_{chro} = 2\sigma_{11}(\frac{e}{p})^2 B_s^2 L_s \frac{\delta p}{p} = \frac{8\sigma_{11}}{f_{sol}}\frac{\delta p}{p}. \tag{4.9}$$

From Eq. 4.9, one can find that the emittance due to chromatic aberration is linear with the momentum spread and with the beam RMS size at the entrance of the solenoid. It is independent of the detailed solenoid field distribution, if the solenoid focal strength is the same. The two different solenoid field distributions, shown in Fig. 4.2, where one is from the older design and the other one is the from the new design as examples, show the same contributions due to chromatic aberration to the normalized emittance. The new design has a broader field distribution than the older design. The simulation is based on ASTRA code, and the parameters are given in the figure caption.

4.1.2 Solenoid spherical aberration

Magnetic lenses can show imaging errors although the particles have a negligibly small momentum distribution. The reasons are spherical aberrations which are caused from regions of nonlinear fields in the lens and particle rays with slopes deviate from the paraxial approximation. The spherical aberration has a third order dependence on the radial position of the particle in the solenoid. The spherical aberration can be calculated by extending the paraxial trajectory equation to higher order terms, here for an axisymmetric magnetic field up to third order [4]:

$$r'' + \kappa r + \kappa r'^2 r - \kappa\left(\frac{B'}{B}\right) r' r^2 + \left[\kappa^2 - \frac{1}{2}\kappa\left(B''\right)\right] r^3 = 0. \tag{4.10}$$

In this equation, r is the radial coordinate of the particle; B' and B'' are the first and second derivative of the solenoid longitudinal field respect to z; $\kappa = (\frac{eB_0}{2m_0c\gamma\beta})^2 = \frac{w_L^2}{\beta^2c^2}$, B_0 is the maximum interior magnetic field of the solenoid, e and m_0 give the electron charge and mass, c is the velocity of light, β and γ are the relativistic factors. Fig. 4.3 shows the spherical aberration effect, where r_0 is the beam radius at the entrance of the solenoid and r_i is the beam size at the image plane. If one considers a beam with emittance and energy spread, r_i can be

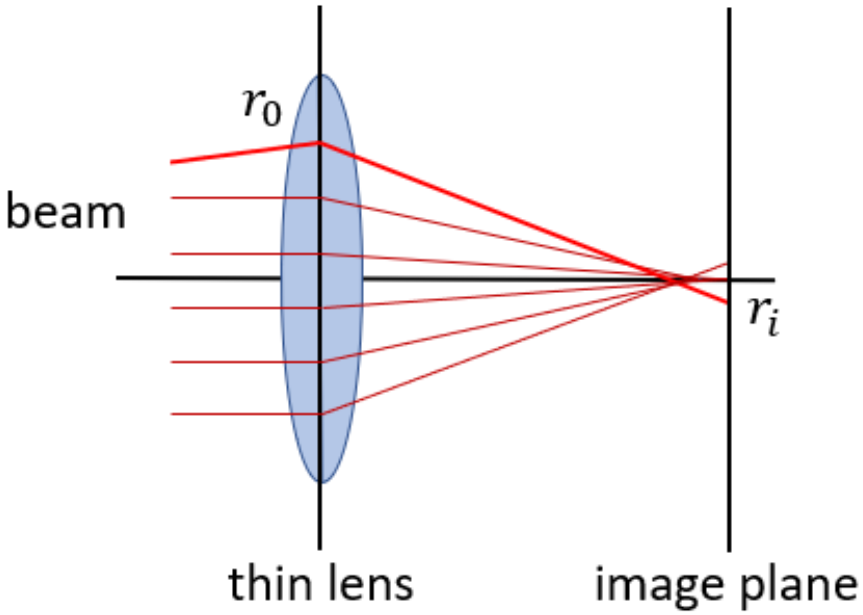

Fig. 4.3 Spherical aberrations effect.

written as [65]:

$$r_i^2 = \left(\frac{\varepsilon}{r_0} f_{sol}\right)^2 + \left(2r_0\frac{\Delta\gamma}{\gamma}\right)^2 + \left(C_S r_0^3\right)^2, \tag{4.11}$$

where ε is the beam emittance, and $\Delta\gamma$ is the beam energy spread. C_s is the spherical aberration coefficient and can be expressed by:

$$C_S = \frac{1}{2}\frac{\int B(z)'^2 dz}{\int B(z)^2 dz}. \tag{4.12}$$

The solenoid spherical aberration emittance can be calculated as:

$$\Delta\varepsilon_{sph} = \frac{r_0^4}{2\sqrt{6}f_{sol}}\sqrt{\frac{C_1^2}{12} + \frac{C_1C_2}{5}r_0^2 + \frac{C_2^2}{8}r_0^4}, \tag{4.13}$$

$$\begin{aligned} C_1 &= C_s \\ C_2 &= \frac{5}{64}\frac{\int B(z)''^2 dz}{\int B(z)^2 dz}. \end{aligned} \tag{4.14}$$

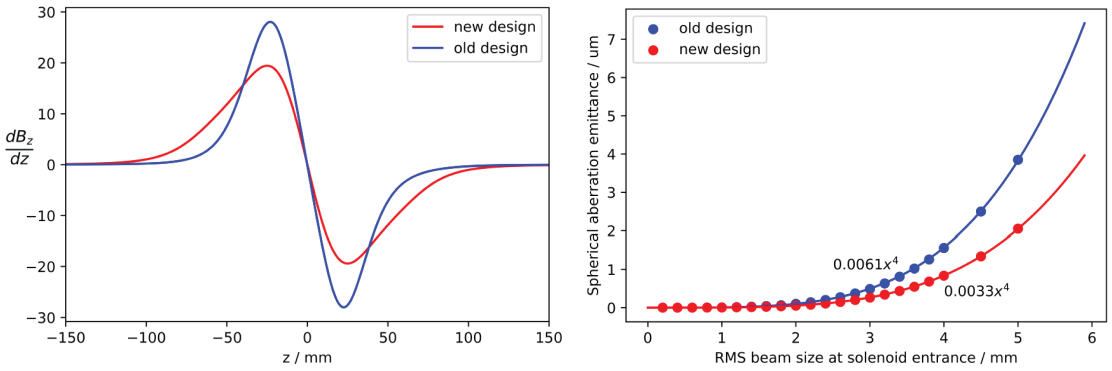

(a) (b)

Fig. 4.4 The comparison of the SC solenoid longitudinal field first derivative (a), and the spherical aberration emittance from ASTRA simulation (b), with new and old designs.

In the right side of Eq. 4.13, compared with the first term, the left terms are much smaller. So the spherical aberration emittance is of fourth power in the beam RMS size at the solenoid entrance.

To decrease the influence of spherical aberration, we optimized the yoke of the SC solenoid at ELBE, and the solenoid longitudinal field is shown as Fig. 4.2 (a). Fig. 4.4 (a) shows the comparison of the second derivative of the old and new design solenoid longitudinal field. One can see that the new design decreases the magnitude of the first derivative at the ends of the solenoid field significantly. In ASTRA simulation, the beam kinetic energy is 3.5 MeV and the space change is ignored. At the entrance of the solenoid, the beam emittance is set to zero with Gaussian distribution. The integral B_z^2 is 1.19×10^{-3} T$^2 \cdot$ m for both old and new design solenoid. Fig. 4.4 (b) shows the spherical aberration emittance of the two designs at the exit of the solenoid. The parameter of the cubic fitting for the new design is about half of the value of the old design. In our facility, the beam RMS size for 200 pC is 3 to 4 mm for Gaussian distribution and maximum gradient 20.5 MV/m with phase 55 degrees. So the spherical aberration emittance of the new design solenoid is 0.85 mm $\cdot$ mrad. The fitting coefficient decreases by 46 %.

4.2 Solenoid field measurement and analysis

4.2.1 Solenoid field analysis in theory

In the current-free region, the magnetic field must satisfy the magnetostatic equations

$$\begin{aligned} \bigtriangledown \cdot \mathbf{B} &= 0, \\ \bigtriangledown \times \mathbf{B} &= \mathbf{0}. \end{aligned} \tag{4.15}$$

Near the axis, the components of an axisymmetric magnetic field (the magnetic field components) can be written as series expansions

$$B_z(r,z) = a_0(z) + ra_1(z) + \frac{1}{2}r^2a_2(z) + \cdots = \sum_{n=0}^{\infty}\frac{r^n}{n!}a_n(z), \tag{4.16}$$

$$B_r(r,z) = b_0(z) + rb_1(z) + \frac{1}{2}r^2b_2(z) + \cdots = \sum_{n=0}^{\infty}\frac{r^n}{n!}b_n(z), \tag{4.17}$$

$$B_\phi(r,z) = 0. \tag{4.18}$$

With the divergence equation and curl equation, one can derive that:

$$B_z(r,z) = \sum_{n=0}^{\infty}\frac{(-1)^k}{4^k}\frac{r^{2k}}{(k!)^2}\left[\frac{\partial^{2k}B_z(0,z)}{\partial z^{2k}}\right], \tag{4.19}$$

$$B_r(r,z) = \sum_{n=0}^{\infty}\frac{(-1)^{k+1}}{4^k}\frac{r^{2k+1}}{(2k+2)(k!)^2}\left[\frac{\partial^{2k+1}B_z(0,z)}{\partial z^{2k+1}}\right]. \tag{4.20}$$

The first terms in the expansions give the terms which are usually used:

$$B_z(r,z) = B_z(0,z) - \frac{r^2}{4}\left[\frac{\partial^2 B_z(0,z)}{\partial z^2}\right] + \cdots \tag{4.21}$$

$$B_r(r,z) = -\frac{r}{2}\left[\frac{\partial B_z(0,z)}{\partial z}\right] + \frac{r^3}{16}\left[\frac{\partial^3 B_z(0,z)}{\partial z^3}\right] + \cdots. \tag{4.22}$$

From $B_z(r,z)$ equation, the n-th term in the series expansion is a kind of form:

$$\sim \frac{r^n}{2^n\left[(\frac{n}{2})!\right]^2}\left[\frac{\partial^n B_z(0,z)}{\partial z^n}\right]. \tag{4.23}$$

Ignoring constant factors, it indicates that the ratio of the adjacent terms in the series is rough:

$$\frac{a_{n+2}}{a_n} \sim r^2\frac{\left[\frac{\partial^{n+2}B_z(0,z)}{\partial z^{n+2}}\right]}{\left[\frac{\partial^n B_z(0,z)}{\partial z^n}\right]}. \tag{4.24}$$

In general, this ratio needs to be less than one for the series to converge. Hence, this provides a criterion for being 'near' the axis:

$$r \ll \sqrt{\frac{\left[\frac{\partial^{n+2}B_Z(0,z)}{\partial z^{n+2}}\right]}{\left[\frac{\partial^n B_Z(0,z)}{\partial z^n}\right]}}. \tag{4.25}$$

The field region in the next section satisfies this condition.

One method to find the solenoid magnetic field axis is to analyze the field near the axis based on Eq. 4.21 and Eq. 4.22. Fig. 4.5 shows the scheme of a misaligned solenoid where the pole angle is θ and azimuthal angle is ϕ. The solenoid field axis vector is $\mathbf{k} = (x, y, z)$. The transfer

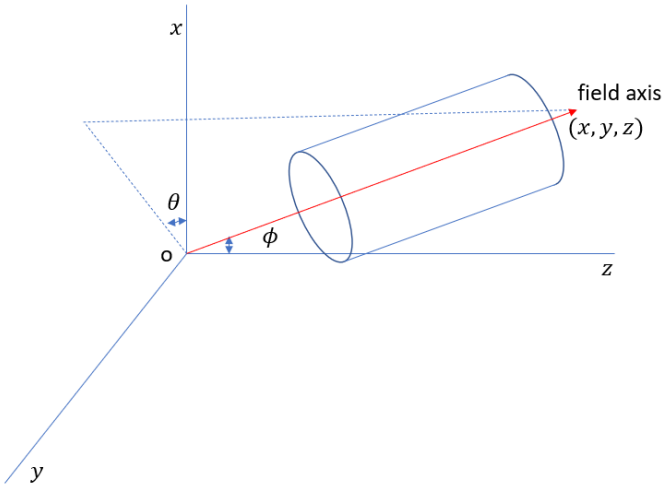

Fig. 4.5 Solenoid misalignment in coordinate system.

expressions are:

$$\begin{aligned} r &= \sqrt{x^2 + y^2 + z^2} \\ x &= r \sin\phi \cos\theta \\ y &= r \sin\phi \sin\theta \\ z &= r \cos\phi. \end{aligned} \tag{4.26}$$

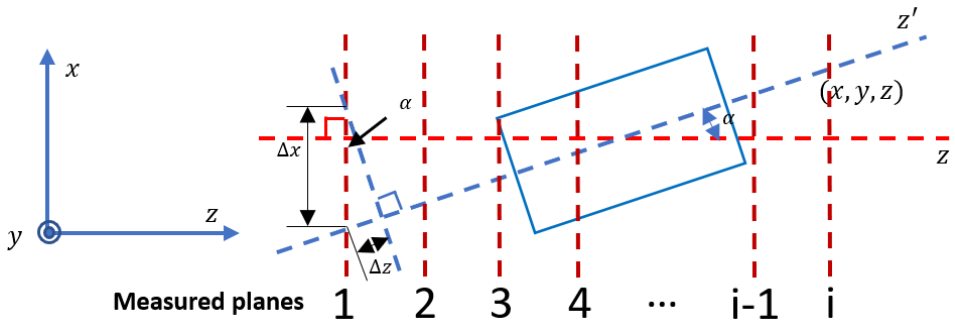

Fig. 4.6 Solenoid misalignment in coordinate system on xz-plane.

The origin point is not always the same in the measurement coordinate system. We set the yz-plane as the horizontal plane, and the xy and xz are vertical planes. The xy-plane, xz-plane, and yz- plane are perpendicular to each other. Fig. 4.6 shows an example of the misaligned solenoid with the projection in the xz-plane. The field data are collected in the measurement planes with index 1 to i, which have a fixed angle to the normal direction of the field axis. In the measured plane, the points with different x values have different longitudinal field derivatives, which means that Eq. 4.21 and Eq. 4.22 cannot be used directly. However, if the plane is located at the position where the longitudinal field has a small gradient, we can use the linear regression method to fit the longitudinal field, such as in Eq. 4.28, and replace the $B_z(0, z)$ in

Eq. 4.21 and 4.22.

$$\Delta z = \Delta x \sin(\alpha) \tag{4.27}$$

$$B_z^{'}(0,z) = B_z(0,z) + k_1 \Delta z + k_2 (\Delta z)^2 + k_3 (\Delta z)^3 + \cdots \tag{4.28}$$

For the multipole field analysis, Walckiers described a method with coils and wires used in CERN LHC magnetic measurement [66, 67]. They have developed fully automated instruments and data analysis processes for the harmonic coil method to measure the multipole modes in magnetic fields. The idea is based on Faraday's law of induction. As the definition of magnetic flux:

$$\Phi_{\mathrm{B}} = \iint_{\mathrm{A}} \mathbf{B} \cdot \mathrm{d}\mathbf{A}, \tag{4.29}$$

Faraday's law of induction says that if the magnetic flux of the wire loop changes, an electromotive force will be produced:

$$\mathcal{E} = -\frac{\mathrm{d}\Phi_B}{\mathrm{d}t}. \tag{4.30}$$

A voltage integrator connected to the coil will be used to eliminate the time coordinate, and the result is only related to the position of the coil. The complex 2D magnetic field is a kind of form:

$$B(x + i \cdot y) = B_y(z) + i \cdot B_x(z) = \sum_{n=1}^{\infty} C_n \cdot \left(\frac{z}{R_{\mathrm{r}}}\right)^{n-1}. \tag{4.31}$$

Here $C_n = B_n + iA_n$, which B_n and A_n represent the normal and skew multipoles of the field. For the rectangle coils with N_t turns and length L, the magnetic flux is:

$$\Psi(z) = N_{\mathrm{t}} \cdot L \cdot \int_{R_1}^{R_2} B(z) \cdot dz, \tag{4.32}$$

R_1 and R_2 are the radii of the rectangle edges with respect to the rotating axis,

$$z = x + i \cdot y = R \cdot e^{i\theta(t)}. \tag{4.33}$$

Then

$$\Psi(\theta = \omega \cdot t) = \mathrm{Re}\left(\sum_{n=1}^{\infty} N_{\mathrm{t}} \cdot L \cdot \frac{R_2^n - R_1^n}{n \cdot R_{\mathrm{r}}^{n-1}} \cdot C_n \cdot e^{in\theta}\right). \tag{4.34}$$

To simplify the expression, let

$$K_n = N_{\mathrm{t}} \cdot L \cdot \frac{R_2^n - R_1^n}{n \cdot R_{\mathrm{r}}^{n-1}}. \tag{4.35}$$

Then

$$\Psi_n = K_n \cdot C_n = K_n \cdot (B_n + iA_n). \tag{4.36}$$

The Fourier analysis coefficients of Φ_n are the multipoles of the field, such as $n = 1$ gives the dipole modes, and $n = 2$ gives the quadrupole modes, shown in Fig. 4.7.

Although this method has high accuracy for the measurements of 2D magnetic fields, it needs a complex control and an electric analysis system and is not convenient for an accelerator facility without a unique field measurement laboratory. To measure the multipole modes easier without the professional equipment, we use the formalism fitting from the Hall probe [68] data. As the

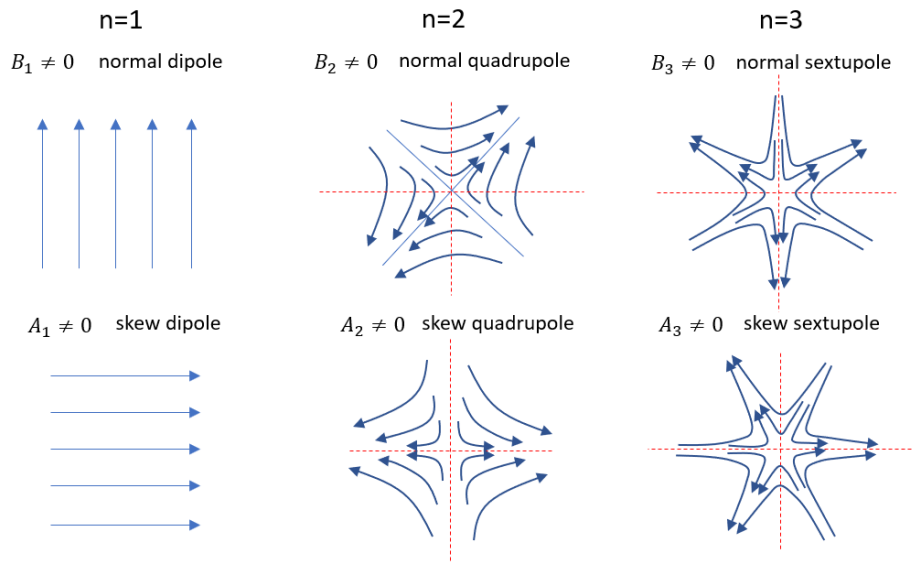

Fig. 4.7 Field lines of normal and skew dipole, quadrupole and sextupole modes field.

definition of dipole, quadrupole and sextupole from [36]:

$$\begin{aligned}
\mathbf{B}_{dn} &= 0\mathbf{e_x} + J_{dn}\mathbf{e_y} \\
\mathbf{B}_{ds} &= -J_{ds}\mathbf{e_x} + 0\mathbf{e_y} \\
\mathbf{B}_{qn} &= J_{qn}y\mathbf{e_x} + J_{qn}x\mathbf{e_y} \\
\mathbf{B}_{qs} &= -J_{qs}x\mathbf{e_x} + J_{qs}y\mathbf{e_y} \\
\mathbf{B}_{sn} &= J_{sn}xy\mathbf{e_x} + \frac{1}{2}J_{sn}(x^2 - y^2)\mathbf{e_y} \\
\mathbf{B}_{ss} &= -\frac{1}{2}J_{ss}(x^2 - y^2)\mathbf{e_x} + J_{ss}xy\mathbf{e_y},
\end{aligned} \tag{4.37}$$

Here the field coefficients are denoted by the letter J. The subscripts 'd', 'q' and 's' indicate the dipole, quadrupole and sextupole modes, and 'n' or 's' mean the normal or the skew type, respectively. For solenoids, the transverse field is:

$$\mathbf{B}_t = J_t x\mathbf{e_x} + J_t y\mathbf{e_y}. \tag{4.38}$$

So we can rewrite the horizontal and vertical fields as form:

$$\begin{aligned}
B_x &= -J_{ds} + J_{qn}y + (J_t - J_{qs})x + J_{sn}xy - \frac{1}{2}J_{ss}(x^2 - y^2) + \dots \\
B_y &= J_{dn} + J_{qn}x + (J_t + J_{qs})y + \frac{1}{2}J_{sn}(x^2 - y^2) + J_{ss}xy + \dots .
\end{aligned} \tag{4.39}$$

Both transverse magnetic field modes can be measured using a Hall magnetic sensor, and the multipole mode coefficients can be calculated by fitting Eq. 4.39.

4.2.2 Simulation of field mapping and analysis

To verify the feasibility of searching for the solenoid magnetic field axis and multipole fields by this fitting method, simulations are made with COMSOL Multiphysics software. The solenoid model consists of a coil with iron yoke, and the quadrupole fields are created by a pair of a normal and a skew quadrupole consisting of 8 coils in an arangement as shown in Fig. 4.8. The coordinate is a Cartesian coordinate system with the center of the solenoid coil as origin point. The axis of the solenoid is given by the vector $\mathbf{e}_{z'} = (x_0, y_0, z_0)$, and the pole angle is θ and azimuthal angle is ϕ. If there is no misalignment, $\mathbf{e}_{z'} = (0, 0, 1)$ and $\theta = \phi = 0$. The magnetic field data exporting from the simulation is based on the measurement coordinate system $o = (x, y, z)$.

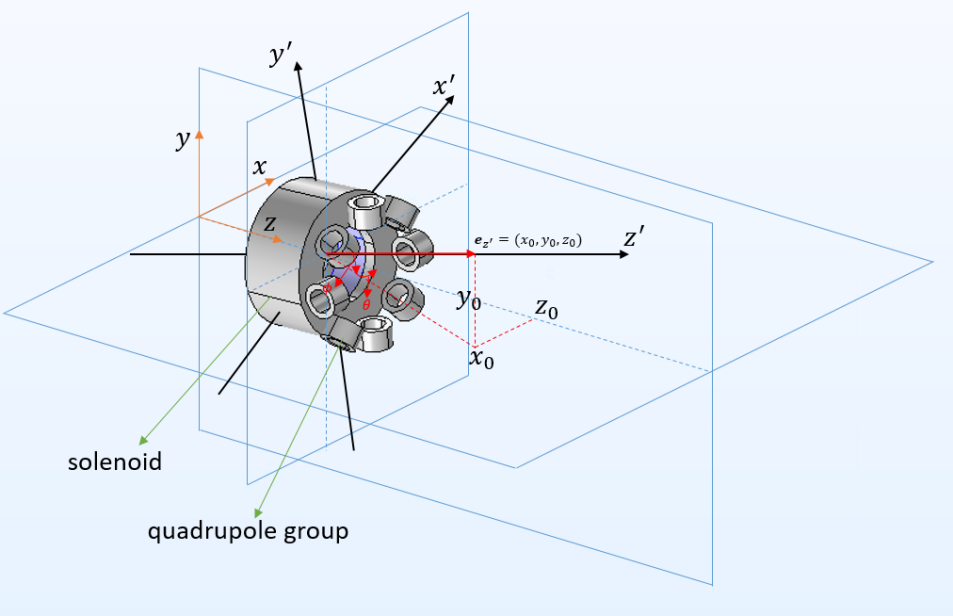

Fig. 4.8 Magnet model and coordinate systems for simulation in COMSOL Multiphysics.

The first part of the simulation deals with the magnetic field mapping and data analysis in order to simulate the determination of the offset and axis tilt angles of the misaligned solenoid. In the simulation the solenoid current was 5 A corresponding to a peak field of 175 mT. The quadrupole coil group was switched off. In the measurement coordinate system the magnetic field components B_z and B_r are taken in 63 planes with 12×13 points in each plane in the range of [-5.5, 5.5] mm $\times$ [-6, 6] mm. The distance between planes is 5 mm and the points in the plane are on a grid with 1 mm distance. By fitting the field components B_z and B_r at the 156 points in each plane, the field can be calculated. Then the center coordinates in these planes deliver the solenoid magnetic field axis by a linear fitting. To guarantee the accuracy and stability of fitting, the linear fitting is separated to two steps. The first step is to fit the points in a range of one to two times of the effective length far from the solenoid center on both sides. The second step is to take the average of these two lines obtained in the first step. Fig. 4.9 shows two groups as examples of axis fitting. To understand the distribution of the field centers along the z direction and make the model simple, it is assumed that the cylindrical coordinate of the solenoid only has a rotation angle α with the axis perpendicular to radius

Table 4.1 Simulation solenoid field axis settings and fit from B_z.

set axis / (10^{-3}, 10^{-3}, 1)	set offset / (mm, mm)	Bz fitting axis / (10^{-3}, 10^{-3}, 1)	Bz fitting offset / (mm, mm)
(3,-7,1)	(2.878, -0.51)	(4.034, -8.377, 1)	(2.915, -0.522)
(3, -20, 1)	(2.878, -0.51)	(4.154, -24.014, 1)	(2.911, -0.528)
(5, -10, 1)	(2.878, -0.51)	(6.866, -11.891, 1)	(2.913, 0.529)
(7, -9, 1)	(4, -4)	(11.018, -10.569, 1)	(4.045, -4.062)
(-8.5, 9, 1)	(-3, 0.5)	(-11.857, 10.651, 1)	(-3.034, 0.512)
(4, -9, 1)	(2, -2)	(5.759, -10.643, 1)	(2.029, -2.033)
(7, -10, 1)	(3.5, -3)	(10.464, -11.492, 1)	(3.538, -3.028)

and longitudinal plane, similar to Fig. 4.6. Ignoring the angular component of the field, then

$$\begin{aligned} B_z(r,z) &= B'_z(r',z')\cos\alpha - B'_r(r',z')\sin\alpha \\ B_{\mathrm{r}}(r,z) &= B'_z(r',z')\sin\alpha + B'_{\mathrm{r}}(r',z')\cos\alpha. \end{aligned} \tag{4.40}$$

The longitudinal component B_z on the axis is the extremum along the radial direction and the radial component B_r is zero, so that

$$\begin{aligned} \frac{\partial B_Z(r,z)}{\partial r} &= 0 \\ B_r(r,z) &= 0. \end{aligned} \tag{4.41}$$

Ignoring the high order terms and use Eq. 4.21 and 4.22, one can obtain that for longitudinal component B_z:

$$r \approx -\frac{\frac{\partial B'_z}{\partial z'}}{\frac{\partial^2 B'_z}{\partial z'^2}} \frac{\tan(\alpha)}{\cos(\alpha)}; \tag{4.42}$$

for radial component B_r:

$$r \approx \frac{B'_z(0,z')}{2\frac{\partial B'_z}{\partial z'}} \sin(\alpha). \tag{4.43}$$

Considering the two zero points in the second derivative of B_z on the mirror planes and one zero point in the first differential of B_z on the center of the solenoid, it is logical that the fitting center distribution from B_z has two peaks at the mirror planes and the fitting center distribution from B_r has one peak at the center plane position. In principle, these two methods are equivalent, but the results from the fitting of B_z are more stable than these from B_r in the simulation, as can be seen in some examples in Tab. 4.1 and 4.2. The relative error of fitting axis tilt from B_z is about 40% to 50% in x direction and 15% to 20% in y direction. The relative error of offset is under 2%. This kind of fitting is a method to estimate the field axis rather than a high accuracy measurement. For the calculation of the tilt angles one can use:

$$\begin{aligned} \theta &= \arctan(\frac{y}{x}) \\ \phi &= \arctan(\frac{\sqrt{x^2+y^2}}{z}) \end{aligned} \tag{4.44}$$

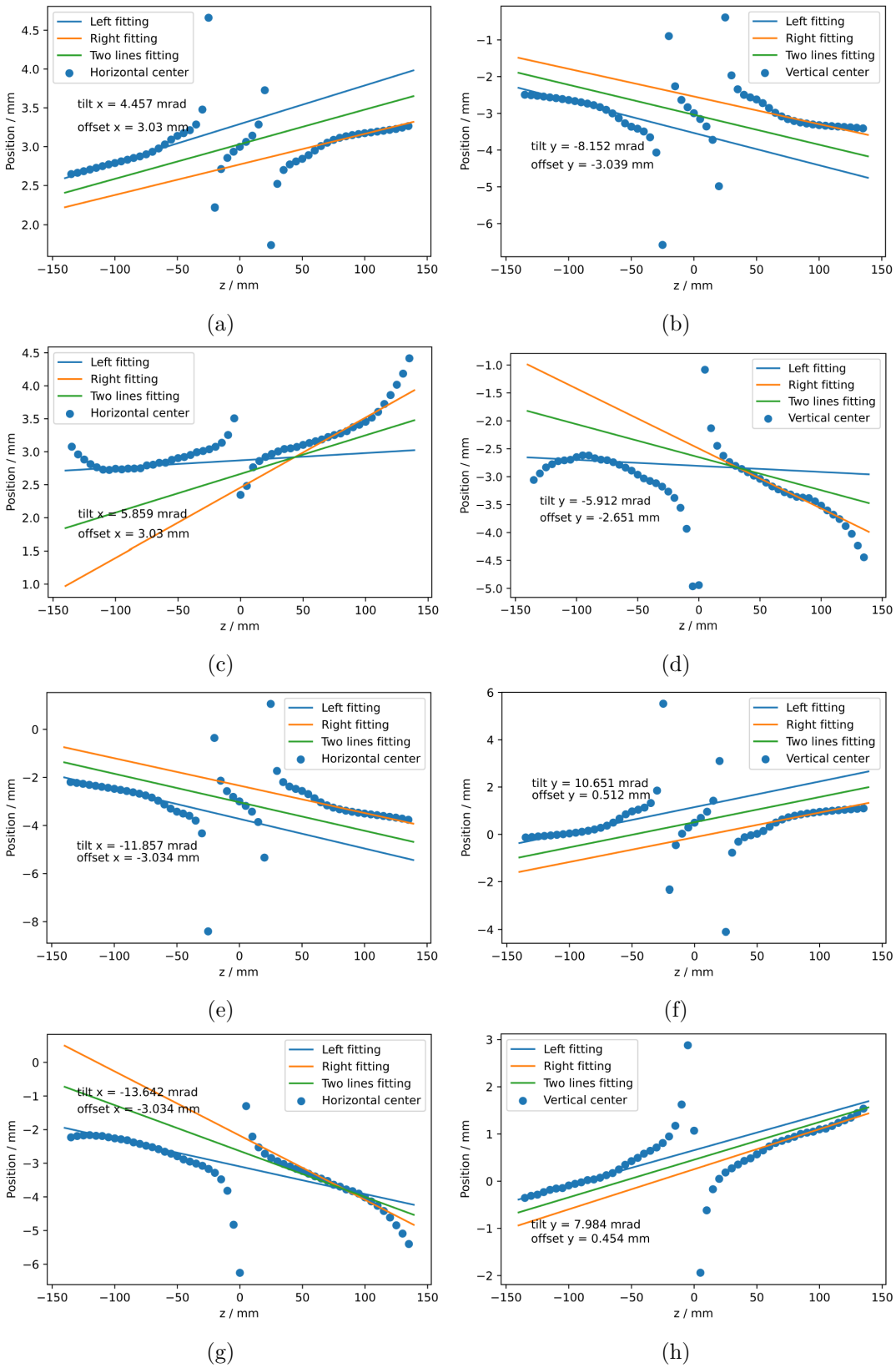

Fig. 4.9 Solenoid field axis fitting. The axis of (a) - (d) is (0.003, -0.007, 1) and with offset of -3 mm in x direction and 0.5 mm in y direction. (a) and (b) are from Eq. 4.21 fitting. (c) and (d) are from Eq. 4.22 fitting; The axis of (e) - (h) is (-0.0085, -0.009, 1) and with offset of -3 mm in x direction and 0.5 mm in y direction. (e) and (f) are from Eq. 4.21 fitting. (g) and (h) are from Eq. 4.22. The texts in every figure are the parameters from the green line fitting.

Table 4.2 Simulation solenoid field axis settings and fit from B_r.

set axis / (10^{-3}, 10^{-3}, 1)	set offset / (mm, mm)	Br fitting axis / (10^{-3}, 10^{-3}, 1)	Br fitting offset / (mm, mm)
(3,-7,1)	(2.878, -0.51)	(4.31, -6.581, 1)	(2.915, -0.459)
(3, -20, 1)	(2.878, -0.51)	(4.669, -18.998, 1)	(2.911, -0.474)
(5, -10, 1)	(2.878, -0.51)	(7.749, -9.275, 1)	(2.913, -0.482)
(7, -9, 1)	(4, -4)	(15.699, -7.489, 1)	(4.045, -3.559)
(-8.5, 9, 1)	(-3, 0.5)	(-13.642, 7.984, 1)	(-3.034, 0.454)
(4, -9, 1)	(2, -2)	(6.72, -8.202, 1)	(2.029, -1.796)
(7, -10, 1)	(3.5, -3)	(13.8, -7.989, 1)	(3.538, -2.634)

In the next simulation, the solenoid is switched off and the field axis vector is $\mathbf{e}_z = (0, 0, 1)$ for the group of quadrupoles. The formalism fitting is helpful to reconstruct the quadrupole field modes from Eq. 4.39. Five different current settings of the quadrupoles are used in COMSOL Multiphysics simulation to show the accuracy of this method. In the simulation, the quadrupole currents are arbitrary values and cannot be compared with the currents of the quadrupole corrector coils in the real photo injector. The results of this simulation are presented in Fig. 4.10. Comparing the coefficients from settings and fitting from Eq. 4.39, one can find that they agree with each other very well. It means that the formalism effectively determines the multipole field modes, although it is difficult to prove the results regarding to the numerical accuracy.

If the solenoid is misaligned, multipole field modes will be introduced, including the dipole, quadrupole, sextupole, and higher modes. In this thesis, we only calculate up to the sextupole. We combine the solenoid center analysis and fitting formalism to analyze its multipole modes for different tilt cases. The solenoid field center is located at origin point when the solenoid has no tilt and offset. The analysis is based on the parameters in Tab. 4.1.

The solenoid transverse field coefficient image agrees with that from calculation based on Eq. 4.22. The mesh size cannot be infinite in the simulation that will give some calculated noise. The axis missing alignment can introduce the dipole , quadrupole and sextupole fields. The dipole field is much larger than the quadrupole and sextupole fields near the solenoid axis center scale. All the multipole modes extend linearly with the axis tilt value increasing. The dipole mode is asymmetric with the solenoid axis center, but not for the quadrupole and sextupole modes. All the peaks of multipole modes appear at two mirror planes or the center plane position. Overall the dipole field is more sensitive than the others to the axis tilt, and the quadrupole field coefficient is much larger than the sextupole coefficient at the same conditions.

4.3 SC solenoid multipole field influence

Considering that the dipole field components only kick the beam, it focus on the influence of the quadrupole field and the sextupole field on the beam emittance in this section. The details about it and how to correct is given in reference [63, 69].

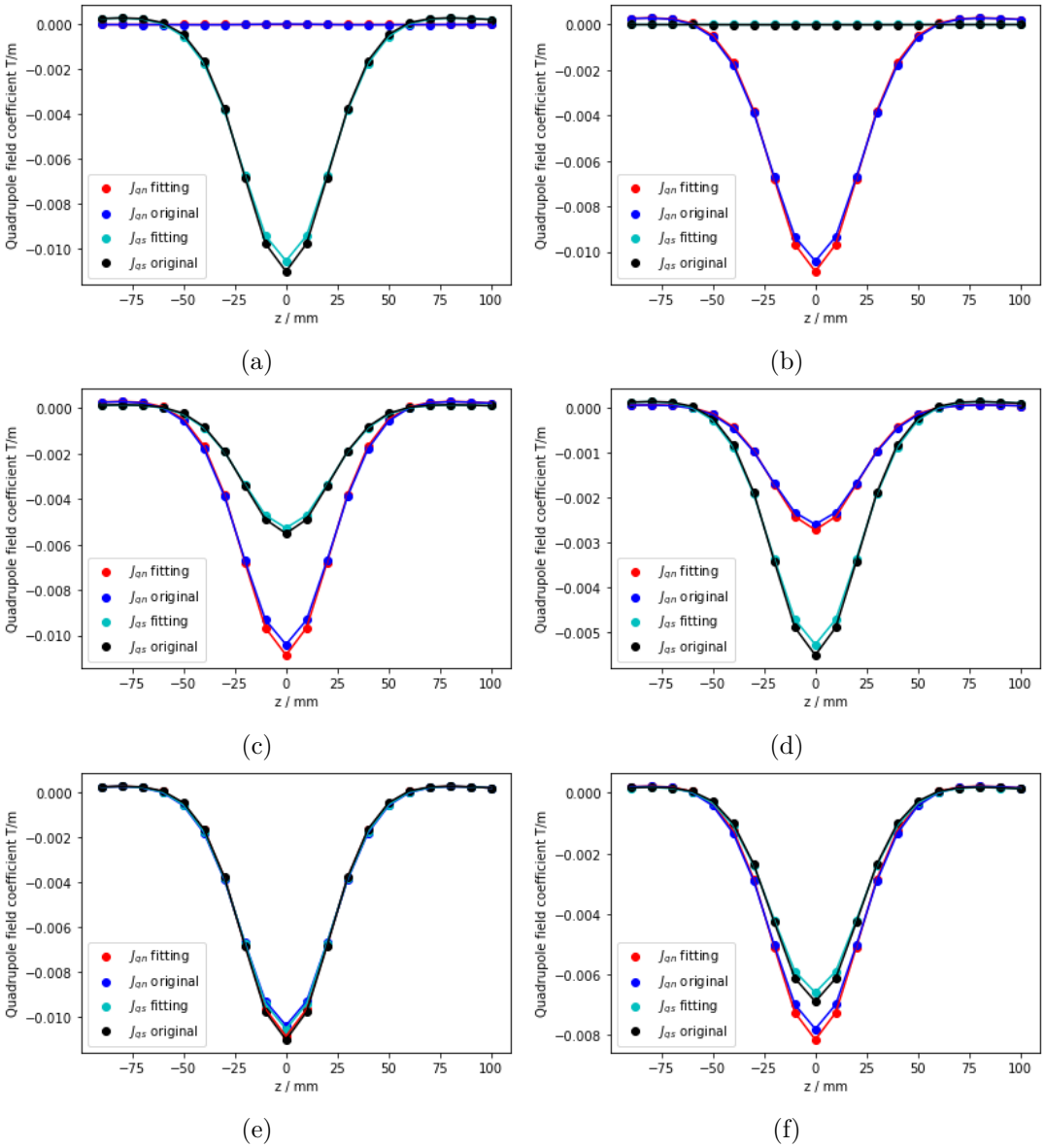

Fig. 4.10 Quadrupol field coefficients data from simulation. (a) is normal quadrupole current is 0 A, skew quadrupole is 80 A; (b) is normal quadrupole current is 80 A, skew quadrupole is 0 A; (c) is normal quadrupole current is 80 A, skew quadrupole is 40 A; (d) is normal quadrupole current is 20 A, skew quadrupole is 40 A; (e) is normal quadrupole current is 80 A, skew quadrupole is 80 A; (f) is normal quadrupole current is 60 A, skew quadrupole is 50 A.

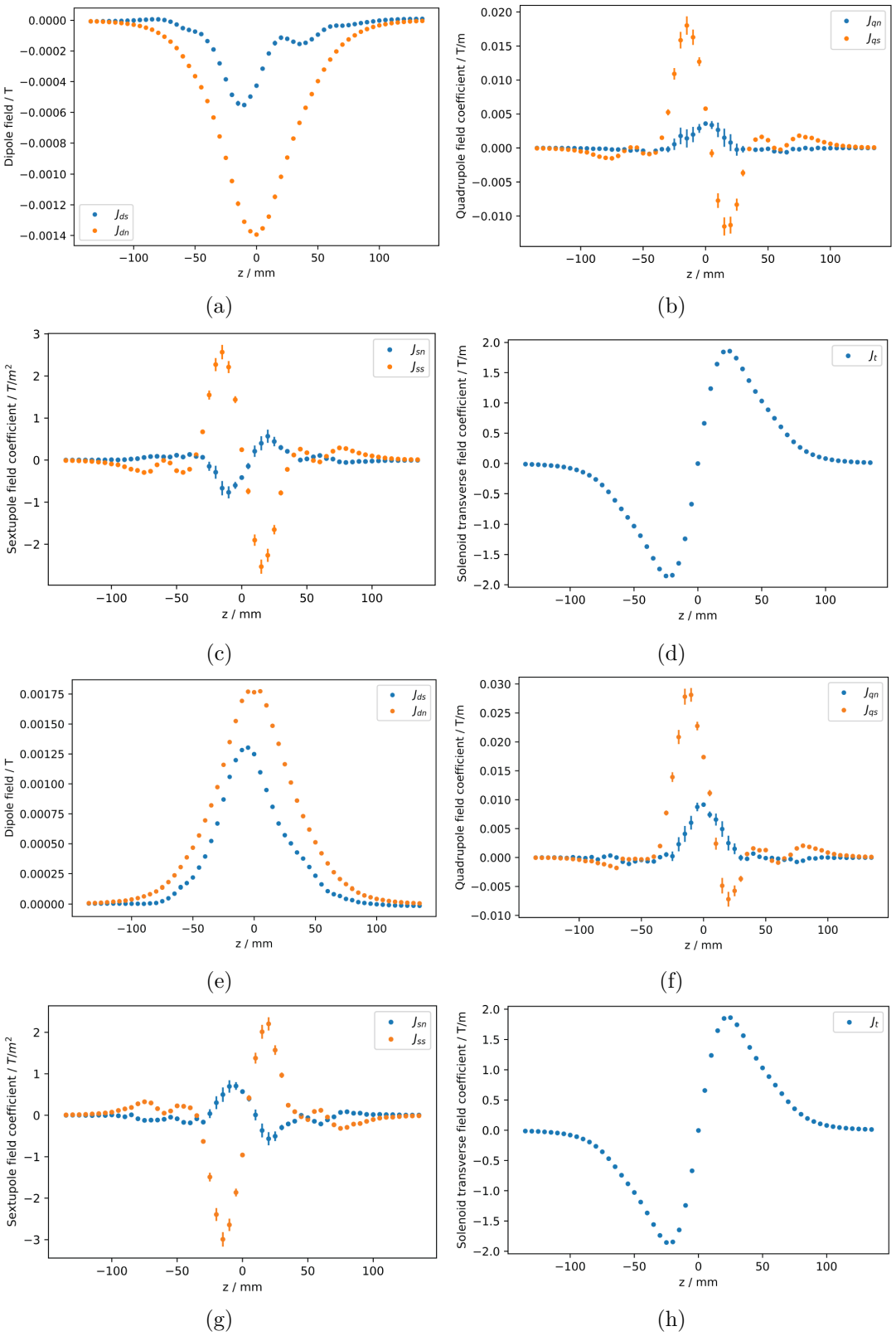

Fig. 4.11 Multipole fields or coefficients of solenoid field obtained for different axis tilt. (a)-(d) are from solenoid axis with (0.003, -0.007, 1) and offset is (2.878 mm, -0.51 mm); (e)-(h) are from solenoid axis with (-0.0085, 0.009, 1) and offset is (-3 mm, 0.5 mm).

The transport matrix in four dimensions, (x, x', y, y'), of a thin normal quadrupole lens and a solenoid lens can be written as:

$$\mathrm{M_{sol}\,M_{quad}} = \begin{pmatrix} \cos^2 KL_s & \frac{\sin KL_s \cos KL_s}{K} & \sin KL_s \cos KL_s & \frac{\sin^2 KL_s}{K} \\ -K \sin KL_s \cos KL_s & \cos^2 KL_s & -K \sin^2 KL_s & \sin KL_s \cos KL_s \\ -\sin KL_s \cos KL_s & -\frac{\sin^2 KL_s}{K} & \cos^2 KL_s & \frac{\sin KL_s \cos KL_s}{K} \\ K \sin^2 KL_s & -\sin KL_s \cos KL_s & -K \sin KL_s \cos KL_s & \cos^2 KL_s \end{pmatrix} \begin{pmatrix} 1 & 0 & 0 & 0 \\ -\frac{1}{f} & 1 & 0 & 0 \\ 0 & 0 & 1 & 0 \\ 0 & 0 & +\frac{1}{f} & 1 \end{pmatrix}. \tag{4.45}$$

In the matrix, L_s is the effective length of the solenoid defined in Eq. 4.2, and $K = \frac{eB_0}{2mc\gamma\beta}$. The normal quadrupole locates at the entrance of the solenoid with focal length f. After the normal quadrupole and the solenoid, the beam matrix is

$$\sigma(s) = \mathrm{M_{sol}M_{quad}}\sigma(0)\left(\mathrm{M_{sol}M_{quad}}\right)^T. \tag{4.46}$$

Then the additional transverse emittance from the quadrupole and the solenoid becomes:

$$\Delta\varepsilon_{n,\ \mathrm{quad\ +\ sol}} = \beta\gamma\frac{\sigma_{x,\ \mathrm{sol}}\ \sigma_{y,\ \mathrm{sol}}}{f}|\sin 2KL_s|. \tag{4.47}$$

When the quadrupole field is rotated by the angle α_1 with respect to a normal quadrupole, the matrix is

$$\mathrm{M_{rotquad}}\ (\alpha_1, f) = \begin{pmatrix} 1 & 0 & 0 & 0 \\ \frac{-\cos 2\alpha_1}{f} & 1 & \frac{-\sin 2\alpha_1}{f} & 0 \\ 0 & 0 & 1 & 0 \\ \frac{-\sin 2\alpha_1}{f} & 0 & \frac{\cos 2\alpha_1}{f} & 1 \end{pmatrix}, \tag{4.48}$$

and Eq. 4.47 changes to:

$$\Delta\varepsilon_{n,\ \mathrm{quad\ +\ sol}} = \beta\gamma\frac{\sigma_{x,\ \mathrm{sol}}\ \sigma_{y,\ \mathrm{sol}}}{f}|\sin 2(KL_s + \alpha_1)|. \tag{4.49}$$

To cancel this influence on the emittance, a pair of correction quadrupoles combining a normal quadrupole and a skew quadrupole is installed in the downstream of the solenoid at distance L, which can rotate the beam by an angle α_2

$$\Delta\varepsilon_{n,\mathrm{total}} = \beta\gamma\left|\frac{\sigma_{x,\mathrm{sol}}\sigma_{y,\mathrm{sol}}}{f}\sin 2\left(KL_s + \alpha_1\right) + \frac{\sigma_{x,\mathrm{cor}}\sigma_{y,\mathrm{cor}}}{f_{\mathrm{cor}}}\sin(2\alpha_2)\right|. \tag{4.50}$$

From Eq. 4.50, one can find that the effect of the corrector is related to the beam RMS size at the corrector position. Here we carried out some simulations using ASTRA and compared the results with Eq. 4.49 and Eq. 4.50. From Fig. 4.13, it can be seen that once the the distance between the corrector, and the solenoid and the quadrupole component of the solenoid are fixed, if the corrector focal strength is not strong enough, it cannot compensate the influence of the quadrupole field from the solenoid. Furthermore we have to consider the distance between the solenoid and the corrector in practice. For the SRF gun, the corrector is located outside the cryomodule at a distance of 0.437 m downstream of the solenoid. Fig. 4.14 shows the simulation results for different distances. At the same parasitic quadrupole focal strength in the solenoid and the same focal strength of the corrector, the shorter the distance, the better is the compensation to emittance. If the distance is too far, such as the blue line in Fig. 4.14, the distance with 0.7 m, the corrector will fail to cancel the influence of quadrupole field of the solenoid or should apply stronger focal strength. From Eq. 4.50, it is obvious to know that the beam size at the corrector is always smaller than that at solenoid position for the solenoid focus

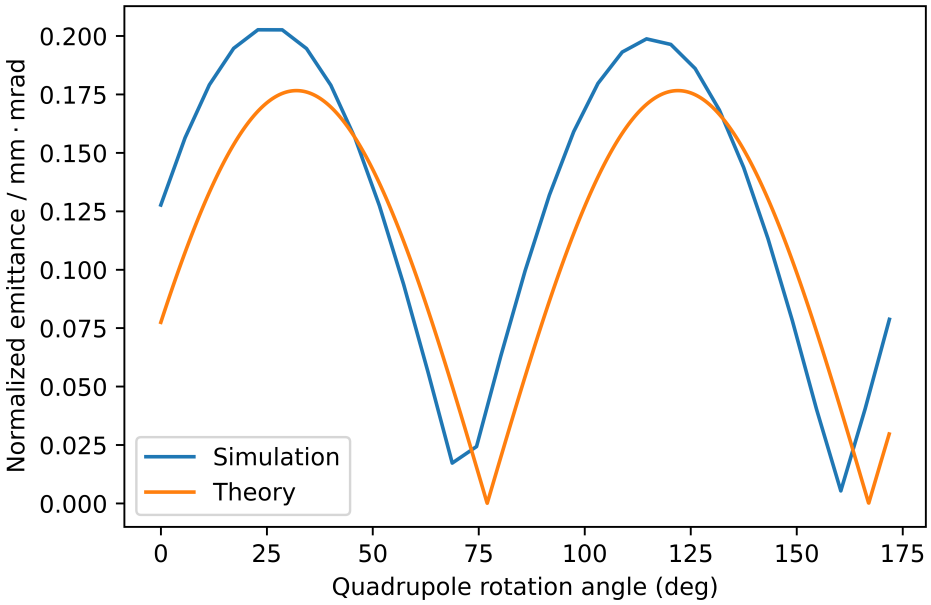

Fig. 4.12 Eq. 4.49 and beam transverse emittance from simulation in ASTRA. The quadrupole combined with the solenoid has an effective length 0.04 m, quadrupole strength 0.5 m^{-2}. The beam kinetic energy is 4 MeV with RMS size of 1 mm at the entrance of the solenoid and no energy spread. The maximum field of the solenoid is 0.171 T ($L_s = 0.04$ m, $K = 5.786\ \mathrm{m}^{-1}$).

the beam and the corrector is located in the focal length of it. In principle, if the corrector is located at the position beyond the focal length where the beam RMS size is as large as the solenoid position or larger, the effect of compensation to emittance is better under the same quadrupole strength of the corrector. However, the focal length of the solenoid is changeable with different necessaries. In the meantime, the corrector cannot compensate the emittance of beam between the solenoid and the corrector. Overall, the best corrector position is at the solenoid position or as close as possible to the solenoid.

It has been reported in [70, 71] that the sextupole field could introduce an extra transverse emittance. The sextupole emittance depends on the field's radial second-order derivative and effective field length. To analyze the influence of the sextupole field, one can ignore the fringe fields and assume that the beam transverse momentum is much smaller than the longitudinal momentum. From the Lorentz force equation, the force in x-direction is:

$$F_x = \frac{dp_x}{dt} = e\left(v_y B_z - v_z B_y\right). \tag{4.51}$$

Considering that $dz = \beta c dt$, the force becomes:

$$\frac{dp_x}{dz} = -eB_y. \tag{4.52}$$

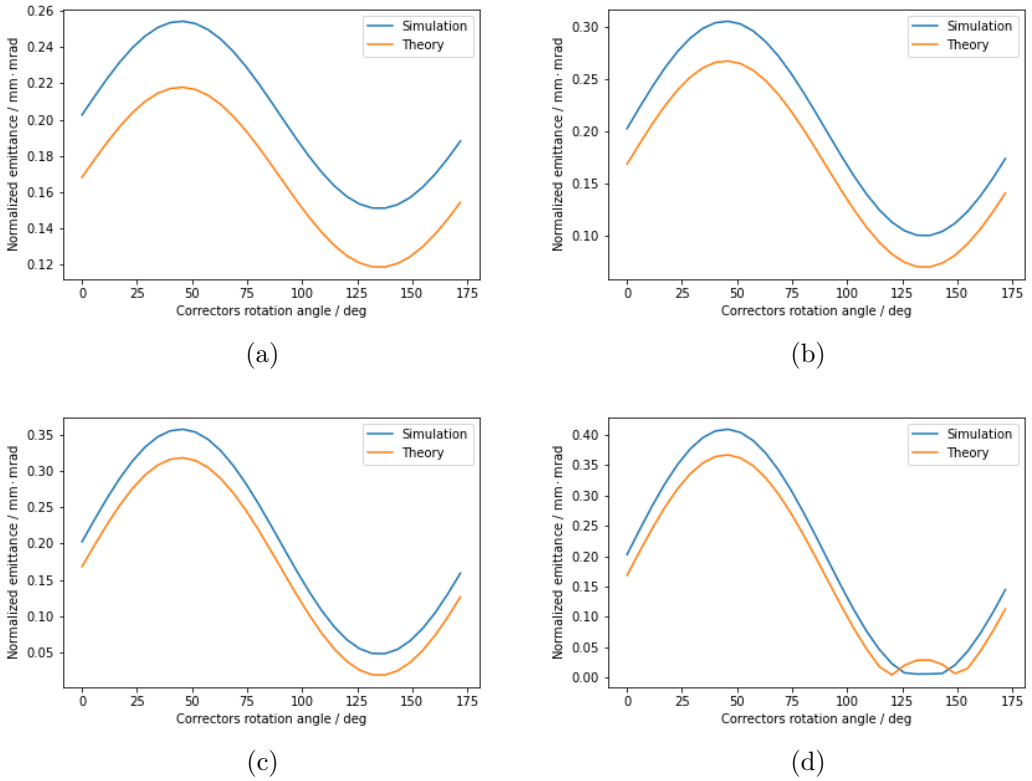

Fig. 4.13 Beam transverse emittance versus quadrupole angle from Eq. 4.50 and from simulation in ASTRA. The quadrupole combined with the solenoid has an effective length of 0.04 m, quadrupole strength 0.5 m^{-2}, and a rotation angle of 23 degrees. The corrector quadrupole has an effective length of 0.0627 m, located at 0.437 m downstream of the solenoid center. The beam kinetic energy is 4 MeV with a round beam of 1 mm RMS size at the entrance of the solenoid and no energy spread. The maximum field of the solenoid is 0.171 T ($L_s = 0.04$ m, $K = 5.786\ m^{-1}$).

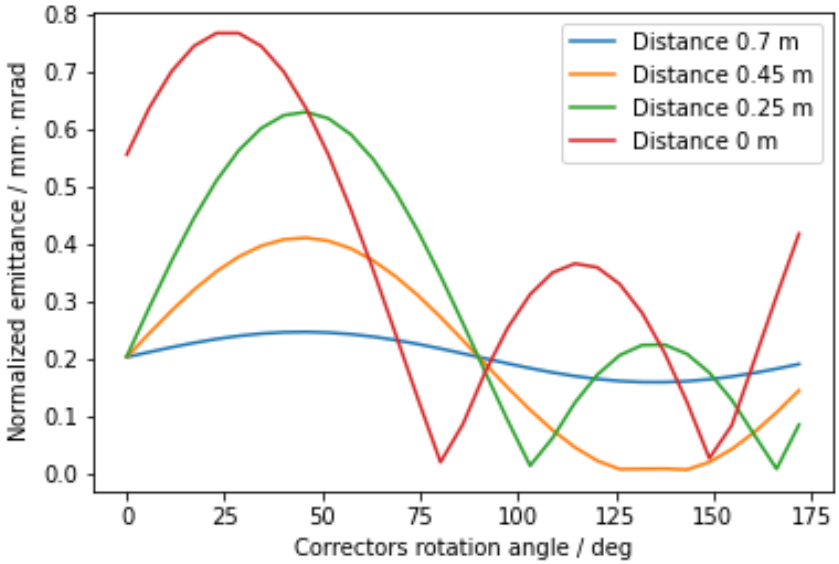

Fig. 4.14 Beam transverse emittance from simulation in ASTRA. The quadrupole combined with the solenoid has an effective length of 0.04 m, quadrupole strength 0.5 m^{-2}, and rotate the angle of 23 degrees. The beam kinetic energy is 4 MeV with round RMS 1 mm at the entrance of the solenoid and no energy spread. The maximum field of the solenoid is 0.171 T ($L_s = 0.04$ m, $K = 5.786\ \mathrm{m}^{-1}$). The corrector has an effective length of 0.0627 m, and focal length is 16 m.

The sextupole field in the y-component is [72]:

$$B_y(x,y) = \frac{1}{2}\frac{\partial^2 B_y}{\partial x^2}\bigg|_{x,y=0}\left(x^2 - y^2\right). \tag{4.53}$$

The beam transverse momentum from the sextupole field is given as:

$$\begin{aligned}\int_{p_x}^{p_x+\Delta p_x} dp_x = \Delta p_x &= -\frac{e}{2}\int_{-\infty}^{\infty}\frac{\partial^2 B_y}{\partial x^2}\bigg|_{x,y=0}\left(x^2 - y^2\right)dz \\ \Delta p_x(x,y) &= -\frac{e}{2}\frac{\partial^2 B_y}{\partial x^2}\bigg|_{x,y=0} L_{eff}\left(x^2 - y^2\right).\end{aligned} \tag{4.54}$$

For the beam with upright phase space, the emittance is

$$\varepsilon_n = \frac{\sigma_x \sigma_{p_x}}{mc}, \tag{4.55}$$

where σ_x is the beam RMS size in x direction and σ_{px} is the beam RMS momentum in x direction, which can be calculated as:

$$\sigma_{p_x}^2 = \frac{\int_{-\infty}^{\infty} \left[\Delta p_x(x, y=0)\right]^2 \rho(x) dx}{\int_{-\infty}^{\infty} \rho(x) dx}. \tag{4.56}$$

In the equation, $\rho(x)$ is the distribution of the beam, such as a Gaussian distribution $e^{-\frac{x^2}{2\sigma_x^2}}$ or an uniform distribution. Then the normalized emittance from the sextupole field for beam with Gaussian or uniform distribution is, respectively:

$$\begin{aligned} \Delta\varepsilon_{n,\text{ sextupole}} &= \frac{\sqrt{3}}{2}\sigma_x^3 \frac{e}{mc} L_{eff} \left.\frac{\partial^2 B_y}{\partial x^2}\right|_{x,y=0}, \\ \Delta\varepsilon_{n,\text{ sextupole}} &= \frac{1}{2}\sigma_x^3 \frac{e}{mc} L_{eff} \left.\frac{\partial^2 B_y}{\partial x^2}\right|_{x,y=0}. \end{aligned} \tag{4.57}$$

From Eq. 4.57, one can see that the emittance of sextupole field increases with the cube of beam RMS size and linear with the sextupole field effective length. If the beam RMS size is too large or the sextupole field is large, one should consider to install a sextupole downstream of the solenoid to cancel the influence of the sextupole field of the solenoid. The decrease of the second order differentiation of transverse magnetic field is helpful to suppress the influence of the sextupole field from the solenoid.

Chapter 5

Transverse Emittance Measurement

5.1 Overview

The methods which are widely used for transverse emittance measurements of electron beams can be divided into two groups: the magnetic field scan and the mask methods. The magnetic field scan methods, including solenoid scan, quadrupole scan, multi screen method, and tomographic phase space mapping, are based on the beam linear transport theory and can be applied for emittance dominated beams. The mask methods, including pepper pot method, multi-slit method and (single) slit-scan, utilize a mask with holes or slits to split the space charge dominated beam into small beamlets, which are then do not suffer from space charge.

The beam envelope equation is a suitable tool to define whether a beam is emittance dominated or space charge dominated. A definition of a propper parameter is in reference [73] in the paper by Anderson et al. For a relativistic beam in a drift space, the envelope equation is

$$\sigma_x'' = \frac{\varepsilon_n^2}{\gamma^2 \sigma_x^3} + \frac{I}{\gamma^3 I_0 \left(\sigma_x + \sigma_y\right)} \tag{5.1}$$

In this equation, σ_x and σ_y are the beam RMS size in horizontal and vertical directions. ε_n is the normalized beam emittance, I is the beam peak current, and γ is the Lorentz factor representing the beam energy. I_0 gives the characteristic current, as $\frac{ec}{r_e}$, about 17 kA. The two terms on the right side represent the emittance and the space charge effects. The ratio of the second term and the first term, R_0, can be used to evaluate the influence of space charge

$$R_0 = \frac{I \sigma_x^3}{\gamma I_0 \varepsilon_n^2 \left(\sigma_x + \sigma_y\right)}, \tag{5.2}$$

for the whole beam. This value is equivalent to another dimensionless intensity parameter in reference χ [74]. If $R_0 < 1$, the beam is considered to be emittance dominated. Otherwise, the space charge dominates the beam. However, even if the beam is emittance dominated, a remaining influence of space charge can appear unless $R_0 \ll 1$. The beamlets behind a pepper pot mask or slit mask become emittance dominated.

The quadrupole scan (solenoid scan is similar, except that the horizontal and vertical directions are coupled) and the slit-scan belong to the main topics in this thesis and are analyzed in detail. For the sake of completeness, here gives the multi screen method, the tomographic phase space mapping and the pepper pot method are shortly introduced.

5.1.1 Multi screen method

The multi screen method is based on the linear elements, such as normal quadrupoles, and at least three screens located at different positions in the beamline to record the size of the beam with different statues in phase space. It is equivalent to the traditional quadrupole scan instead of scanning one quadrupole focal strength. As Fig. 5.1 shows, the ideal situation is that one of the screen intercepts the beam waist and the beside screens give the size of the convergent beam and divergent beam. The quadrupoles in this process apply a sufficient and suitable phase-advance by a fixed focal strength. The advantage of the method is the simple operation and the flexible setup in the beamline.

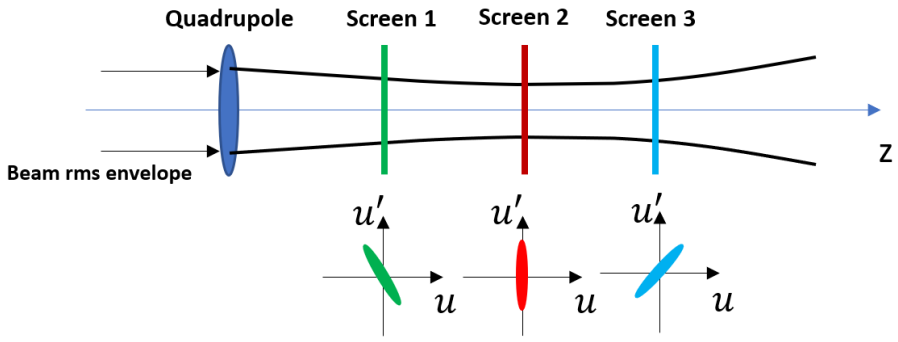

Fig. 5.1 Multi screen method frame.

5.1.2 Tomographic phase space mapping

The theory of tomographic phase space mapping is similar to the approach in computed tomography (CT). Mathematically, a n-dimensional distribution can be reconstructed from a set of its (n-1)-dimensional projections, applying Radon transform and inversion [75]. Several studies have been carried out to recover the beam phase space using CT, for instance 2-D phase space [76, 77, 78, 79] and 4-D phase space [80]. As mentioned before, according to Liouville's theorem, the particle density remains constant in phase space in linear transport systems without space charge effects. Assuming that there is no coupling between horizontal, vertical and longitudinal directions, the 2-D phase space density in each direction is a constant. In the linear beam transport, the transport matrices are affine transformations, such as rotation, expansion, shear, translation, or combinations of these. One can rotate the beam in phase space with a certain angle with a magnetic field, including quadrupole field and solenoid field, and calculate the transport matrix elements. The 1-D projection of the beam shape on the screen along the horizontal or vertical direction delivers a part of information of the beam phase space

at a certain angle. If the angle range and number of measurement points are sufficient, the beam phase space can be reconstructed by means of the Radon inversion transform.

Compared to quadrupole or solenoid field scan, the tomographic phase space mapping can give the details of beam phase space distribution, even for beams suffering the linear space charge [77]. The disadvantages of this method are the complex algorithm and the limitation due to the rotation angle range.

5.1.3 Pepper-pot method

The pepper-pot method applies a mask with holes and a screen [81, 82]. The setup frame is shown in Fig. 5.2. When the beam hits the mask, only the fractions of the beam at the hole positions can go through and form a pattern of beamlet distributions on the screen. From these distributions of beamlets and the pepper pot mask parameters, sizes and positions, one can recover the beam phase space in four dimensions. The advantage of pepper-pot method is that the coupled terms in the 4-D beam matrix can be determined. However, one of the disadvantages is the comparably low resolution of the beamlet images due to the low particle number in the beamlets. The second disadvantage is that the size and arrangement of the holes in one mask is fixed. This causes the limitations in the beam size and emittance which can be measured. Furthermore, the fabrication of the micrometer holes with large aspect ratio in high accuracy is difficult.

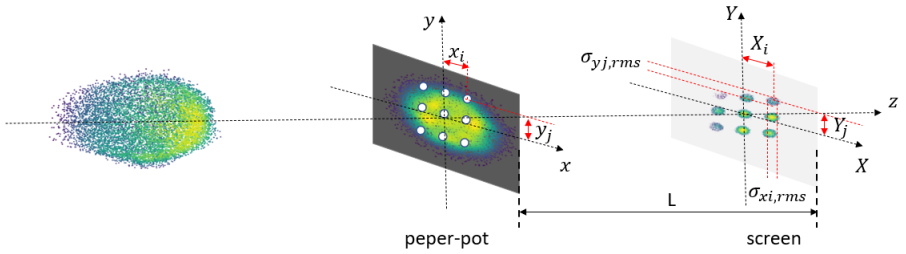

Fig. 5.2 Peper-pot method frame.

5.2 Quadrupole scan

5.2.1 Theory

As an important element in accelerator, quadrupole magnets serve for the transport of charged particle beams through beamlines by focusing and defocusing in transverse directions. Due to their high efficiency for focusing of charged particle beams with relativistic velocities, magnetic quadrupoles with current-carrying coils are widely applied in accelerators. As Fig. 5.3 (a) shows, a quadrupole consists of two pairs of opposing magnetic poles. Fig. 5.3 (b) shows the magnetic field distribution along the two axes, B_x is a linear function of y and B_y is a linear

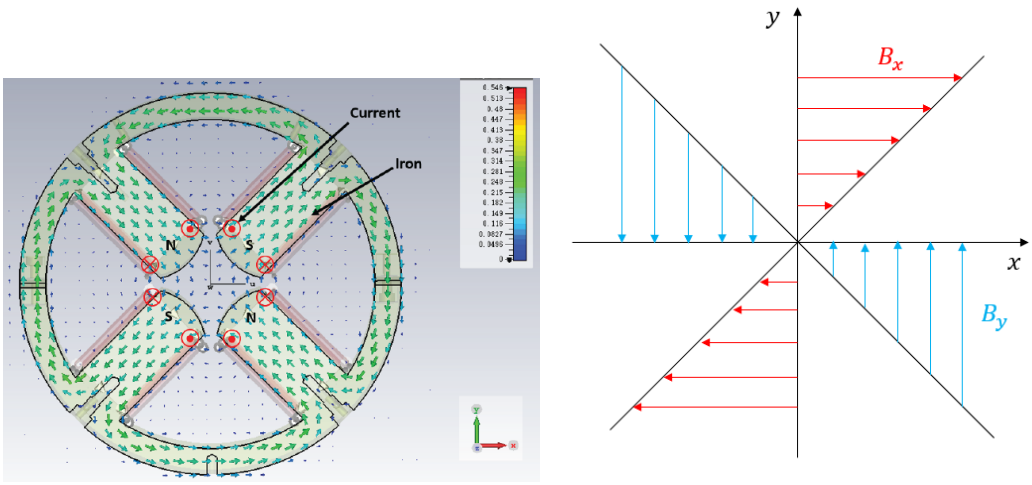

(a) (b)

Fig. 5.3 (a): Normal quadrupole magnet profile from simulation; (b): Quadrupole field along with the x and y axis.

function of x. The quantity g is the field gradient of the quadrupole with

$$\begin{aligned} B_x &= gy \\ B_y &= gx. \end{aligned} \tag{5.3}$$

Based on the magnetic gradient, quadrupole strength is defined as:

$$k = \frac{g}{B\rho}, \tag{5.4}$$

$B\rho$ is named the magnetic rigidity of the beam. The other basic parameter, quadrupole effective length, is defined as:

$$L_{eff} = \frac{\int g dz}{g_0} \; or \; \frac{\int k dz}{k_0}, \tag{5.5}$$

g_0 and k_0 are the maximum value of g and k. Fig. 5.4 shows the normalized field gradient along the z axis.

In linear transport theory, the normal quadrupole matrix in 4-D can be written as [72]:

$$\mathrm{M_q} = \begin{pmatrix} C_f & \frac{1}{\sqrt{k_f}} S_f & 0 & 0 \\ -\sqrt{k_f} S_f & C_f & 0 & 0 \\ 0 & 0 & C_d & \frac{1}{\sqrt{k_d}} S_d \\ 0 & 0 & \sqrt{k_d} S_d & C_d \end{pmatrix}$$

$$\begin{aligned} C_f = \cos(\sqrt{k_f} L_f)\,, \; S_f = \sin(\sqrt{k_f} L_f) \\ C_d = \cosh(\sqrt{k_d} L_d)\,, \; S_d = \sinh(\sqrt{k_d} L_d) \end{aligned} \tag{5.6}$$

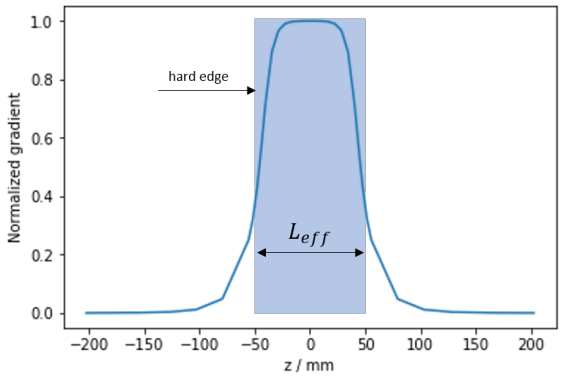

Fig. 5.4 Quadrupole magnetic field normalized gradient.

Here k_f and L_f are the quadrupole strength and effective length in focusing direction, k_d and L_d are the quadrupole strength and effective length in defocusing direction. The effective length incorporates the fringe field, but it is a constant for a certain quadrupole whatever it focuses or defocuses. A detailed analysis shows, that there is a small difference between these two values in different quadrupole field profiles, which will influence the quadrupole strength slightly[36].

$$L_{eff} = L_f = L_d, \tag{5.7}$$

$$k_{eff} = k_f = k_d. \tag{5.8}$$

In thin-lens approximation, suitable where the length of the quadrupole is small compared with the focus length ($L_{eff} \ll f$), the effective length can be set $L_{eff} \to 0$, while keeping the refractive power constant, such as,

$$\frac{1}{f} = k_{eff} L_{eff}. \tag{5.9}$$

The physical meaning of the thin-lens approximation is that the horizontal and vertical positions of the particles input and output from the quadrupole are the same.

The quadrupole scan frame is shown as Fig. 5.5. The beam RMS size is a function of the quadrupole focal strength. By fitting the function, one can obtain the beam parameters in phase space. The function can be derived from transport matrix. Consider the two beam matrices

$$\Sigma^q = \begin{pmatrix} \sigma_{11}^q & \sigma_{12}^q \\ \sigma_{12}^q & \sigma_{22}^q \end{pmatrix} \text{ and } \Sigma^s = \begin{pmatrix} \sigma_{11}^s & \sigma_{12}^s \\ \sigma_{12}^s & \sigma_{22}^s, \end{pmatrix},$$

the first one characterizes the beam in front of the quadrupole and the second at the screen, $\sigma_{11} = \langle x_i^2 \rangle = \varepsilon\beta$, $\sigma_{22} = \langle x_i^{'2} \rangle = \varepsilon\gamma$, $\sigma_{12} = \sigma_{21} = \langle x_i x_i^{'} \rangle = -\varepsilon\alpha$. β, γ and α are Twiss parameters. The transport matrix from the quadrupole to the screen is:

$$\mathrm{M} = \begin{pmatrix} 1 & d \\ 0 & 1 \end{pmatrix} \mathrm{M_u},$$

$\mathrm{M_u}$ is the 2-D matrix of quadrupole in horizontal or vertical direction. Then:

$$\Sigma^s = \mathrm{M}\Sigma^q\mathrm{M}^{\mathrm{T}}. \tag{5.10}$$

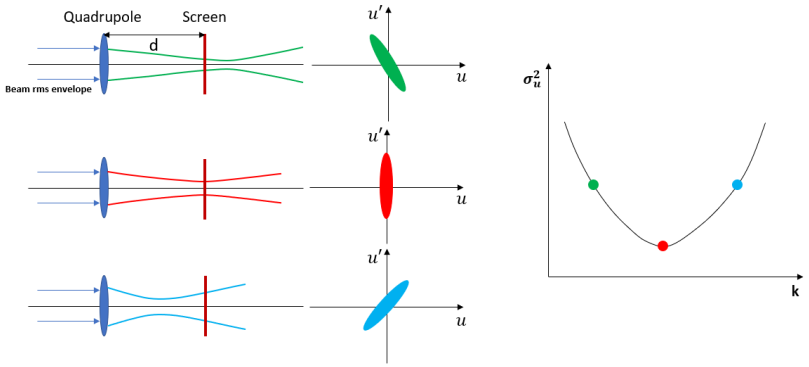

Fig. 5.5 Quadrupole scan frame.

One can obtain the following equations in the thin-lens approximation:

$$\sigma_{11}^s = (\sigma_{11}^q d^2)k^2 L_{eff}^2 + (-2d\sigma_{11}^q - 2d^2\sigma_{12}^q)kL_{eff} + \sigma_{11}^q + 2d\sigma_{12}^q + d^2\sigma_{22}^q. \tag{5.11}$$

And in the general case for focusing:

$$\begin{aligned}\sigma_{11}^s =&(\sigma_{11}^q + d^2\sigma_{22}^q + 2d\sigma_{12}^q)C_f^2 - \frac{2d\sigma_{11}^q + 2d^2\sigma_{12}^2}{L_f}(\sqrt{k}L_f)S_fC_f + \frac{d^2\sigma_{11}^q}{L_f^2}(\sqrt{k}L_f)^2S_f^2 \\ &+ \frac{L_f^2\sigma_{22}^q}{(\sqrt{k}L_f)^2}S_f^2 + (2d\sigma_{22}^q + 2\sigma_{12}^q)L_f\frac{1}{\sqrt{k}L_f}C_fS_f - 2d\sigma_{12}^qS_f^2\end{aligned} \tag{5.12}$$

and defocusing:

$$\begin{aligned}\sigma_{11}^s =&(\sigma_{11}^q + d^2\sigma_{22}^q + 2d\sigma_{12}^q)C_d^2 + \frac{2d\sigma_{11}^q + 2d^2\sigma_{12}^q}{L_d}(\sqrt{k}L_d)S_dC_d + \frac{d^2\sigma_{11}^q}{L_d^2}(\sqrt{k}L_d)^2S_d^2 \\ &+ \frac{L_d^2\sigma_{22}^q}{(\sqrt{k}L_d)^2}S_d^2 + (2d\sigma_{22}^q + 2\sigma_{12}^q)L_d\frac{1}{\sqrt{k}L_d}S_dC_d + 2d\sigma_{12}^qS_d^2\end{aligned} \tag{5.13}$$

The normalized emittance can be calculated by

$$\varepsilon_n = \beta\gamma\det(\Sigma^q) = \beta\gamma\sqrt{\sigma_{11}^q\sigma_{22}^q - {\sigma_{12}^q}^2}. \tag{5.14}$$

For the thin-lens approximation, by defining the abbreviations $A = \sigma_{11}^q d^2$, $B = -2d\sigma_{11}^q - 2d^2\sigma_{12}^q$, $C = \sigma_{11}^q + 2d\sigma_{12}^q + d^2\sigma_{22}^q$, the Eq. 5.14 can be simplified to

$$\varepsilon_n = \beta\gamma\frac{1}{d^2}\sqrt{AC - \frac{1}{4}B^2}. \tag{5.15}$$

Compared with Eq. 5.12 and Eq. 5.13, the thin-lens approximation Eq. 5.11 is much simpler and easier for fitting. However, the thin-lens approximation is in high uncertainty, if the drift distance is too short or the quadrupole strength is too large, which is discussed in section 5.2.2.

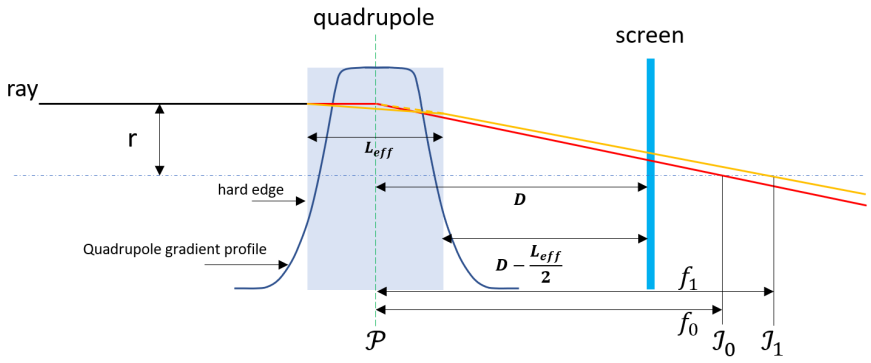

Fig. 5.6 Determining the drift distance. The red and original lines are from the thin-lens approximation and thick-lens, respectively. The original dash line is the extension of the original line. $\mathcal{P}$ is the principal plane of the thin-lens approximation. But the principal plane of the thick-lens is almost the same position in two orders approximation. $\mathcal{I}_0$ and $\mathcal{I}_1$ are the focal plane of the thin-lens approximation and thick-lens with focal length f_0 and f_1, respectively. D is the drift distance of the thin-lens approximation, and $D - \frac{L_{eff}}{2}$ is the drift distance of the thick-lens.

To find the quadrupole strength scan scale quickly, one can calculate the partial derivatives of σ_{11}^s to kL_{eff} in Eq. 5.11 :

$$\frac{\partial \sigma_{11}^s}{\partial (kL_{eff})} = 2\sigma_{11}^q d^2 kL_{eff} - 2\left(\sigma_{11}^q d + \sigma_{12}^q d^2\right) = 0, \tag{5.16}$$

then

$$(kL_{eff})_{\min} = \frac{1}{d} + \frac{\sigma_{12}^q}{\sigma_{11}^q}. \tag{5.17}$$

This value is related to the inherent beam parameters. It is easy to calculate the focal strength in simulation, which gives a good reference point for the scanning. Although it is the value for the thin-lens approximation, it is also close to this point in the general cases. But it is much more complex to derive an expression and to calculate a value. However, when the space charge is taken into consideration, this value will be shifted.

5.2.2 Quadrupole scan simulation

In section 5.2.1, the basic idea of quadrupole scan for emittance measurements has been introduced. In this section, the simulation and the error analysis of this method will be given. At the ELBE facility, the effective length of the quadrupole is 0.1 m, and in the simulation, this value is used. The beam's kinetic energy is 4 MeV, and the bunch charge is 200 pC. Three aspects are discussed in this section: drift distance between the quadrupole and the screen, beam space charge, and the equations used for fitting. The drift distance between the quadrupole and the screen is defined as the distance from the center of the quadrupole to the screen for thin-lens. The drift distance is from the end of the quadrupole to the screen for thick quadrupole, shown as Fig. 5.6.

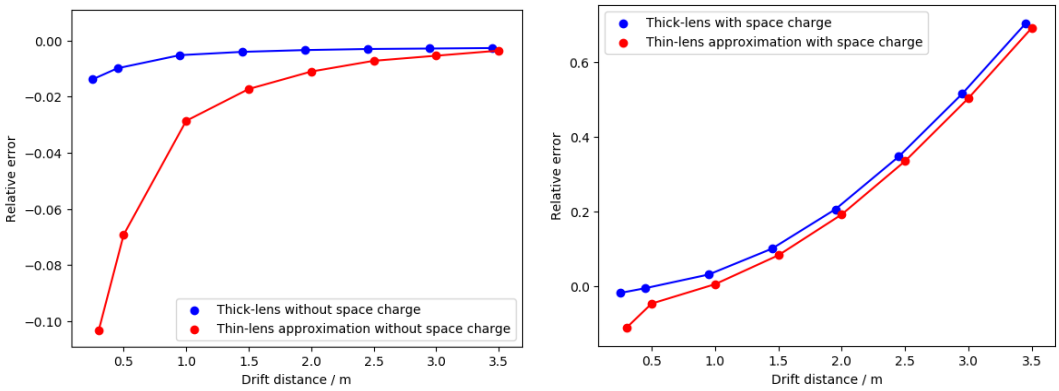

(a) (b)

Fig. 5.7 Normalized emittance relative error vs drift distance. In (a) it ignores the space charge. In (b) it includes the space charge. In the simulation, the bunch charge is 50 pC, at the quadrupole position the original beam normalized emittance is 1.6506 mm · mrad, kinetic energy is 3.98 MeV, and beam RMS size at quadrupole position is 1.2761 mm. The relative error is defined as $(\varepsilon_{n,cal} - \varepsilon_{n,ori})/\varepsilon_{n,ori}$, where the $\varepsilon_{n,cal}$ is normalized emittance from the quadrupole scan, and $\varepsilon_{n,ori}$ is the normalized emittance at the quadrupole position.

In the simulation, the influence from thin-lens approximation and space charge are considered. From Fig. 5.7 (a), one can find that if the space charge is ignored, the emittance relative error from thick-lens fitting is small for short drift distance and nearly independent of the drift distance for longer drift distance. When the drift distance is shorter than 0.5 m, the relative error is larger than 1%. The reason maybe come from the quadrupole fringe field. For thin-lens approximation, the relative error is similar to the thick-lens, but larger than the thick-lens, especially for the distance less than 1 m. This is because, for short drift distance, the quadrupole needs higher k values to complete the scan, and the thin-lens condition, $l \ll d$, $\sqrt{k}l \to 0$, is not satisfied anymore. The details of all the fitting are in Fig. 5.8. When the space charge is considered in the simulation, it shows that the relative error become larger along with the drift distance. Fig. 5.8 shows the fitting curves with and without space charge. In the fitting curves with the thick-lens approach, the points at the right side of the minimum point are parallel for the with and without space charge. However, the points on the left side have a big difference, especially for large drift distances. It indicates that for a quadrupole scan, the influence of the space charge is on the left side of the minimum points rather than the right side. When the beam is in the left point situation, it is a more space-charge-dominated beam. When the beam size crosses the minimum point, it is a more emittance-dominated beam. This is consistent with the conclusion from S. G. Anderson and J. B. Rosenzweig in reference [73], where they obtain it from the beam envelope equations.

One thing should be noticed is that the space charge destroys the symmetric of the fitting points. Here, the symmetric means that the fitting from the left and right points are the same. Fig. 5.9 shows the fitting curves from left and right half points. When considering the space charge, the two curves have a noticeable difference, which results in the difference of calculated emittance from fitting parameters.

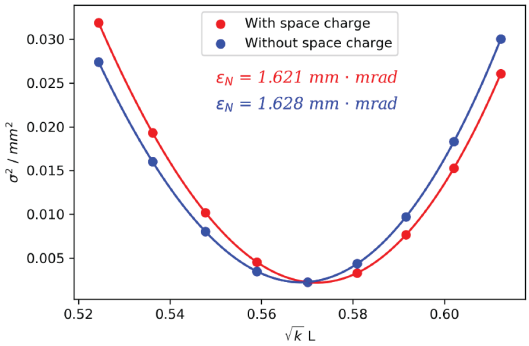

(a) Drift distance 0.25 m and Equ. 5.12

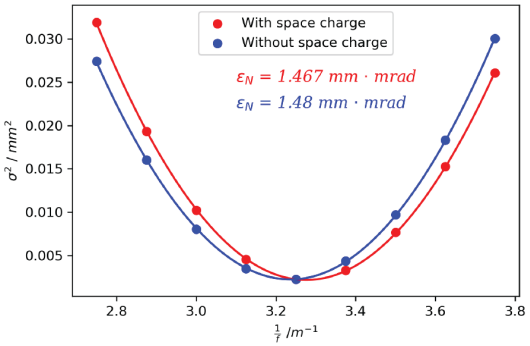

(b) Drift distance 0.3 m and Equ. 5.11

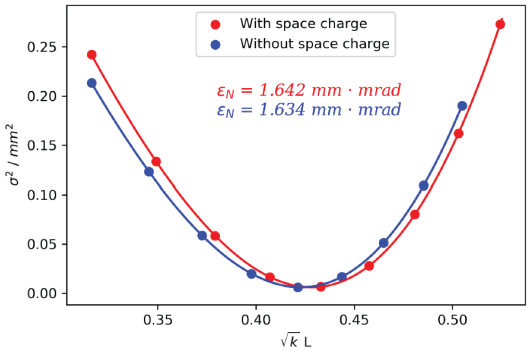

(c) Drift distance 0.45 m and Equ. 5.12

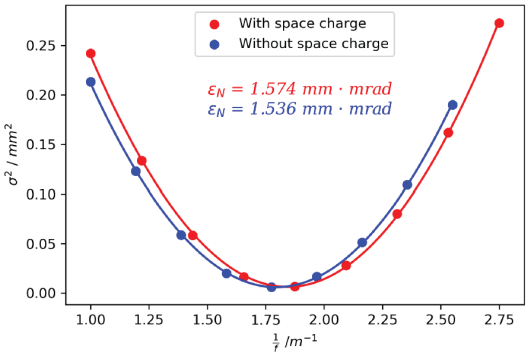

(d) Drift distance 0.5 m and Equ. 5.11

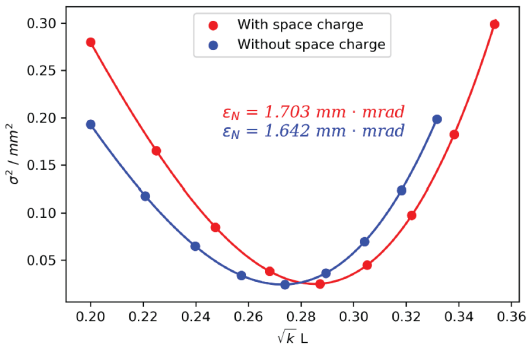

(e) Drift distance 0.95 m and Equ. 5.12

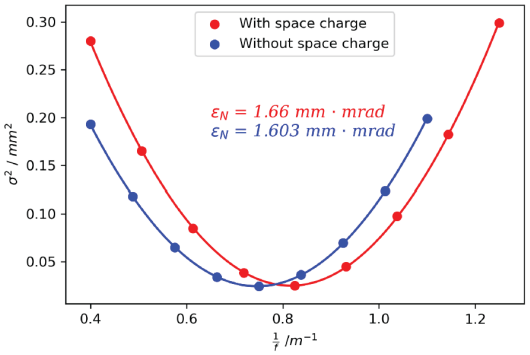

(f) Drift distance 1.0 m and Equ. 5.11

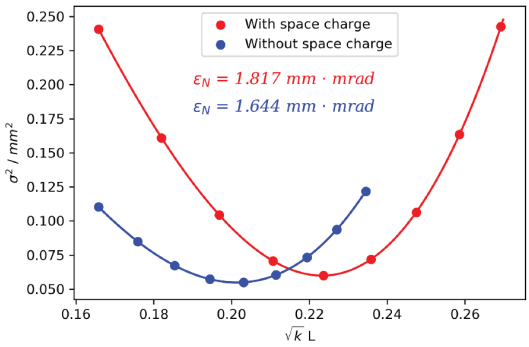

(g) Drift distance 1.45 m and Equ. 5.12

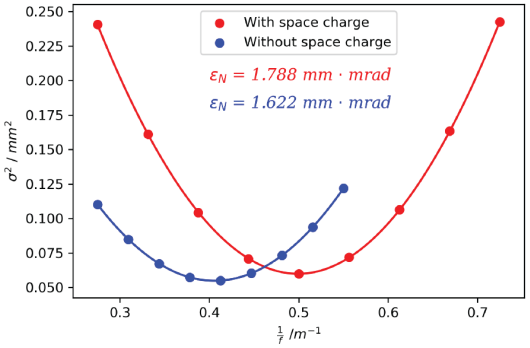

(h) Drift distance 1.5 m and Equ. 5.11

Fig. 5.8 In the simulation, the parameters at the quadrupole station are the same as Fig. 5.7.

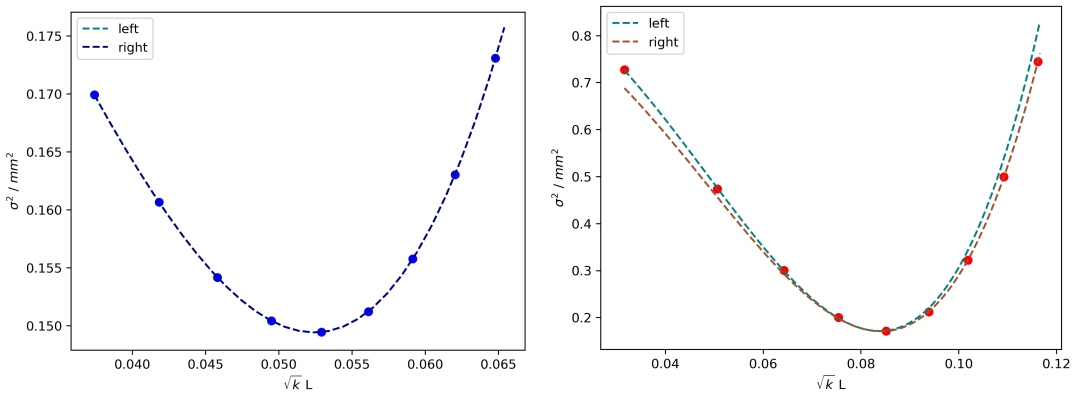

(a) (b)

Fig. 5.9 In figure (a), the simulation has no space charge; In figure (b), the simulation has space charge.

5.2.3 Error analysis

The error of quadrupole scan has two parts. The first part is from the fitting error and the second part is from the quadrupole focal strength error. The fitting method usually used is the linear least squares analysis [83]. Assume that one obtains n groups of data about quadrupole scan. $\boldsymbol{\sigma}^{se}$ is the beam RMS size on the screen with $(n \times 1)$ dimension from experiments, $\boldsymbol{\sigma}^{f}$ is the beam RMS size on the screen with $(n \times 1)$ dimension from fitting, $\boldsymbol{X}$ is the matrix with $(n \times 3)$ dimension and relative to the quadrupole focal strength, $\boldsymbol{\beta}$ is the coefficient matrix with (3×1) dimension. In thin-lens approximation, $\boldsymbol{\beta} = [A, B, C]^T$. Then rewrite Eq. 5.11 as:

$$\boldsymbol{\sigma}^{f}(\boldsymbol{\beta}) = \boldsymbol{X}\boldsymbol{\beta}, \tag{5.18}$$

the rest term is

$$\boldsymbol{R}(\boldsymbol{\beta}) = \boldsymbol{\sigma}^{se} - \boldsymbol{\sigma}^{f}(\boldsymbol{\beta}), \tag{5.19}$$

so the function should be minimized is

$$\boldsymbol{S}(\boldsymbol{\beta}) = \|\boldsymbol{R}(\boldsymbol{\beta})\|^2. \tag{5.20}$$

The minimum can be calculate from the derivatives of $\boldsymbol{S}(\boldsymbol{\beta})$ with $\boldsymbol{\beta}$:

$$\frac{\mathrm{d}\boldsymbol{S}(\boldsymbol{\beta})}{\mathrm{d}\boldsymbol{\beta}} = 0. \tag{5.21}$$

Then the optimization $\boldsymbol{\beta} = [A, B, C]^T$ will be obtained. The uncertainty of $\boldsymbol{\beta}$ can be given from Jacobian matrix of the fitting and will transform to the emittance error from Eq. 5.15. This error can be analyzed as following:

$$\frac{\partial \varepsilon}{\partial A} = \frac{1}{2d^4\varepsilon}C, \tag{5.22}$$

$$\frac{\partial \varepsilon}{\partial B} = \frac{1}{2d^4\varepsilon}\left(-\frac{1}{2}B\right), \tag{5.23}$$

$$\frac{\partial \varepsilon}{\partial C} = \frac{1}{2d^4\varepsilon}A, \tag{5.24}$$

$$\begin{aligned}\Delta\varepsilon_f^2 = &\left(\frac{\partial \varepsilon}{\partial A}\right)^2 \Delta A^2 + \left(\frac{\partial \varepsilon}{\partial B}\right)^2 \Delta B^2 + \left(\frac{\partial \varepsilon}{\partial C}\right)^2 \Delta C^2 + 2\frac{\partial \varepsilon}{\partial A}\frac{\partial \varepsilon}{\partial B}\Delta A \cdot \Delta B \cdot \sigma_{ab} \\ &+2\frac{\partial \varepsilon}{\partial A}\frac{\partial \varepsilon}{\partial C}\Delta A \cdot \Delta C \cdot \sigma_{ac} + 2\frac{\partial \varepsilon}{\partial B}\frac{\partial \varepsilon}{\partial C}\Delta B \cdot \Delta C \cdot \sigma_{bc}.\end{aligned} \tag{5.25}$$

Here ε is the geometric emittance, σ_{ab}, σ_{ac} and σ_{bc} represent the covariance between A, B and C each other and can be obtained from the fitting coefficients. For thick-lens equation, the analysis is totally the same.

As mentioned in quadrupole calibration part, the quadrupole focal strength is not always the same as the theory. The focal strength uncertainty will influence the emittance calculation. Assume that the quadrupole strength used for calculation is k_r and the real one is k_0,

$$k_r = (1 + \delta_k)k_0, \tag{5.26}$$

where δ_k is the quadrupole strength error. Adding this factor in Eq. 5.11 and Eq. 5.15, one can calculate the emittance error from quadrupole focal strength uncertainty is:

$$\Delta\varepsilon_k = \delta_k. \tag{5.27}$$

This conclusion is strictly from the thin-lens approximation fitting equation, but for thick-lens, it is also a good approximation from simulation results. So the total quadrupole scan error is:

$$\Delta\varepsilon = \sqrt{\Delta\varepsilon_f^2 + \Delta\varepsilon_k^2}. \tag{5.28}$$

5.3 Slit-scan and error analysis

5.3.1 Theory

The last section shows that when the beam is space charge dominated, the quadrupole scan method will give a significant error. The other disadvantage is that quadrupole scan can only give the value of beam emittance but not the details of the beam transverse phase space. To observe the details of the beam transverse phase space, people develop several methods, including slit-scan, pepper-pot, and quadrupole tomography. The slit-scan and multi-slit techniques are widely used for measuring the transverse phase space and transverse projected emittance of high-brightness electron beams produced by photo injectors. In these methods, the space charge dominated beam is split into many small and emittance dominated beamlets using one mask with one or several narrow slits and the beamlets drift from mask position to a screen, as it is shown in Fig. 5.10. The analysis works in the same way for both kinds, single slit-scan and multi-slit mask.

For the beamlets a linear beam transport between the slit mask and the observation screen can be described by the transport matrix:

$$\begin{pmatrix} x_{\text{screen}} \\ x'_{\text{screen}} \end{pmatrix} = \begin{pmatrix} 1 & L \\ 0 & 1 \end{pmatrix} \begin{pmatrix} x_{\text{slit}} \\ x'_{\text{slit}} \end{pmatrix} \tag{5.29}$$

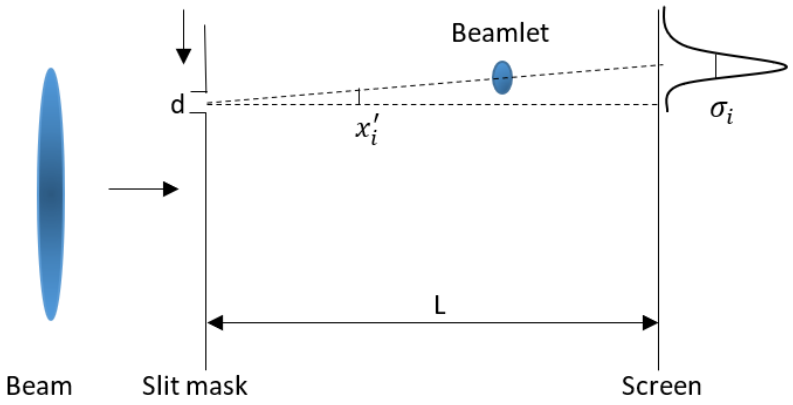

Fig. 5.10 Illustration of single-slit scan emittance measurement scheme.

Furthermore, the particle divergence is transferred to a position distribution. The transverse emittance ε_{rms} is defined as:

$$\varepsilon_{rms} = \sqrt{\langle x^2 \rangle \langle x'^2 \rangle - \langle xx' \rangle^2} \tag{5.30}$$

A normalized transverse emittance ε_{rms} can be defined as

$$\varepsilon_{rms} = \frac{p_z}{m_0 c} \sqrt{\langle x^2 \rangle \langle x'^2 \rangle - \langle xx' \rangle^2} \tag{5.31}$$

Here $\langle x^2 \rangle$, $\langle x'^2 \rangle$, $\langle xx' \rangle$, x' are defined based on the particle distribution $\rho(x, x')$:

$$\begin{gathered} \left\langle x^2 \right\rangle = \int \rho(x - \langle x \rangle)^2 dx dx', \quad \left\langle x'^2 \right\rangle = \int \rho \left(x' - \langle x' \rangle\right)^2 dx dx' \\ \langle xx' \rangle = \int \rho(x - \langle x \rangle) \left(x' - \langle x' \rangle\right) dx dx', x' = \frac{p_x}{p_z} \end{gathered} \tag{5.32}$$

where p_x is the beam horizontal momentum, p_z is the beam longitudinal momentum and approximately equal to beam total momentum here, m_0 is the rest mass of an electron, c is the speed of light. In the slit-scan case, the $\langle\ \rangle$ is related to an average over the beamlets and n_i is the particle intensity through the slit at i-th position. The bunch center at slit position is $\langle x \rangle = \frac{\sum n_i x_{si}}{\sum n_i}$, and x_{si} is the slit coordinate at ith position. The beam size at the slit plane is $\langle x^2 \rangle = \frac{\sum n_i (x_{si} - \langle x \rangle)^2}{\sum n_i}$. The bunch average divergence is $\langle x' \rangle = \frac{\sum n_i x_i'}{\sum n_i}$, and x_i' is the i-th slit position's average divergence which can be obtained by $x_i' = \frac{\langle x_{sci} \rangle - x_{si}}{L}$, here $\langle x_{sci} \rangle$ is the position of the i-th beamlet center on the screen, and L is the drift distance from the slit mask to the screen. The i-th beamlet divergence is $\sigma_i'^2 = \frac{\sigma_i^2 - \frac{d^2}{12}}{L^2}$, and σ_i is the i-th beamlet size on the screen and d is the slit size. The quantities in Eq. 5.32 can now be expressed by the values measured at the screen:

$$\left\langle x'^2 \right\rangle = \frac{\sum \left[n_i \sigma_i'^2 + n_i \left(\langle x_i' \rangle - \langle x' \rangle \right)^2 \right]}{\sum n_i}, \tag{5.33}$$

$$\langle xx' \rangle = \frac{\sum n_i x_{si} \langle x_i' \rangle}{\sum n_i}. \tag{5.34}$$

5.3.2 Beamlet image processing by machine learning

Image processing plays a vital role in the slit-scan emittance measurements. In our experiment, the beamlet images are obtained in a given time interval from the camera while the slit is continuously moving. Usually, tens to one hundred images will be stored for one measurement. The first task is to select the images which contain beamlet information frome those which contain noise only. The second task is the improvement of the images with beamlet information by filtering the noise from the relevant beamlet signals. The traditional method is a manual selection or a Gaussian fitting to distinguish the images with beamlet and with noise only. A median filter and complex processing based on the two-dimensional beamlet images can decrease the noise and improve the signal-noise ratio. Although these methods work well and decrease the noise effectively, they are time-consuming. The success of machine learning applications in nature images classification and filter noise [84, 85] encourage us to try it in beamlet image analysis.

The definition of machine learning is that a computer algorithm can learn some rules automatically from the already known data or experiment and can make predictions or decisions from new experimental data or other information [86]. Until now, no single model is universal for all data and applications. Every model is based on a particular class of dataset, and after training, it is only suited for this kind of data. As an example for a machine learning model, an artificial neural network is shown in Fig. 5.11 which consists of an input layer, hidden layers and an output layer. The input data should have the same standard form in all datasets for one model, whereas the output data can be an alloncation into categories, a value, an image, or something else. A matrix connects the hidden layers, depending on the size with tens or thousands of parameters, called weights, which should be learned from training. In a learning process the values of these weights are determined by means of training datasets for which the expected output results are given. After that, the internal parameters of the hidden layers are fixed and stored for use in applications.

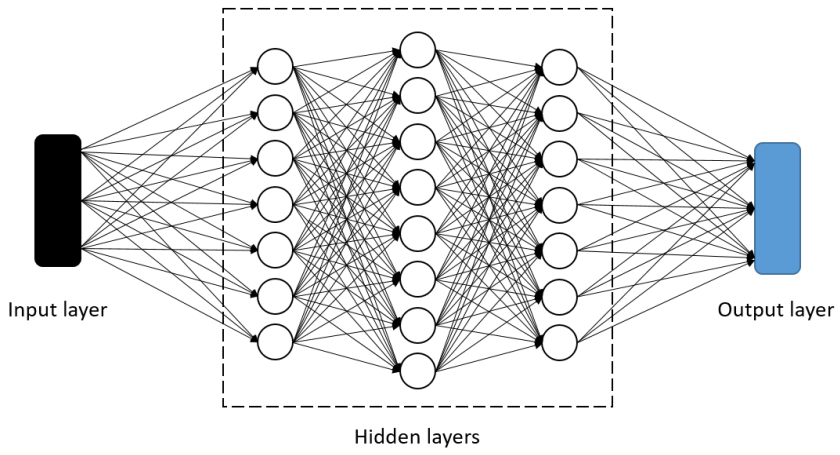

Fig. 5.11 Basic structure of an artificial network for machine learning.

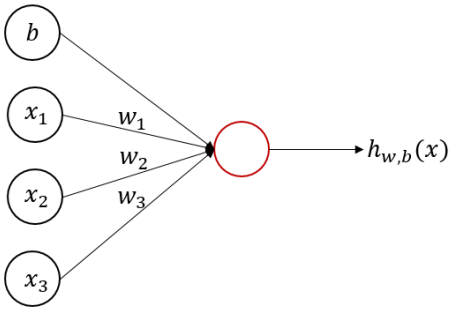

Fig. 5.12 Model of a single neuron as basic unit of a machine learning network.

5.3.3 Basic model of machine learning

At present, one of the most popular and powerful network is neuron connection network connection, which is similar to our Neuron in the brain. Reference [87] gives an example to explain how it works. The basic unit is a single neuron shown in Fig. 5.12. The input vector is $x = (b, x_1, x_2, x_3)^T$, in which b is bias term and usually as one. The weight vector is $w = (1, w_1, w_2, w_3)^T$ for different input terms. The output is $h_{w,b}(x) = f\left(w^T x\right) = f\left(\sum_{i=1}^{3} w_i x_i + b\right)$, where $f : R \mapsto R$ is called the activation function. There are several different activation functions which are used in neural network models, but in this thesis we have chosen the rectified linear unit (ReLU) function:

$$f(x) = max\{0, x\}. \tag{5.35}$$

A plot of the ReLU function is presented in Fig. 5.13. The ReLU function is defined in the set of real numbers R and the output interval is $(0, \infty)$.

It introduces how the neutral network connects and works between the hidden layers at a simple example with three layers, as shown in Fig. 5.14. This neural network has the parameters $(w^{(1)}, b^{(1)}, w^{(2)}, b^{(2)})$. The element $w_{ij}^{(l)}$ in $w^{(1)}$ denomnates the weight of the connection of the unit j of l-th layer and unit i of $l+1$-th layer. $a_i^{(l)}$ is the activation (output value) of unit i in

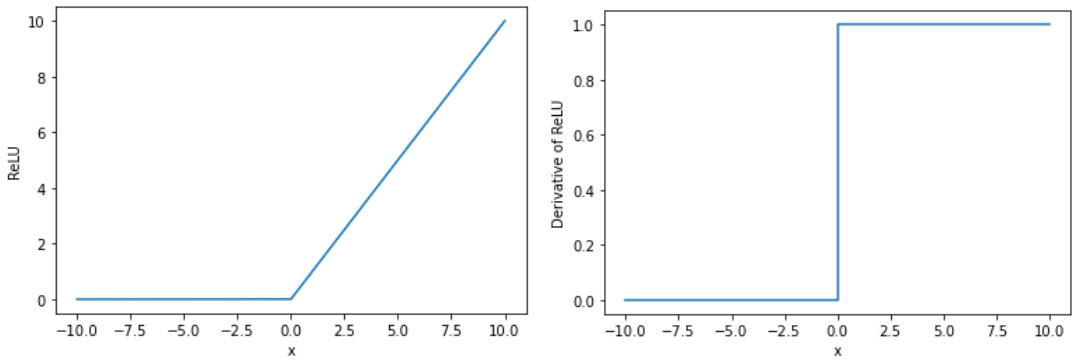

(a) (b)

Fig. 5.13 (a) is the ReLU function, and (b) is the derivative of ReLU function.

l-th layer. Then this neural network can be described as equations:

$$a_1^{(2)} = f\left(w_{11}^{(1)}x_1 + w_{12}^{(1)}x_2 + w_{13}^{(1)}x_3 + b_1^{(1)}\right) \tag{5.36}$$

$$a_2^{(2)} = f\left(w_{21}^{(1)}x_1 + w_{22}^{(1)}x_2 + w_{23}^{(1)}x_3 + b_2^{(1)}\right) \tag{5.37}$$

$$a_3^{(2)} = f\left(w_{31}^{(1)}x_1 + w_{32}^{(1)}x_2 + w_{33}^{(1)}x_3 + b_3^{(1)}\right) \tag{5.38}$$

$$h_{w,b}(x) = a_1^{(3)} = f\left(w_{11}^{(2)}a_1^{(2)} + w_{12}^{(2)}a_2^{(2)} + w_{13}^{(2)}a_3^{(2)} + b_1^{(2)}\right). \tag{5.39}$$

The supervised learning (SL) network can learn a function to map an input and output based on the foregone input-output pairs or experiences. One input-output pair is called one case. An input data is typically a vector or matrix. A desired output is usually named the label or supervisory signal of the input. A dataset consist of a large number of cases, and is defined as $\{(x^{(1)}, y^{(1)}), (x^{(2)}, y^{(2)}), \ldots, (x^{(n)}, y^{(n)})\}$ with n cases. One needs a function to estimate the difference between the outputs and labels, called the cost function. There is no one unique cost function for universal datasets, and one should define it by oneself depending on the solving problem. One of the widely used cost functions is:

$$J(W, b; x, y) = \frac{1}{2}\left\|h_{W,b}(x) - y\right\|^2. \tag{5.40}$$

To avoid overfitting, people will add a regularization term which tends to decrease the magnitude of the weights with parameter λ, written as:

$$J(w, b) = \left[\frac{1}{n}\sum_{i=1}^{n} J\left(w, b; x^{(i)}, y^{(i)}\right)\right] + \frac{\lambda}{2}\sum_{l=1}^{n_l-1}\sum_{i=1}^{s_l}\sum_{j=1}^{s_{l+1}}\left(w_{ji}^{(l)}\right)^2. \tag{5.41}$$

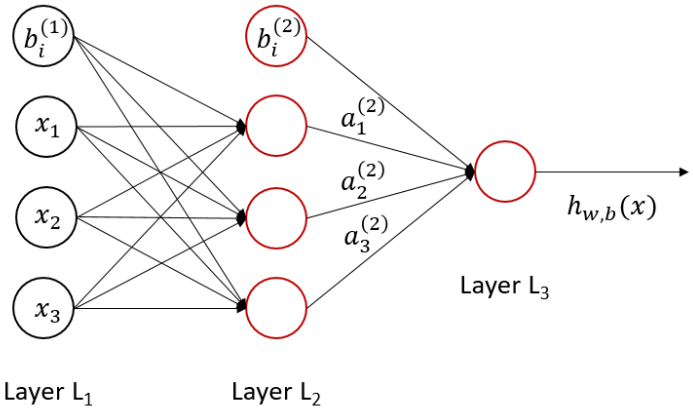

Fig. 5.14 Structure of a simple neural network with one hidden layer.

To minimize the cost function $J(w,b)$, the weights and biases will be improved as follow:

$$\begin{aligned} w_{ij}^{(l)} &:= w_{ij}^{(l)} - \alpha \frac{\partial}{\partial w_{ij}^{(l)}} J(w,b) \\ b_{i}^{(l)} &:= b_{i}^{(l)} - \alpha \frac{\partial}{\partial b_{i}^{(l)}} J(w,b). \end{aligned} \tag{5.42}$$

In the Eq. 5.42, α is the learning rate which is a hyperparameter and should be adjusted manually during training. Now we can describe the whole algorithm as the following steps:

- 1. Set the weight step δw, and bias step δb to zero (matrix or vector) for all layer l;
- 2. For i from 0 to n:
- 2a. Use backpropagation to compute $\Delta_{w^{(l)}} J(W,b;x,y)$ and $\Delta_{b^{(l)}} J(W,b;x,y)$;
- 2b. Set $w^{(l)} = w^{(l)} + \Delta_{w^{(l)}} J(W,b;x,y)$ and $b^{(l)} = b^{(l)} + \Delta_{b^{(l)}} J(W,b;x,y)$;
- 3. Update the parameters:

  $w^{(l)} = w^{(l)} - \alpha[(\frac{1}{n}\Delta w^{(l)}) + \lambda w^{(l)}]$;

  $b^{(l)} = b^{(l)} - \alpha[\frac{1}{n}\Delta b^{(l)}]$.

Some basic concepts in training and evaluation

To make the next part more understandable, here are four basic concepts often used in the machine learning field:

- Loss function is defined with respect to a single training case. It measures the error between the output and the label on a single training case.
- Cost function measures the error in an entire training set and is the average of the loss function. However, sometimes the loss function and cost function are synonymous in papers. In the following figures, the y label, "Loss", always means the cost function.
- Epoch indicates one time passes of the entire training dataset the whole algorithm, including one front propagation and one backpropagation, has been completed.
- Batch size means the number of cases in a training dataset utilized in one iteration.

In principle, the loss function will converge the increasing of the number of epochs. However, there are several types of loss function value verse epochs overtraining, such as underfitting and overfitting. Many publications from computer science have talked about this topic. Generally, when the training and testing errors are both high, the model is said to be underfitted. There are several reasons resulting in underfitting problems, such as the model algorithm is too simple or the training epoch is not enough, shown as Fig. 5.15 (a). So one should boost the machine learning algorithm in the model and enlarge the training epochs. When the training error continues decreasing, while the testing error is increasing and the gap between each other becomes larger, shown as Fig. 5.15 (b), the model is called overfitting. One reason for overfitting is that the training data has a different distribution than the testing dataset, and the former is

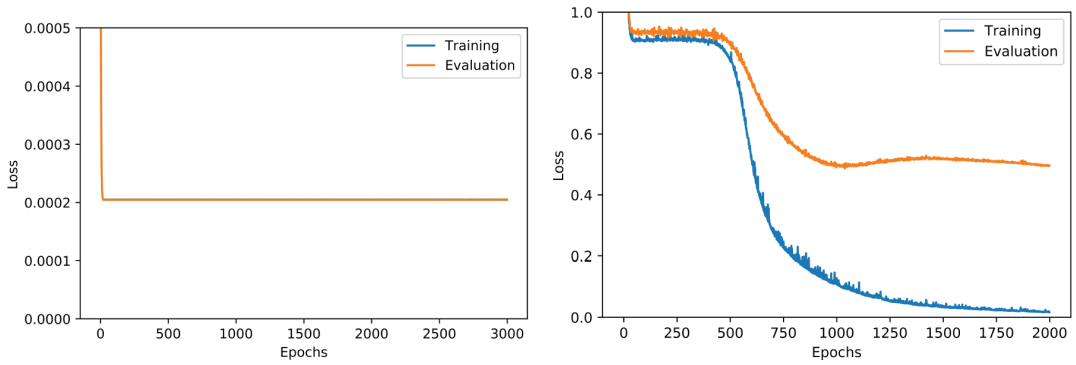

(a) (b)

Fig. 5.15 Underfitting (a) and overfitting (b).

much larger than the latter. The second reason is that the model is too complex with large parameters. The third reason is that the model has an ample hypothesis space, which means that the dataset is likely too simple for the model, and several parameter groups can fit the training dataset. Underfitting and overfitting always happen until one completes a practical model training and testing. Fig. 5.16 shows the relationship between the model capacity, which usually means the features that the model can represent, and these two situations [88].

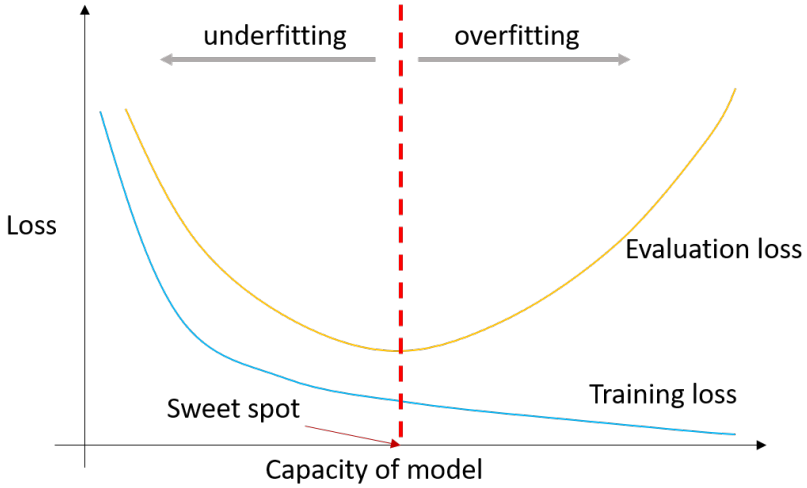

Fig. 5.16 Overfitting and Underfitting represented using model loss vs capacity.

Beamlet images classification network

A convolutional neural network is designed to classify the images with and without beamlet signal. This is a typical two categories classification question. In the model, the input data have one dimension with 494 values, the image intensity integration in horizontal direction. The first convolution layer has as output 32 features with a leaky rectified-linear-unit (ReLU) function. For the second convolution layer the output has 64 features. After this, a pooling layer and

a sigmoid function are used. The whole connection layer is at the end, and the log-softmax function scales the value from 0 to 1, as Eq. 5.43.

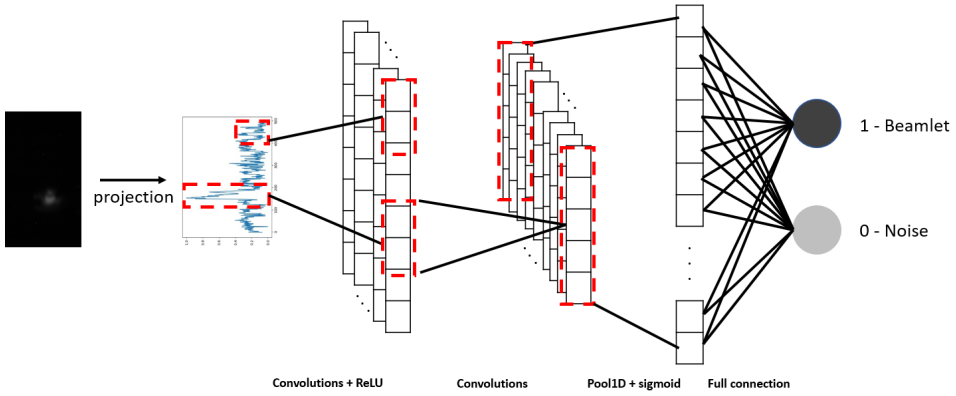

Fig. 5.17 Classification model.

$$LogSoftmax(x_i) = log(\frac{exp(x_i)}{\sum_j exp(x_j)}) \tag{5.43}$$

In this model, 2500 cases from experiments are used, thereof 2000 for training, and 500 for testing. The distribution of beamlet signal and noise images are the same and both 50%. It takes about half an hour for one hundred epochs of training and testing on the personal computer. Fig. 5.18 (a) shows the loss during the training and testing. The loss decreases fast into 20 epochs and becomes stable after 50 epochs. During the training, the accuracy increases relatively fast and slightly fluctuates, less than 0.1%. In the end, the accuracy is 98.8% which is enough for the experiments, shown as Fig. 5.18 (b).

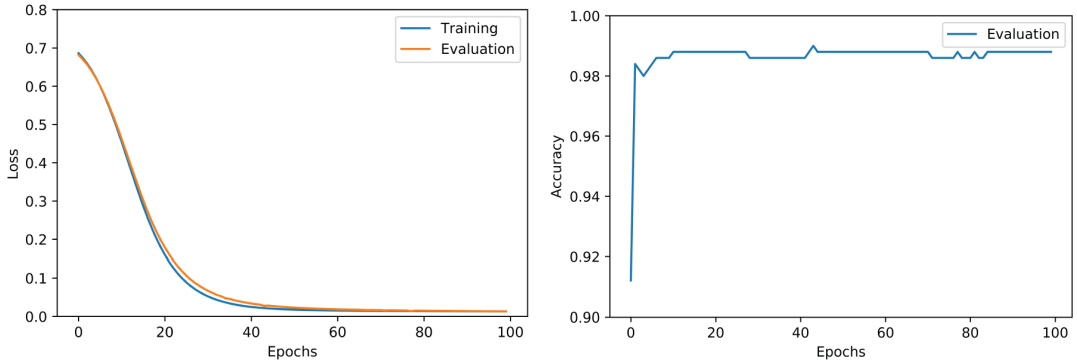

(a) (b)

Fig. 5.18 Classification loss (a) and classification accuracy (b).

Beamlet images machine learning filter network

The second task consists in the noise reduction of the beamlet images. The network in this part is an auto-encoder. Mark A. Kramer first created this network type in 1991 to analyze the complex data without restriction on the character of the nonlinearities present in the data [89]. The typical idea is to learn the features of the data with noise (encoder), then reconstruct the data from the features (decoder) as shown in Fig. 5.19. In recent years this network has been proven for reducing images noise in accelerator physics field [90]. The auto-encoder consists of

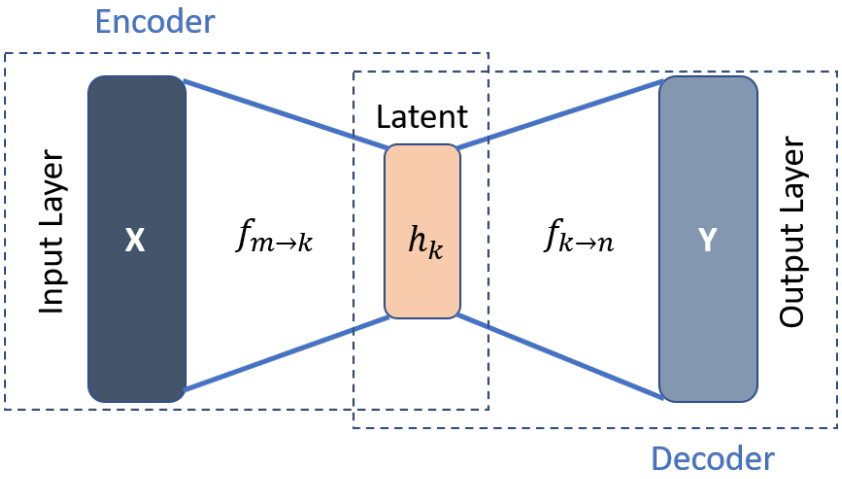

Fig. 5.19 Auto-encoder sketch.

two parts, the encoder, and the decoder. For the encoder, the input is the vector $x \in R^m$, and the output is the reconstructed vector $y \in R^n$. In the simplest case, one hidden layer exists that stores the vector in the latent space h_k. The network has to learn the functions $f_e : R^m \to R^k$ and $f_d : R^k \to R^n$. In principle, the features of the inputs will be learned and stored into the latent layer, and then the decoder layers will rebuild the signal as the output. The encoder layers and the decoder layers are symmetric in most situations.

In the auto-encoder network used for beamlet images, shown in Fig. 5.20, the input data have one dimension, which is the same as in the classified network. The output features of the convolution layers in the encoder part are 16 and 32 with stride 1. The upsample layers are both nearest, and scaling factors are 2. The latent layer has 1964 features. The output features of the convolution layers in the decoder part are 32 and 16 with stride 2. In the end, it applies a whole connecting layer.

The training data are from 1502 experimental beamlet images, processed using traditional filters and manually. Fig. 5.21 shows the programmed user interface used for experimental beamlet images. Noise signal data are taken from 107 experimental images with no beamlet signals. The noise signals are first normalized, some examples are shown as Fig. 5.22. Some noise images are similar to random, and some are not. The reason is the influence of the radiation surrounding the camera, and digital noise is changeable. We randomly combined the filtered beamlet and noise data, and constructed 167205 projection data records, in which 80 % were used for training and 20 % for testing. The cases used for training and testing are shown as Fig.

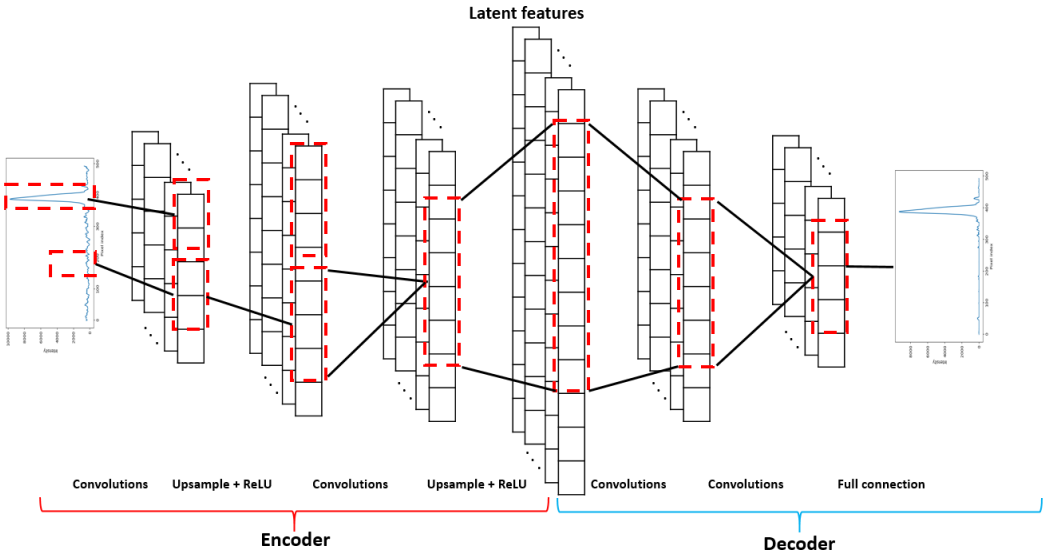

Fig. 5.20 Auto-encoder network structures.

5.23. The training procedure was performed in the Maxwell Computer Cluster at DESY, using

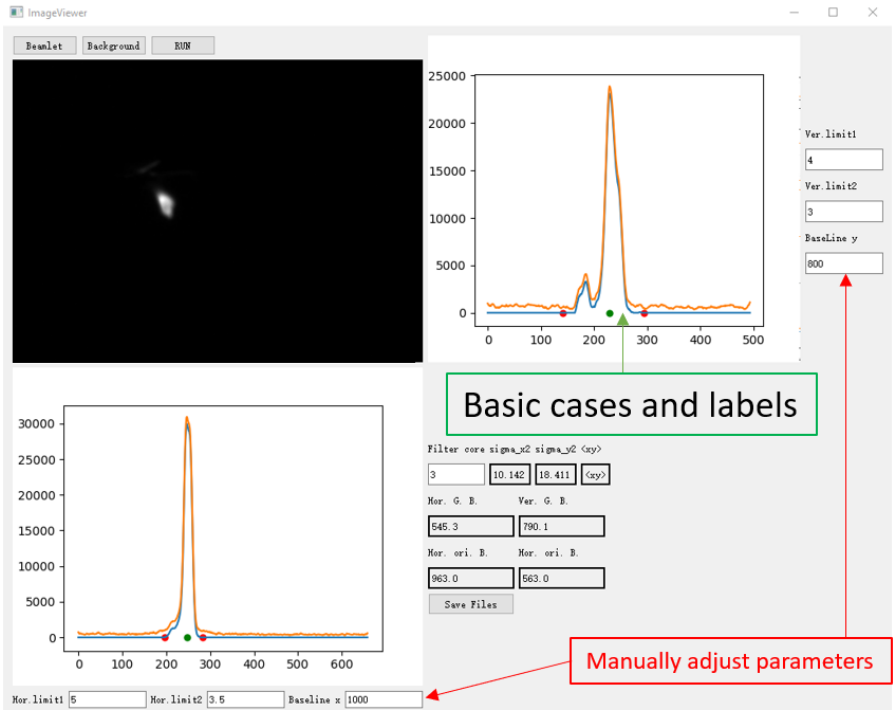

Fig. 5.21 Experimental beamlet images processing user interface.

NVIDA Tesla P100 GPU. The training time depends on the choices of the hyperparameters, such as the batch size, learning rate, and epoch size. Also, the effect and the stability of the network have a relationship with these hyperparameters. When the network's structure is defined, the next important work is to search for the best hyperparameters for the network,

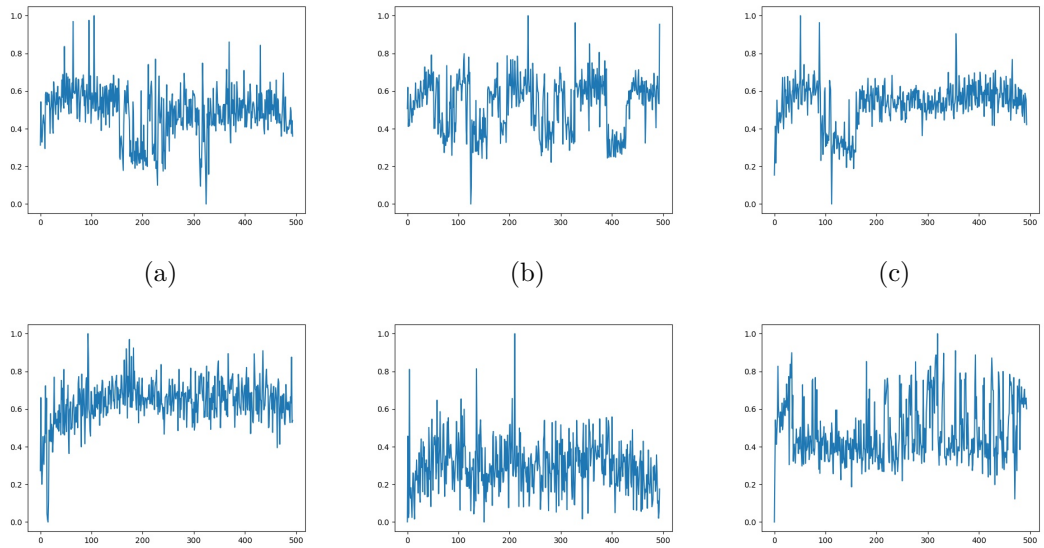

(a) (b) (c)

(d) (e) (f)

Fig. 5.22 Beamlet noise from experiments.

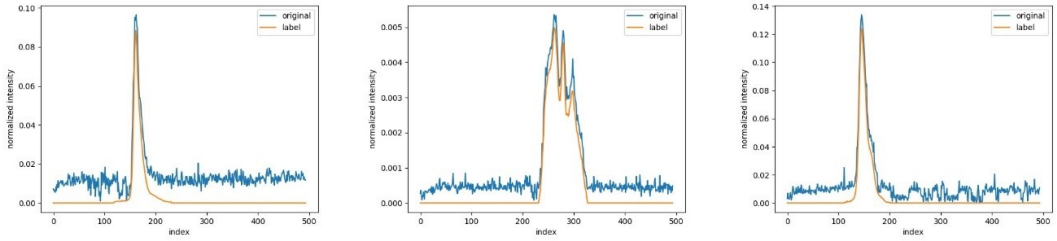

(a) (b) (c)

Fig. 5.23 Autoencoder dataset cases examples.

which means, in general, that the loss of the network becomes small and stable. Usually, one can find hints during training and testing on how to optimize these parameters. Even for the experienced researcher, it still needs several tries to find the best parameters for the network.

The optimizer used is Adam in Pytorch [91]. To find a better latent layer size, shown as Fig. 5.24 (a), one can find that the latent layers size of 122 and 1960 are worse than layer size of 490 and 982. The loss of the latent layer size of 122 converges slower and finally stabilizes at 6×10^{-8}. The loss of the latent layer size of 1960 is fluctuating and converges slowest, although it is close to the 122 latent layers in the end. For the latent size of 490 and 982, they have similar loss in the end, but the 982 latent layers size converges faster in the beginning. So the latent layers size is set as 982. The other important parameter in the network is the learning rate. Fig. 5.24 (b) shows three different learning rate with 982 latent layers. The loss decreases and converges faster with larger learning rate. But when the learning rate is more than 3×10^{-5}, this trend will become slow. The batch size is another important parameter. Generally, small batch size is noisy, and offer a regularizing effect and lower generalization error. Also, small batch size make it easier to fit one batch worth of training data in memory and small requirement to the memory size. However, this is not a rule and depends on the dataset features [92]. From Fig. 5.24 (c), one can find that during training, the network with smaller batch size converges slower than that with larger batch size. But when the batch size is larger than 3072, the loss becomes higher, and indicates the best batch size is 3072.

When the best hyperparameters are found, the network is ready to process the beamlet images from experiments. It costs about one and a half hours with one thousand epochs, 3072 batch size, and mean square error (MSE) loss function for training. The total number of parameters is 2 005 887 in the network.

This network is more efficient and faster than the traditional filters, as the comparison shows in Fig. 5.25. From the images, one can see that the traditional filters can only filter the common noise. They cannot reduce the tilt noise, and at the same time preserve the real signal. However, the auto-encoder filter can do both. Even the substructure of the beamlet signal can be well reconstruct. The disadvantage of the auto-encoder filter is that it is not a universal filter. It is suitable for the projected beamlet images only, i.e. for the one-dimensional signal in the vertical direction. One should rebuild the dataset for different images and train the network again.

5.3.4 Slit-scan simulation

To study the slit-scan method in detail and to check the data processing method, a series slit-scan simulations utilizing the computer code ASTRA are carried out. The basic approach is similar to the actual slit-scan experiments, and the steps are the followings:

- 1. Generate a beam distribution with given number of particles, beam energy, emittance, and Twiss parameters;
- 2. Cut beam into beamlets according to slit width and step width;
- 3. Drift space simulations (slit to screen) for all beamlets with particle input from cutting;
- 4.Record the particles position at the screen station;

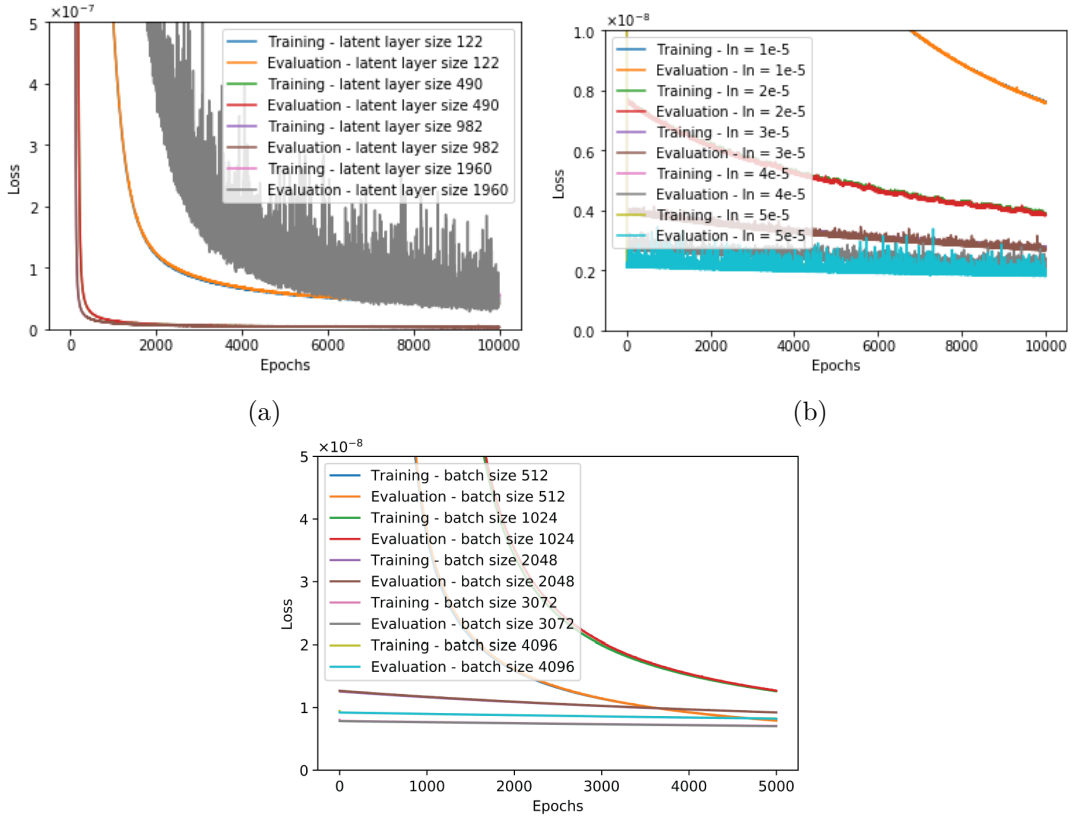

Fig. 5.24 Loss comparison of different latent layer size under learning rate 1×10^{-5} with 1024 batch size (a). Loss comparison of different learning rate under 982 latent layers with 1024 batch size (b). Loss comparison of different batch size under 982 latent layers with learning rate 1×10^{-5} (c).

- 5. Calculate and reconstruct the phase space of the whole beam at slit position from the beamlet data;
- 6. Compare reconstructed phase space and emittance results with the initial data.

In this simulation, the 3-D space charge calculation method of ASTRA is applied for the part from slit position to the screen. First, we talk about the particle number in the simulation. Considering the time of simulation, we decided to use the smallest particle number of 0.8 million which provides accurate results.

5.3.5 Error analysis of slit-scan

The error of slit-scan emittance measurement in our experiments has five contributions: the slit width error (e_0), the space charge error (e_1), slit position recording jitter (e_2), beamlet images center and RMS size uncertainty (e_3), and beam energy uncertainty (e_4). It is shown as the

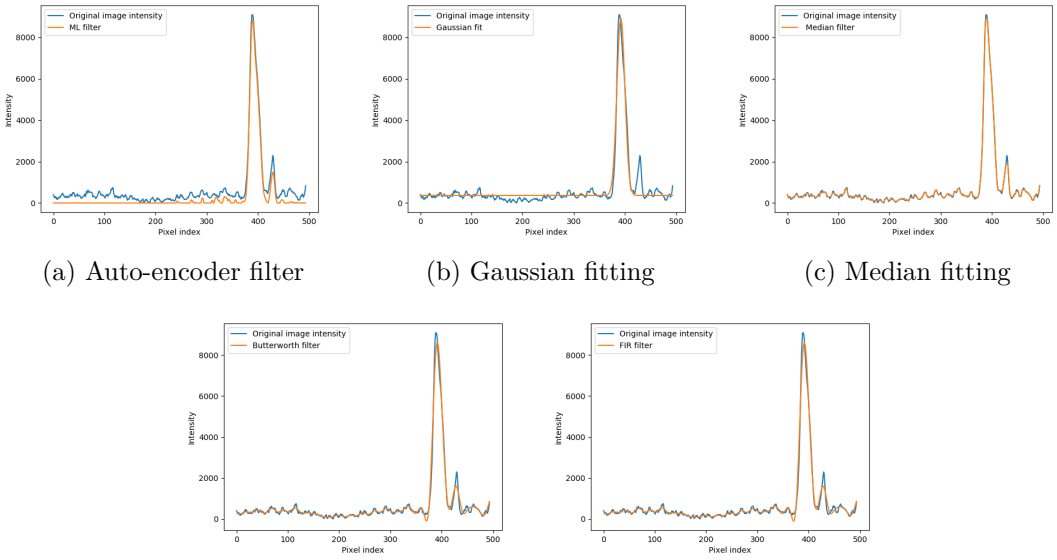

(a) Auto-encoder filter (b) Gaussian fitting (c) Median fitting

(d) Butterworth filter (e) FIR filter

Fig. 5.25 Different filters comparison.

equation:

$$e = \sqrt{e_0^2 + e_1^2 + e_2^2 + e_3^2 + e_4^2}. \tag{5.44}$$

5.3.6 Beam size correction factor

Using a YAG screen, the beam RMS size can also be measured directly at the slit position. Experimental results show that reconstructed beam sizes $< x^2 >$ from the measurement of the beamlets are smaller than the direct results. The reason is the finite signal-to-noise ratio which causes signal losses at the low-intensity edges of the beamlets. This effect has been identified for the first time at the PITZ photo injector [93, 94] and a correction factor f_c has been introduced:

$$f_c = \frac{\sigma_x}{\sqrt{x^2}}, \tag{5.45}$$

where σ_x is the beam RMS size measured at slit position, and $< x^2 >$ is the second central moment of the beam distribution from slit can measurement. Then the (corrected) normalized emittance can be written as:

$$\varepsilon_{n,rms} = \frac{\sigma_x}{\sqrt{\langle x^2 \rangle}} \frac{p_z}{m_0 c} \sqrt{\langle x^2 \rangle \langle x'^2 \rangle - \langle x x' \rangle^2}. \tag{5.46}$$

As proposed in Ref. [93, 94] this conservative approach of the slit-scan analysis has been used in this paper and belongs to the standard slit-scan procedure at the ELBE SRF Gun. Fig. 5.26 gives the correction factor changes with bunch charge. One can find that at low bunch charge, sometimes the factor is smaller than one due to dark current or the other noise not subtracted

from signal mixed into the signal completely. In most situations, it is between 1 and 1.1 for higher bunch charges.

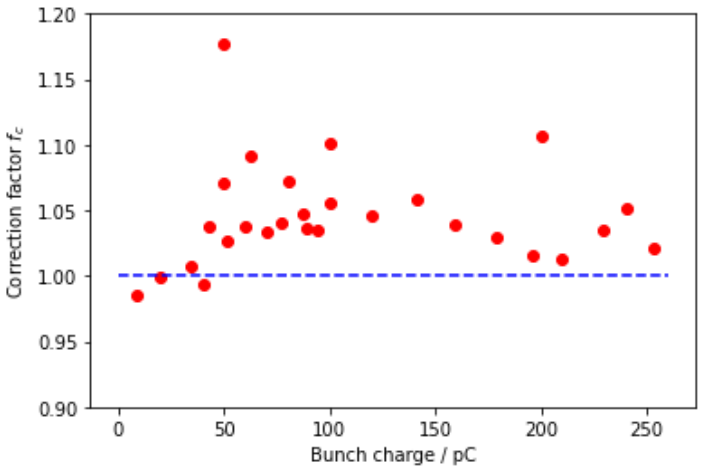

Fig. 5.26 Correction factor along with bunch charge. The blue dash line is equal one and the read dots are the correction factor calculated from slit scan experiment at different bunch charge.

Fig. 5.27 shows three beamlet images with complex spot distributions obtained from ASTRA simulation with parameters at slit position which are summarized in Tab. 5.1. The halos in these distributions may be below the experimental noise level, and thus the measured second central momenta could be smaller than the real ones.

5.3.7 Error due to the slit width

The influence of slit width is studied in simulation. From the slit-scan theory, the slit width does not limit the emittance measurement results. However, in experiments, the results for low bunch charges with low emittance are far from the simulation. One reason is the image noise, and the other reason is the limitation of the silt width and the pixel size of the screen, which will decrease the signal-to-noise ratio of beamlet images. In our beamline, the YAG screen pixel size is 25.3 μm. In the simulation, the pixel size is also fixed to 25.3 μm, and the silt width is

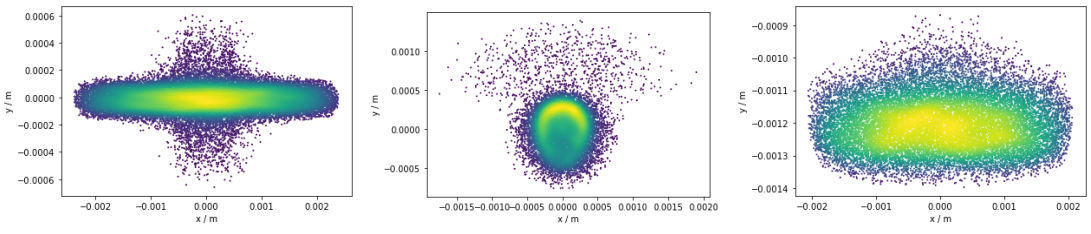

(a) (b) (c)

Fig. 5.27 Beamlet distribution with long tail in simulation.

Table 5.1 Slit-scan simulation beam parameters at slit position. In ASTRA simulation, the laser spot is Gaussian distribution with 1.064 mm RMS size and cutting at 1.17 time RMS size; gun maximum gradient is 20.5 MV/m with phase 55 degree and -5 kV DC voltage at cathode position; the integral solenoid field is 1.388 $\times$ 10^{-3} $T^2 \cdot m$ and located at 0.7 m downstream from the cathode; the slit is located at 2.76 m downstream from the cathode.

Beam energy (MeV)	4.452
Bunch charge (pC)	100
Horizontal RMS size (mm)	0.43
Vertical RMS size (mm)	0.43
Longitudianl RMS size (mm)	1.714
Transverse normalized emittance (mm·mrad)	1.655

changed at different beam normalized emittance. The results for the emittance error are shown in Fig. 5.28.

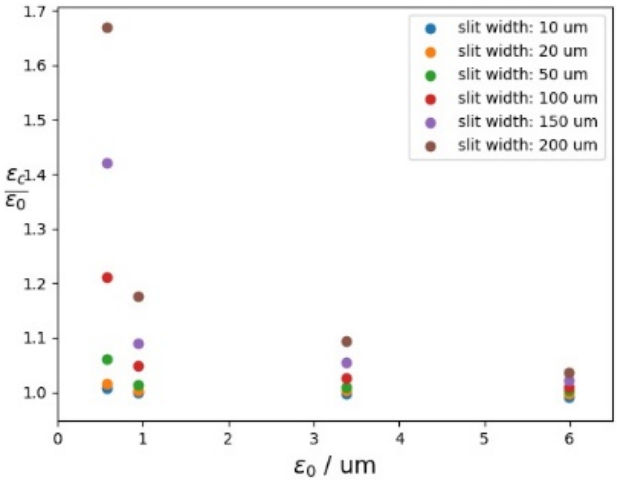

Fig. 5.28 Emittance error with different slit width at 0.75 meters drift distance.

Every slit with a certain width has an inherent error for different beam emittance. From fitting, it can be written as Eq. 5.47 approximately:

$$e_0 = \left| \frac{\varepsilon_c - \varepsilon_0}{\varepsilon_0} \right| \approx \frac{e^{-k\varepsilon_c}}{1 - e^{-k\varepsilon_c}} \tag{5.47}$$

here k is the parameter from fitting and shown in Tab. 5.2 and Fig. 5.29

5.3.8 Beamlet space charge effect

It is intuitive that once the space-charge dominated beam hit the slit and the major part is stopped, the remaining beamlet becomes an emittance dominated beam and gets rid of space

Table 5.2 The factors of different slit width.

Slit width (um)	k ($\text{mm} \cdot \text{mrad}^{-1}$)
10	10.93
20	9.10
50	4.85
100	2.12
150	1.19
200	0.76

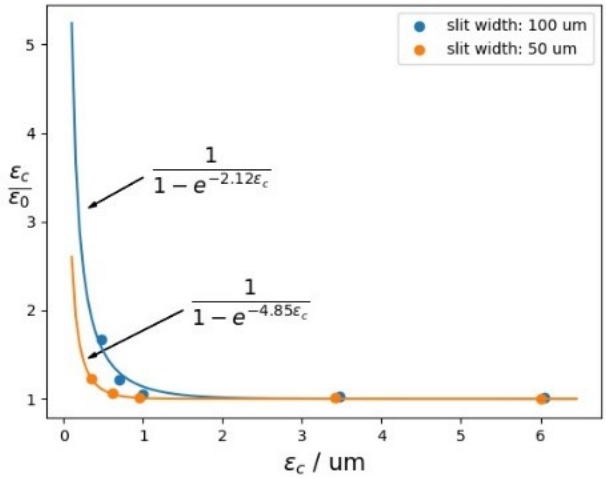

Fig. 5.29 The emittance ratio of calculation and simulation with calculation emittance.

charge. However, this conclusion is incorrect because the slit cut off most of the particles, but it does not change the particle density. The beamlets with high particle density potentially contribute further to an emittance error.

From Eq. 5.2, a typical value is $R_0 = 0.1$ for a beam with 200 pC and 2.1 mm RMS size at slit position at SRF gun beam line for 1.875 mm RMS size laser spot on the cathode. Assuming that the beam distribution is uniform at the slit position and the slit width is d, the beamlet space charge dominance ratio can be given by:

$$R_b = \sqrt{\frac{2}{3\pi}} \frac{I}{\gamma I_0} \left(\frac{d}{\varepsilon_n}\right)^2 \tag{5.48}$$

When $R_b << 1$, the beamlet is emittance-dominated, and the influence of space charge is negligible. However, from the experiments, sometimes it is impossible to realize this condition due to the reception of the screen limitation. To evaluate the exact magnitude of the error from space charge, a series slit-scan simulation considering the drift distance and space charge are carried out with ASTRA. In the simulation, the slit width is 100 μm, and the slit step is fixed to 100 μm, similar to the experiments. From simulation results, the space charge and the drift distance contribute to the emittance error.

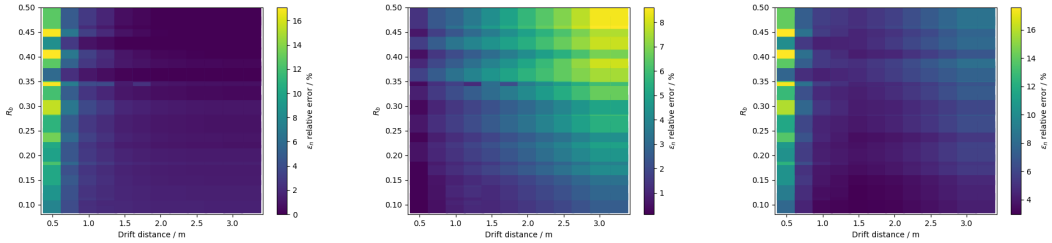

(a) (b) (c)

Fig. 5.30 Slit scan simulation: (a) without space charge, (b) only space charge, (c) with space charge.

Generally, when $R_b \leqslant 0.1$ and the drift distance is larger than 0.5 m, the error is less than 3% and will decrease with the drift distance enlarging, independent of space charge. When $R_b > 0.1$, the error from space charge enlarges with the drift distance increases, especially for large R_b, as Fig. 5.30 (b) shows. For a short drift distance smaller than 0.5 m, the error is more than 10% for the most cases.

However, R_b is related to beam parameters, such as bunch charge, beam spot size and bunch length. In the simulations, we have changed the laser power, laser spot size on the cathode, gun phase and solenoid current that all determine the aforementioned beam parameters. Fig. 5.31 shows how R_b evolves with bunch charge for laser spot radii on the cathode of 1.25 mm and 1.875 mm. The R_b for smaller laser spot radius on the cathode is larger than for the bigger radius for bunch charge less than 75 pC. In the high bunch charge case, larger than 100 pC, the smaller laser spot on the cathode has smaller R_b. When R_b is less than 0.5, the error is less than 10% as Fig. 5.30 (a) first column showns.

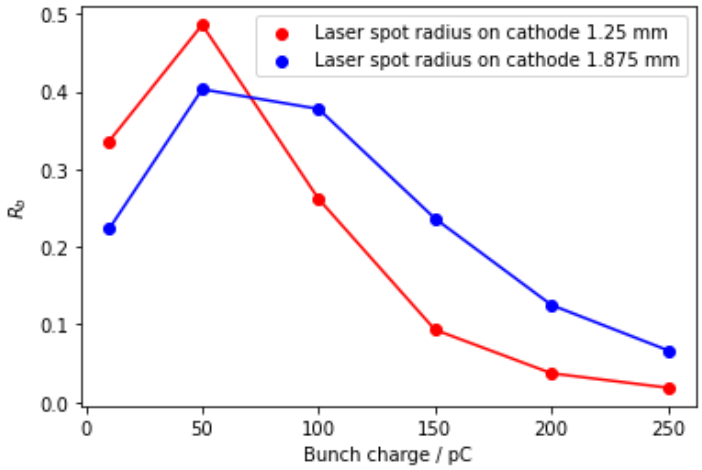

Fig. 5.31 along with the bunch charge at two different laser spot on the cathode.

5.3.9 Slit position recording uncertainty

The slit control system will be described in the next chapter in detail. Since the delay time of the whole system being is uncertain, the recorded values of slit position calculated in Eq. 6.8 have jitter. From the recording time and position, one can calculate the velocity of the motor in each step. If assume that the setting velocity of the slit is stable and constant, one can compare the velocity from the recording data with the setting values. Fig. 6.29 shows that during the slit-scan, the recording time or slit position has some uncertainties, which results in the slit step having about 0.2 % error for the setting velocity of 0.25 mm/s. To analyze the influence of slit position jitter on emittance, it assumes that the jitter is a random value from a uniform distribution, and the average of the jitter is Δx. Ignoring the high order terms, the error of emittance can be written as:

$$\begin{aligned} \varepsilon_{nc} &\cong \left(1 + \frac{\Delta x}{x}\right) \varepsilon_{n0} \\ e_2 &= \frac{\Delta x}{x}, \end{aligned} \tag{5.49}$$

here ε_{nc} and ε_{n0} are the calculated and original emittance. Fig. 5.32 shows that the error result from the position jitter is linear with the record step jitter. In our experiments, this error is less than 0.8% in average.

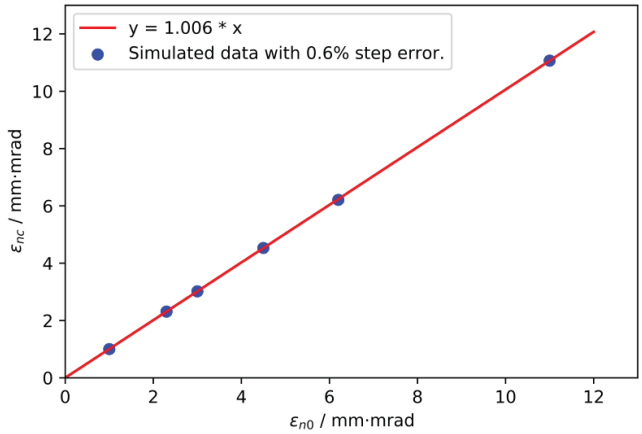

Fig. 5.32 The normalized emittance from calculation versus the normalized emittance from simulation at average 0.6% slit moving step error

5.3.10 Image noise

Although the ML filter can reduce noise efficiently, the remaining noise will influence the beamlet position and RMS size calculation. On the other hand, the signal-to-noise ratio is different and unknown in each beamlet image. In the experiments, one can make the slit scan two times, one time with the beam off for background measurement. However, this means it needs twice the time and still cannot subtract the noise one hundred percent. The influence of

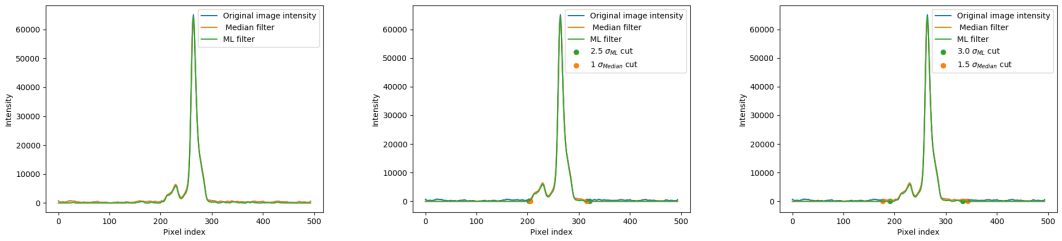

(a) (b) (c)

Fig. 5.33 One example with different cutting factors.

Table 5.3 Beamlets center, RMS and intensity details of Fig.5.33.

ML filter			Median filter		
Limit f	Center (pixel)	RMS (pixel)	Limit f	Center (pixel)	RMS (pixel)
0	262.80	23.64	0	260.58	55.07
2.5	262.40	15.36	1	262.29	16.15
3.0	262.50	15.71	1.5	262.31	19.29

dark current on beam emittance will be discussed later in this section. To reduce the influence of the noise on the beamlet center and RMS size calculations, these calculations are performed twice. The first calculation uses the pixel intensities of the whole measurement range. In the second time, the pixel intensities are used in a certain range of the beamlet RMS size times a factor f far from the center calculated first. Usually, f is chosen between 0.5 to 5 depending on different image conditions. Fig.5.33 and Tab. 5.3 show one example calculated with different f factors, which indicates that the beam RMS size is more sensitive than the center position to the value of f.

For the emittance calculation, the uncertainty is from the beamlet image intensity, the beamlet center, and beamlet RMS size. Let δ_n, δ_c, and δ_σ be the averaged relative uncertainties of the beamlet intensity, the beamlet center position, and the square of the RMS size. Assuming that they are independent of the beamlet number i, then the i-th beamlet center and RMS size can be written as:

$$\begin{aligned} n_{i,r} &= (1 \pm \delta_n)\, n_i \\ \bar{x}_{sci,r} &= (1 \pm \delta_c)\, \bar{x}_{sci} \\ \sigma^2_{i,r} &= (1 \pm \delta_\sigma)\, \sigma^2_i. \end{aligned} \tag{5.50}$$

Then the beamlet deviation is:

$$x'_{i,r} = \frac{1}{L}\left(\bar{x}_{sci,r} - x_{si}\right) = \frac{1}{L}\left(\bar{x}_{sci} - x_{si}\right) \pm \frac{\delta_c}{L}\bar{x}_{sci}, \tag{5.51}$$

beam center deviation is:

$$< x' >_r = \sum n_i x'_{i,r} =< x' > \pm \frac{\delta_c}{L} \sum n_i \bar{x}_{sci} =< x' > \pm \frac{\delta_c}{L} < \bar{x}_{sc} >, \tag{5.52}$$

the error of $< x'^2 >$ from δ_c:

$$\begin{aligned} < x'^2 >_r &= \sum n_i \sigma_i'^2 + \sum n_i \left(x'_{i,r} - < x' >_r \right)^2 \\ &= \sum n_i \sigma_i'^2 + \sum n_i \left[\frac{1}{L} \left(\bar{x}_{sci} - x_{si} \right) \pm \frac{\delta_c}{L} \bar{x}_{sci} - < x' > \pm \frac{\delta_c}{L} < \bar{x}_{sc} > \right]^2, \\ &= < x'^2 > \pm 2 \frac{\delta_C}{L} \sum n_i \left(x'_i - < x' > \right) \left(\bar{x}_{sci} - < \bar{x}_{sc} > \right) \end{aligned} \tag{5.53}$$

the error of $< x'^2 >$ from δ_σ:

$$< x'^2 >_r = < x'^2 > \pm \frac{\delta_\sigma}{L^2} < \sigma^2 >, \tag{5.54}$$

the error of $< x'^2 >$ from δ_n:

$$\begin{aligned} \left\langle x'^2 \right\rangle_r &= \sum n_{i,n} \sigma_i'^2 + \sum n_{i,n} \left(x'_i - < x' >_r \right)^2 \\ &= \sum n_{i,n} \sigma_i'^2 \pm \delta_n \sum n_i \sigma_i'^2 + \sum \left(1 \pm \delta_n \right) n_i \left(x'_i - < x' >_r \right)^2 \\ &= < x'^2 > \pm \delta_n < x'^2 >, \end{aligned} \tag{5.55}$$

the error of $< xx' >$ from δ_c:

$$\begin{aligned} < xx' >_r &= \sum n_i x_{si} x'_{i,r} \\ &= \sum n_i x_{si} \left[\frac{1}{L} \left(\bar{x}_{sci,r} - x_{si} \right) \pm \frac{\delta_c}{L} \bar{x}_{sci,r} \right] \\ &= < xx' > \pm \frac{\delta_c}{L} \sum n_i x_{si} \bar{x}_{sci}, \end{aligned} \tag{5.56}$$

the error of $< xx' >$ from δ_n:

$$\begin{aligned} < xx' >_r &= \sum \left(1 \pm \delta_n \right) n_i x_{si} x'_{i,r} \\ < xx' >_r &= < xx' > \pm \delta_n < xx' >, \end{aligned} \tag{5.57}$$

the error of $< x^2 >$ from δ_n:

$$< x^2 >_r = < x^2 > \pm \delta_n < x^2 > . \tag{5.58}$$

The final equation for the error of squared geometrical emittance $\delta(\varepsilon^2)$ is:

$$\Delta \left(\varepsilon^2 \right) = \frac{2\delta_c}{L} \left| \left\langle x^2 \right\rangle \left\langle x' \bar{x}_{sc} \right\rangle - \left\langle xx' \right\rangle \left\langle x_s \bar{x}_{sc} \right\rangle \right| + \delta_\sigma \left\langle x^2 \right\rangle \left\langle \sigma'^2 \right\rangle + 2\delta_n \varepsilon^2. \tag{5.59}$$

To obtain the relative error of ε:

$$\Delta\varepsilon = \frac{\partial \varepsilon}{\partial \left(\varepsilon^2 \right)} \Delta \left(\varepsilon^2 \right) = \left(\frac{\partial \varepsilon^2}{\partial \varepsilon} \right)^{-1} \Delta \left(\varepsilon^2 \right) = \frac{1}{2\varepsilon} \Delta \left(\varepsilon^2 \right) \tag{5.60}$$

$$e_3 = \frac{\Delta\varepsilon}{\varepsilon} = \frac{\delta_c}{\varepsilon^2 L} \left| \left\langle x^2 \right\rangle \left\langle x' \bar{x}_{sc} \right\rangle - \left\langle xx' \right\rangle \left\langle x_s \bar{x}_{sc} \right\rangle \right| + \frac{\delta_\sigma}{2\varepsilon^2} \left\langle x^2 \right\rangle \left\langle \sigma'^2 \right\rangle + \delta_n. \tag{5.61}$$

Introducing:

$$\begin{aligned} \frac{\langle x^2\rangle \langle x'\bar{x}_{Sc}\rangle - \langle xx'\rangle \langle x_S\bar{x}_{SC}\rangle}{L} &= k_C\varepsilon_0^2 \\ \left\langle \sigma'^2 \right\rangle \left\langle x^2 \right\rangle &= k_\sigma\varepsilon_0^2, \end{aligned} \tag{5.62}$$

finally, the emittance error caused by the beamlet measurement uncertainties is:

$$e_3 = \left| \delta_c k_c + \delta_n + \frac{\delta_\sigma k_\sigma}{2} \right|. \tag{5.63}$$

k_c and k_σ depend on the distribution of the beam in phase space and the relationship of the coordinate systems at slit position and screen position. It is difficult to calculate them because they all include the real measurement values. However, one can estimate them if it is assumed that their magnitudes are similar as the actual emittance value and the factors k_c and k_σ are equal to one. So the error from the beamlet intensity, center and RMS size jitter is linear with the jitter magnitude as $|\delta_n + \delta_c + \frac{\delta_\sigma}{2}|$.

5.3.11 Energy uncertainty

Energy jitter will contribute to the error of the normalized emittance by the relativity factors β and γ. This error can be written as:

$$e_4 = \frac{\delta\varepsilon_n(E)}{\varepsilon_n} = \frac{1}{\beta^2}\frac{\delta(E)}{E} \tag{5.64}$$

5.4 Extremely low bunch charge and cathode thermal emittance measurement

5.4.1 Theory

The emittance measurement at extremely low bunch charge is essential in many cases for a successful operation of the photo injector. This includes to measure the thermal emittance of the photocathode, and on the other hand it is needed for low bunch charge applications, such as Ultrafast Electron Diffraction (UED). There are three methods suitable for this measurement: solenoid scan, single shot thermal emittance mapping, and grid scan. Here we focus on the first two methods only.

The solenoid scan and the quadrupole scan are similar in the implementation and the data analysis. However, one potential failure consists in the fact that the horizontal and the vertical directions of the beam can be correlated. Then the beam spot remains not round during the measurement and an enlarged emittiance can be measured. P. W. Huang and H. Qian at PITZ have introduced a new thermal emittance measurement method, called single shot thermal emittance mapping [95]. The idea of this method bases on linear beam transport theory. Fig. 5.34 shows a simplified model of the beamline components which are involved, the gun cavity, a solenoid, and a screen. In the analysis of this model, the cavity is simply treated as a diverging lens and the solenoid as thin focusing lens, and they are represented by the corresponding

matrices in linear transport theory. The simple estimation is given in the following:

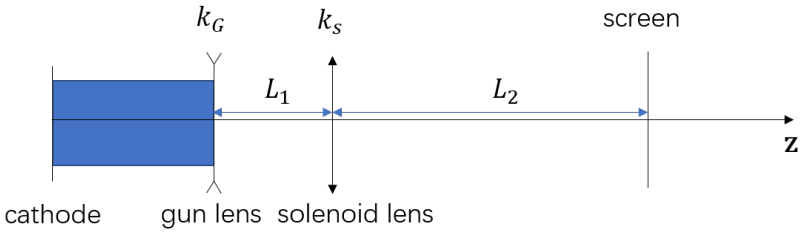

Fig. 5.34 Single shot thermal emittance mapping illustration.

$$\begin{pmatrix} x \\ \frac{p_x}{m_0 c} \end{pmatrix} = M \begin{pmatrix} x_0 \\ \frac{p_{x0}}{m_0 c} \end{pmatrix} = \begin{pmatrix} M_{11} & M_{12} \\ M_{21} & M_{22} \end{pmatrix} \begin{pmatrix} x_0 \\ \frac{p_{x0}}{m_0 c} \end{pmatrix} \tag{5.65}$$

$$M = \begin{pmatrix} 1 & L_2 \\ 0 & 1 \end{pmatrix} \begin{pmatrix} 1 & 0 \\ -k_s & 1 \end{pmatrix} \begin{pmatrix} 1 & L_1 \\ 0 & 1 \end{pmatrix} \begin{pmatrix} 1 & 0 \\ k_G & 1 \end{pmatrix} \tag{5.66}$$

Then

$$M_{11} = 1 + k_G L - (1 + k_G L_1) L_2 k_s \tag{5.67}$$

$$M_{12} = L - L_1 L_2 k_s. \tag{5.68}$$

here $L = L_1 + L_2$. For the cavity, for instant the SRF gun cavity, the focal strength is estimated as [42]:

$$k_G = \frac{dx'}{dx} = \frac{eE_0}{2cp_{nz}} \sin(\varphi). \tag{5.69}$$

The solenoid focal strength is calculated from Eq. 4.1. The beam position and RMS size square can be written as:

$$x = \mathrm{M}_{11} x_0 + \mathrm{M}_{12} x_0', \tag{5.70}$$

$$\left\langle x^2 \right\rangle = M_{11}^2 \left\langle x_0^2 \right\rangle + M_{12}^2 \left\langle (x_0')^2 \right\rangle \tag{5.71}$$

with x_0' is defined as $p_{x0}/(m_0 c)$. If we set M_{11} equal zero, then the solenoid focal strength must be

$$k_s = \frac{1 + k_G L}{(1 + k_G L_1) L_2}. \tag{5.72}$$

For the given value of L_1 and L_2, the solenoid magnetic field must be 0.2477 T, and the corresponding current amounts about 5.5 A, which is inside the setting range. M_{12} amounts

$$M_{12} = \frac{L_2}{1 + k_G L_1} \frac{m_0 c}{p_z} \tag{5.73}$$

At the photocathode, the transverse position and transverse momentum of the photoemission electrons are not correlated and the thermal emittance can be expressed by

$$\frac{\varepsilon_{nc}}{\sigma_{x0}} = \frac{p_{x0}}{m_0 c} = \frac{\sigma_x(L)}{M_{12}} \tag{5.74}$$

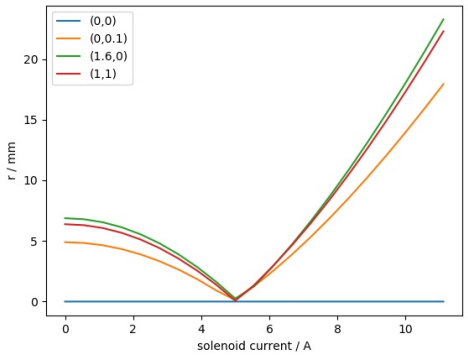

(a) 50 fC, With space charge

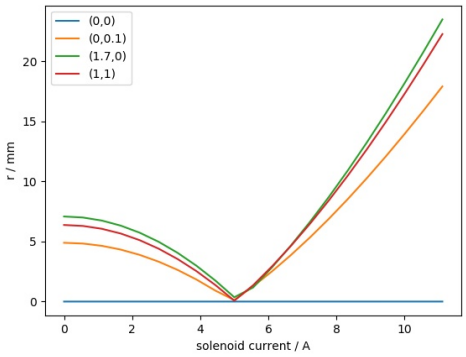

(b) 50 fC, Without space charge

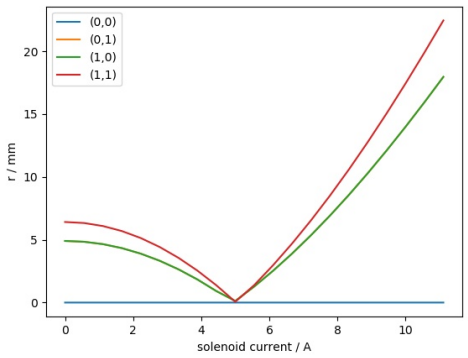

(c) 100 fC, With space charge

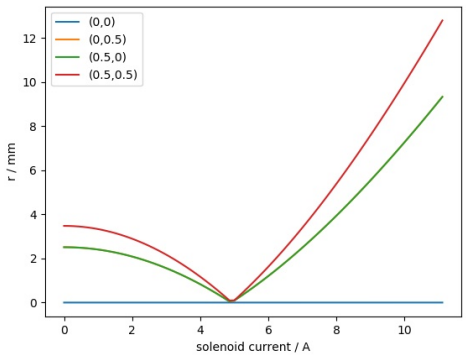

(d) 100 fC, Without space charge

Fig. 5.35 Solenoid working current with and without space charge in simulation. In this simulation, the SRF Gun gradient is 8 MV/m with phase 50 degrees. The distance from solenoid to the screen is 2.061 m. The curves are for different starting positions on the cathode (x, y) with values in mm.

where σ_{x0} is the RMS photoemission spot size on the cathode and $\sigma_x(L)$ the RMS beam spot size on the screen.

5.4.2 Single shot transverse momentum imaging simulation

Electron bunches with 50 fC and 100 fC charge with and a RMS length 2.3 ps are used in the simulation. The distance from the cathode to the screens amounts 2.76 m for the screen in screen station 2. In the method the precondition for exact results is that the matrix element M_{11} is zero. This means that the beam position on the screen remains constant independent of the initial beam position on the cathode. To proof that and to find the exact setting value of the solenoid for this condition, the inital beam is given different offset values at the cathode and the solenoid current is varied. The offset values in the simulation are less than 2 mm because the cathode diameter is 4 mm in the experiment. At the edge of the cathode, field nonlinearities appear, but their effect is not severe. As we can see in Fig.5.35, the solenoid working current is equal for all beam position offset on the cathode. Using screen station 2 in

the beamline, the solenoid current is around 5 A in the simulation. The space charge effect can be ignored if the bunch charge is 50 fC or 100 fC or similar small, which is also proofed in the simulation presented in Fig. 5.35.

Once the gun parameters are set, the solenoid working current can be obtained from simulation and later from the experiment by the same method. Then M_{12} can be taken from the simulation. Fig. 5.36 shows the determination of the M_{12} value. From the linear fitting, M_{12} is 0.21296 ± 0.00006 mm^2/(mm $\cdot$ mrad).

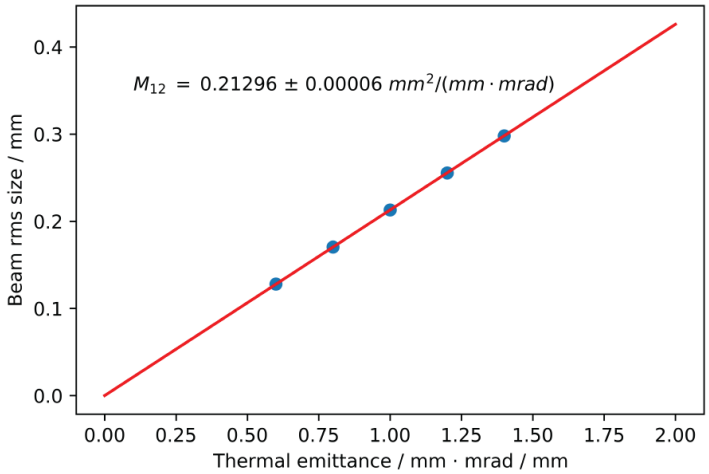

Fig. 5.36 Single-shot mapping M_{12}. In this simulation, the SRF Gun gradient is 8 MV/m with phase 50 degrees. The distance from solenoid to the screen is 2.061 m and the solenoid working current is 4.85 A.

Chapter 6

Experiment results

6.1 SC solenoid magnetic field

6.1.1 Solenoid design and motivation

As it is discussed in Chapter 4.1.2, the spherical aberration coefficient of a solenoid grows with the square of the first derivative of the axial magnetic field. The additional emittance due to the spherical aberration increases linearly with this coefficient. In order to reduce this effect, we optimized the iron yoke geometry and broadened the longitudinal field distribution of the solenoid, especially we decreased the gradient of the longitudinal edge field. This new solenoid is intended for SRF gun III. As in the previous SRF gun, the motivation for the use of a SC solenoid is not to obtain a high field, but a shortest possible distance to the SC cavity. Thus, the solenoid is placed inside the gun cryomodule which requires a compact design and extremely low thermal losses from the solenoid coil electric current. Since SRF gun III is planed to deliver beams with lower emittance at higher bunch charges, it also needs a reduction of the spherical aberration.

The coil body of the SC solenoid was built by Niowave Inc. The NbTi SC wire used for the winding of the coil is a multifilament wire with Cu matrix and a 4.5:1 ratio of Cu to NbTi. The critical temperature for superconductivity of the NbTi amounts 9.7 K. The coil has 2110 windings and the total length of the wire used is approximately 640 m. The magnet yoke is made of soft iron, the other parts consists of Cu, Al, and nonmagnetic stainless steel. In Fig. 6.1 the solenoid design is presented. The iron yoke surrounds the SC coil and has a lengths of 120 mm, an outer diameter of 124 mm, and a boring diameter of 63.5 mm. A ring-shaped Cu plate with inserted, u-shaped, stainless steel tube for liquid He is attached to the coil body and serves for cooling. In the cryomodule the He tube is connected to the 2 K helium cooling system of the RF cavity.

6.1.2 Cryomodule

For tests and the magnetic field measurement, the SC solenoid has been installed in the cryomodule intended for SRF gun III. Fig. 6.2 shows a section of the cryomodule's CAD design

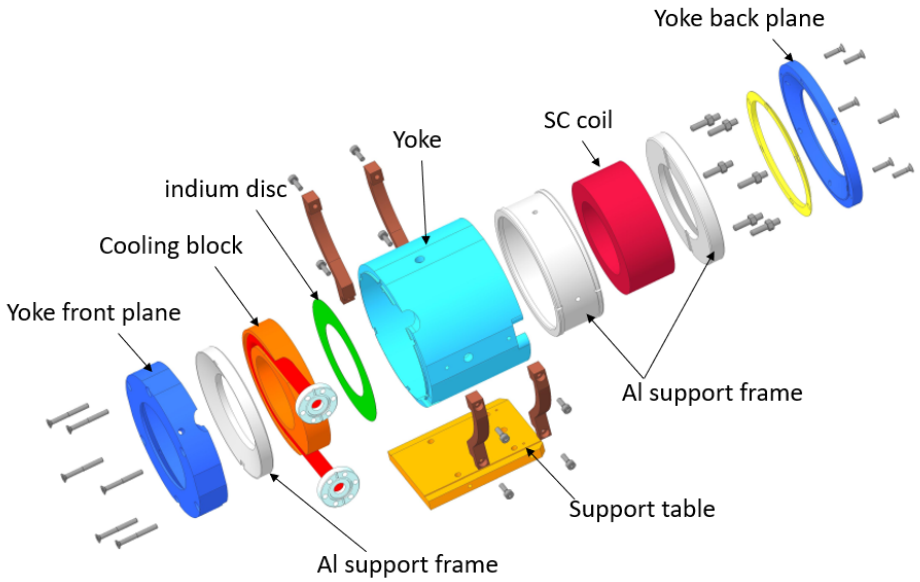

Fig. 6.1 Exploded CAD drawing of the SC solenoid.

with the SC solenoid, the beam tube, the cavity end group, and the He vessel housing the RF cavity. A successful operation of the gun requires an exact alignment of the solenoid with respect to the RF cavity axis, which concerns the two transverse coordinates x, y and the corresponding two tilt angles. For its transverse movement the solenoid is mounted on the platform of two combined translation stages driven by stepper motors. The adjustment of the horizontal and vertical tilts can be done manually by appropriate screws.

The solenoid alignment procedure should be done in two main steps [96]. The first step is performed during the gun cryomodule assembly. It has the purpose to adjust the two tilt angles, i.e. to make sure that the axis of the solenoid is parallel to the cavity axis. The second step is carried out after commissioning of the gun. It is a beam based alignment and required the remote controlled horizontal and vertical motion of the solenoid. The spacing between solenoid boring and beam tube allows a movement up to 6 mm in horizontal and vertical directions.

Whereas the SC solenoid with all related components and diagnostics were built in as it is shown in Fig. 6.3, that was not the case for the RF cavity and the beam pipe. Instead a vacuum-tight tube, closed at the inner end was assembled, which extends into the cryomodule by about 300 mm and allows access from outside for the field probes (see Fig. 6.5).

After finishing the installation work, the cryomodule was sealed and vacuum pumped. Since it was connected to the liquid He and liquid N_2 cooling system of the ELBE facility and the computerized control and monitoring system was in operation, the cryomodule was automatically cooled down and was permanently hold in the operational state. At the solenoid temperatures between 4.5 K and 5 K were measured up to the current target value of 8 A, i.e. the temperature was always safely below the critical value of 9.7 K. In order to transfer away the ohmic heat from the stepper motors, they are cooled by liquid N_2.

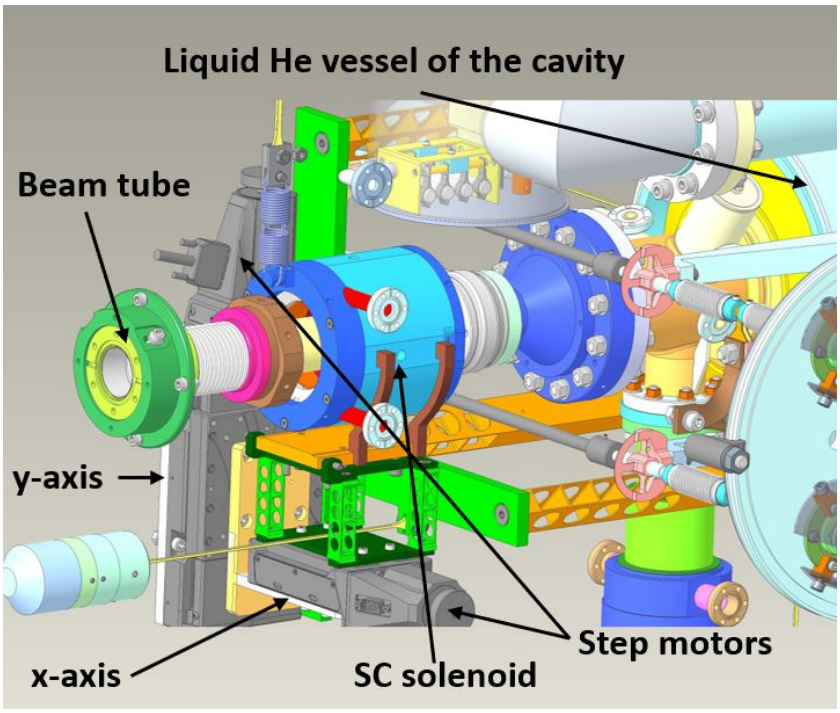

Fig. 6.2 CAD image of the SC solenoid installation in the SRF gun III cryomodule.

6.1.3 Measurement setup

A photograph of the magnetic field measurement system is shown in Fig. 6.4. For the 3-D coordinate measuring of components and mechanical alignment a Quantum Max metrology tool (mechanical measuring arm) of FARO company was used. Before closing the cryomodule, the mechanical axis and position of the solenoid were determined by means of this measuring tool. As a reference plane the large flange for the front-side lid (see Fig. 6.4) of the cryomodule was chosen. The three-axis movement of the measuring probes for the magnetic field mapping was realized by a combination of three motorized linear stages (OWIS GmbH). The stage for the z-axis motion had a travel range of 270 mm, and thus the magnet probes were mounted in such a position that the maximum of the the longitudinal field was located at about z = 135 mm. For the determination of the transverse coordinate origin and the longitudinal axis adjustment again the FARO mechanical measuring arm was employed. In the transverse plane at the starting position z = 0 mm, the transverse center point was found to be (15.28 mm, 65.50 mm). Moving the z-axis stepper motor the full range of motion of 270 mm, the measurement axis had deviations of -0.296 mrad in the horizontal -0.407 mrad in vertical direction for the first time, and had -0.667 mrad in the horizontal and 0.889 mrad in the vertical direction for the second time.

The two magnetic field sensors are based on the Hall effect. The first one is a 1-D axial Hall probe from Magnet-Physik GmbH applied to measure the longitudinal field component, as shown in Fig. 6.7 (a). Its measurement range is from 3 mT to 3 T and the active area has 0.4 mm diameter. The second one is a 3-D Hall probe from SENIS AG with a range of ± 200 mT and a resolution of 0.001 mT for the three field components. The active probe size is 150 μm x

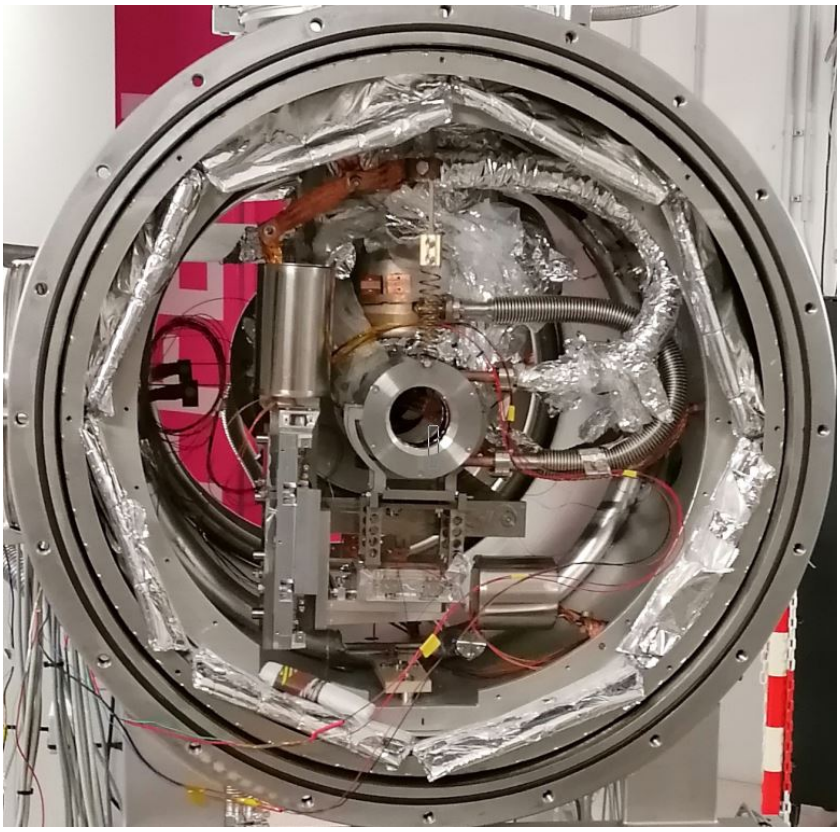

Fig. 6.3 SC solenoid installation in cryomodule.

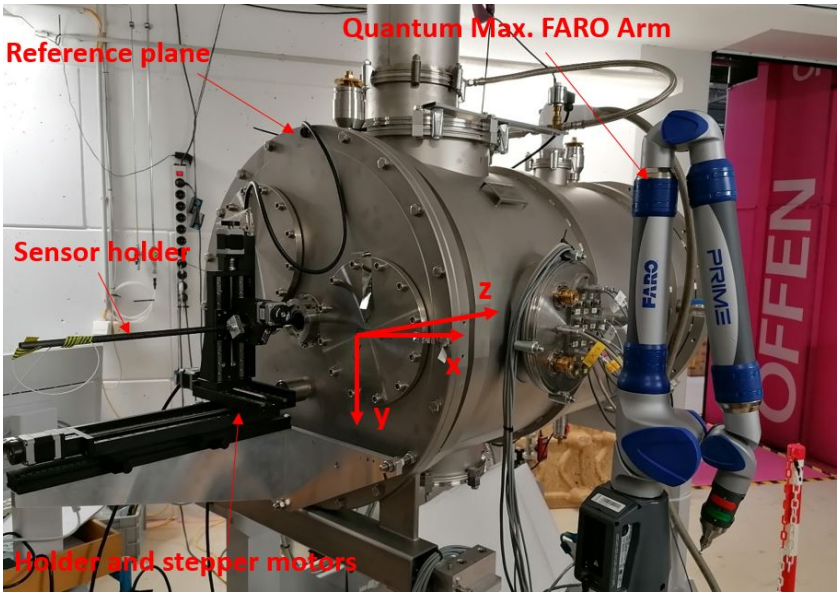

Fig. 6.4 Superconducting solenoid measurement system.

150 μm and 50 μm in thickness. A holder was built to ensure the probe is without tilt and to cover the probe for protection during the mapping, shown in Fig. 6.7 (b). For the measurement

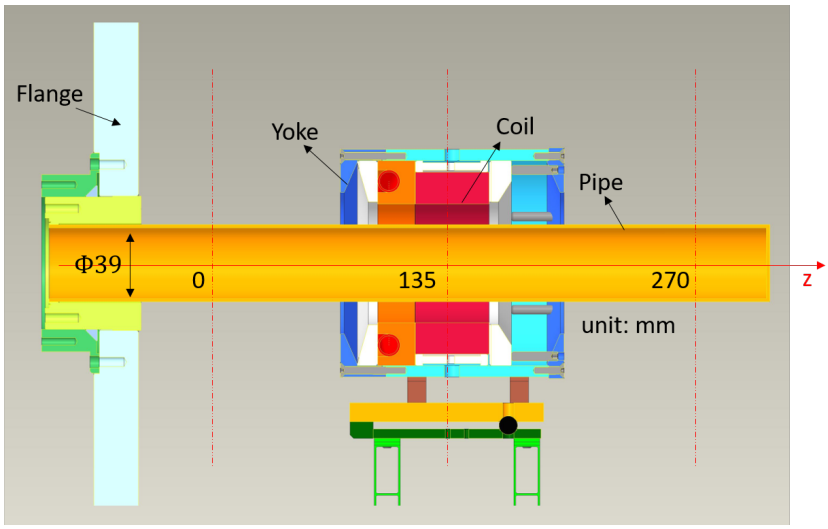

Fig. 6.5 CAD image of field measurement setup with SC solenoid, tube, and coordinate system.

of the longitudinal magnetic component with 1-D probe the range was 0 to 270 mm with a 5 mm step size and it was carried out along the mechanical solenoid axis. The mapping with the 3-D probes was performed in an area of 12 mm × 11 mm in horizontal and vertical directions, as shown in Fig. 6.6. The center point of each plane was (15.28 mm, 65.5 mm). The step sizes were 1 mm in the transverse plane and 5 mm in the longitudinal direction. It takes about 4.5 minutes to measure one plane, and the total time for one complete mapping was about five and a half our. Due to the range limit of the 3-D probe, the maximum current for mapping was 5 A. The longitudinal field component was determined with currents from 1 A to 8 A.

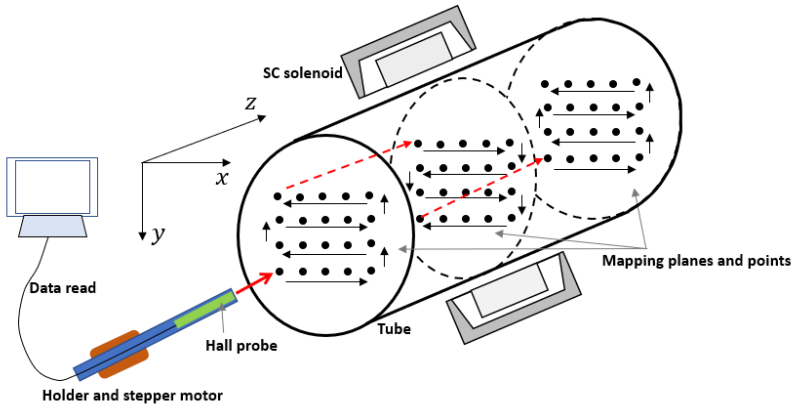

Fig. 6.6 Illustration of the SC solenoid field mapping.

6.1.4 Longitudinal field results

The longitudinal field B_z on axis was measured with the 1-D Hall probe because of easier data processing. The longitudinal field is much stronger than the transverse field. Thus the comparably low effect arising from the mismatch between measurement axis and solenoid axis

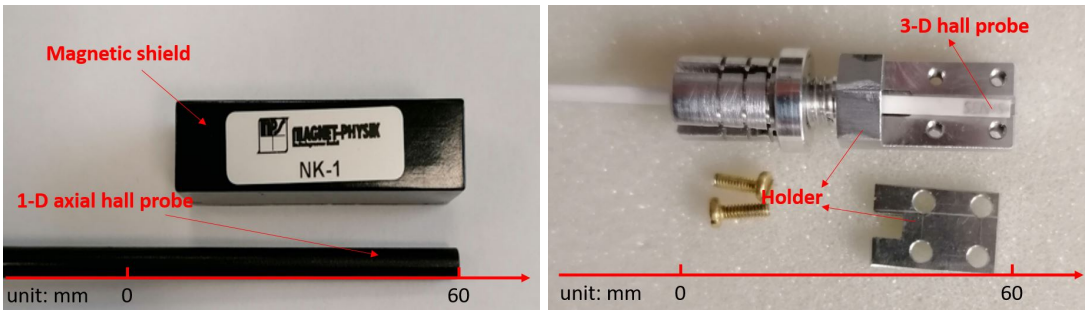

(a) (b)

Fig. 6.7 (a) 1-D hall probe; (b) 3-D hall probe and holder.

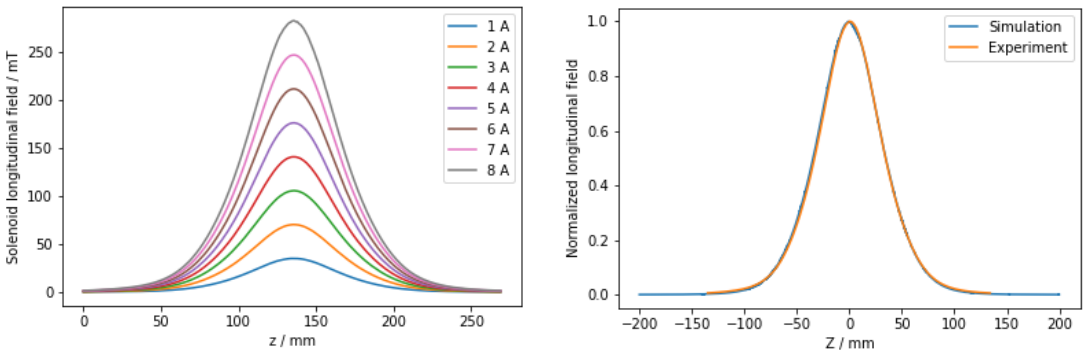

(a) (b)

Fig. 6.8 SC solenoid longitudinal field.

is ignored. Fig. 6.8 (a) shows the longitudinal field profile of B_z for currents from 1 A to 8 A. The comparison with computed profile, presented in Fig. 6.8 (b), shows a very good agreement. As expected, the field maximum of B_z grows linearly with the solenoid current, and the slope coefficient is 35.232 mT/mm, shown in Fig. 6.9 (a). The effective length is measured to 50.990 mm $\pm$ 0.068 mm (defined in Eq. 4.2), and Fig. 6.9 (b) shows the results obtained for different currents.

6.1.5 Misalignment measurement

In order to determine the magnetic field of the SC solenoid a mapping of the spatial field distribution was performed as it is illustrated in Fig. 6.6. For this measurement the 3-D Hall probe was applied and, given by the range limit, the maximum current for the mapping was 5 A. As it was proven to be advantageous in the simulation, the longitudinal field component B_z was used in the analysis. To avoid any influence of the background field, the first mapping was carried out at 0 A current, and these data were subtracted from the regular measurement data before numerical treatment. The data analysis was performed as described in section 4.2.2. For each plane the coordinates of the extremum (maximum outside and minimum inside the solenoid) were determined by a parabolic fitting. Then linear regressions are performed

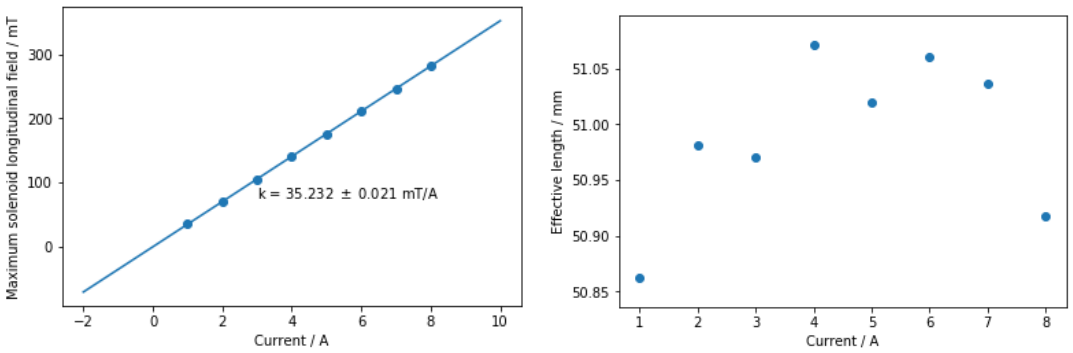

(a) (b)

Fig. 6.9 SC solenoid maximum longitudinal field vs current (a) and effective length vs current (b).

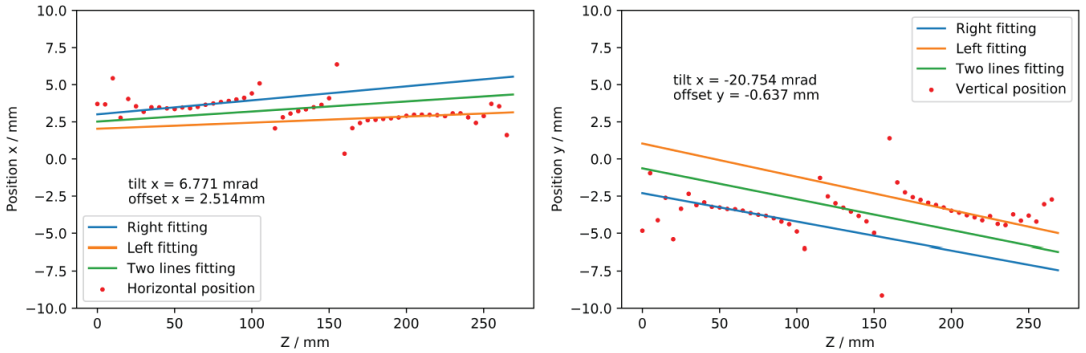

(a) (b)

Fig. 6.10 SC solenoid longitudinal field axis fitting with current 4 A. Horizontal axis fitting (a) and Vertical axis fitting (b).

in selected z ranges at the entrance and exit of the solenoid with these series of center point coordinates which deliver two straight lines. The final values for the SC solenoid field axis tilt and offset are the averaged values of these two straight line values. Fig. 6.10 shows a group of measurement results at 4 A solenoid current together with the linear fitting to determine the solenoid axis parameter (a, b) and the axis center coordinates for all the measured planes from z = 0 mm to z =270 mm. A summary of the misalignment measurement results is presented in Tab. 6.1.

The offset position of the solenoid can be corrected by moving the x-y stage during operation of the SRF gun. However, the axis tilt can not be corrected afterwards. The misalignment between magnetic field axis and measurement axis can originate from a difference between the solenoid's magnetic and mechanical axes, the adjustment error of the solenoid with respect to the reference plane, the error of the measuring coordinate system with respect to the reference plane, and the inaccuracy in the data analysis. Further sources of possible impact are the magnetic hysteresis of the solenoid and surrounding components or a solenoid position change due to thermal contraction during the cool-down to 4.5 K.

Table 6.1 SC solenoid field axis measurement results.

Current / A	tilt x / mrad	tilt y / mrad	offset x / mm	offset y / mm
1	8.593	-19.043	0.062	-2.161
2	6.268	-24.781	0.489	-0.65
3	27.405	-23.357	0.042	-0.825
4	6.771	-20.754	2.514	-0.637
5	5.297	-19.178	2.878	-0.569
-3	6.884	-21.51	2.56	-0.5
-4	7.693	-23.209	2.132	-0.545
-5	9.001	-24.512	2.117	-0.499
Average	9.739 ± 7.239	-22.043 ± 2.262	1.599 ± 1.193	-0.798 ± 0.561

6.1.6 Multipole components

The multipole field analysis is based on the transverse field components which are measured with the 3-D Hall probe. Before the evaluation procedure was applied to the measured field data, again the measured background field was subtracted from the field mapping data. The specific aim of the data analysis was to determine the coefficients for the multipole field components according to Eq. 4.39 for each measurement plane. The center coordinates needed, were taken from the previous axis measurements.

Finally, a fitting procedure, performed for each plane, delivers the coefficients. The example presented in Fig. 6.11 belongs to the solenoid field at 5 A and the diagrams show the results as function of the longitudinal coordinate z. Fig. 6.11 (a) compares the solenoid transverse field coefficient J_t of the present measurement with the curve obtained from the first derivative of the meausred axis field B_z (see Eq. 4.22). The very good agreement confirms the correctness of the method.

Fig. 6.11 (b) shows the normal and the skew components of the parasitic dipole field. The normal dipole component is symmetric with the center of the solenoid, but the skew dipole is not. The entire dipole field can be written as given in the following equation:

$$\mathbf{B}_d = \mathbf{B}_{dn} + \mathbf{B}_{ds} = -J_{ds}\mathbf{e_x} + J_{dn}\mathbf{e_y} \tag{6.1}$$

The values obtained by integration along the z axis determine the strength and direction of the dipole kick which the beam suffers. Fig. 6.12 (a) presents the same results in the form of magnitude and phase. As can be seen, a phase change happens at the center plane position. The integrated dipole field increases linearly with the solenoid current, as shown in Fig. 6.12 (b).

The parasitic quadrupole part, presented in Fig. 6.11 (c), is antisymmetric with respect to the middle plane in the stronger normal component. The integrated gradient, calculated by z-integration of the presented curves, is thus nearly zero. However, taking into consideration the Larmor rotation of the beam coordinate frame inside the solenoid, an effect could still appear, as it has been discussed in Chapter 4. To evaluate the entire quadrupole field, we combine the normal and skew part as written in the following:

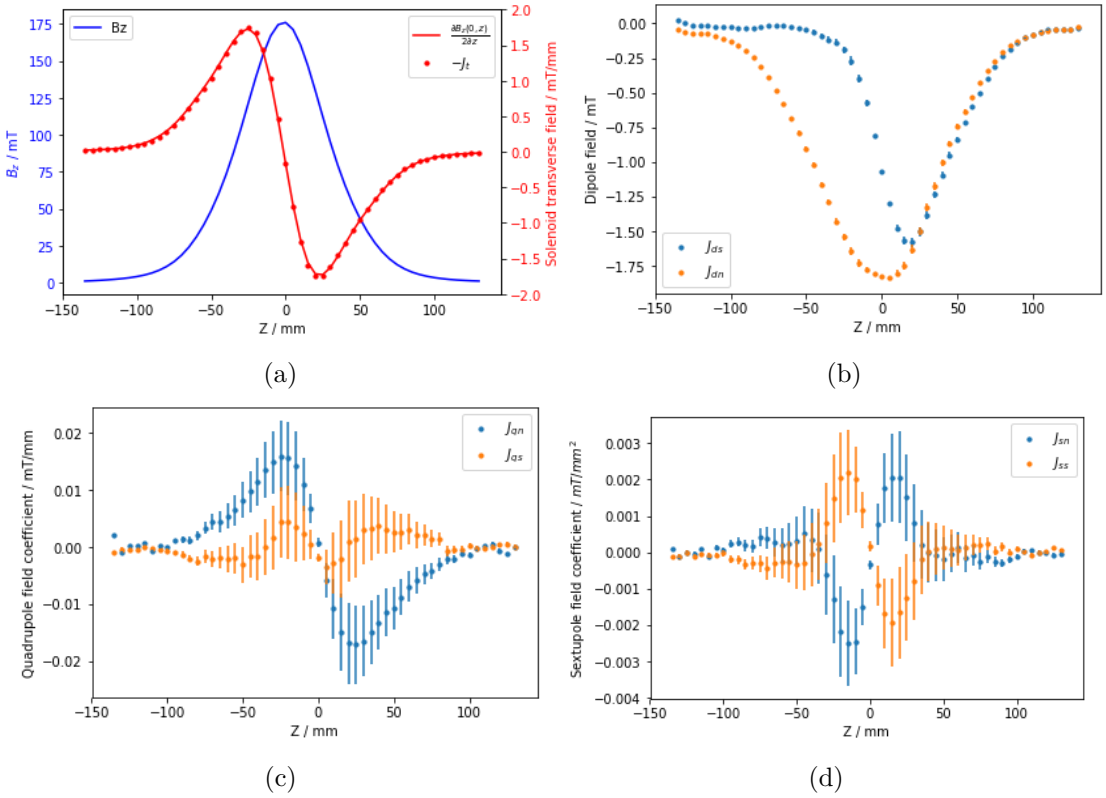

Fig. 6.11 SC solenoid transverse field multipole coefficients. (a) Solenoid transverse field vs z; (b) Normal and skew dipole components vs z; (c) Normal and skew quadrupole components vs z; (d) Normal and skew sextupole components vs z.

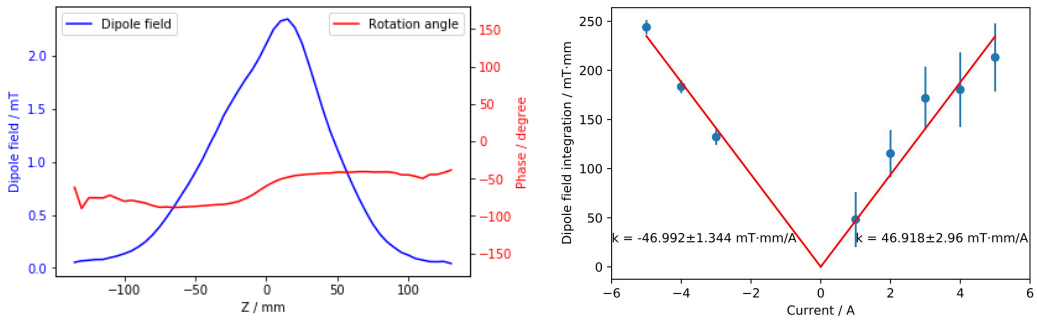

(a) (b)

Fig. 6.12 (a) Dipole component and phase vs z at solenoid current 5 A; (b) Dipole component integration vs current.

$$\mathbf{B}_q = \mathbf{B}_{qn} + \mathbf{B}_{qs} = (J_{qn}y - J_{qs}x)\mathbf{e_x} + (J_{qn}x + J_{qs}y)\mathbf{e_y} \tag{6.2}$$

The polar representation with magnitude and phase is shown in Fig. 6.13 (a), and Fig. 6.13 (b) depicts the integrated gradient in dependence on the solenoid current. The slopes for positive and negative currents of the lines in Fig. 6.13 (b) are different, which is likely caused by the measurement errors.

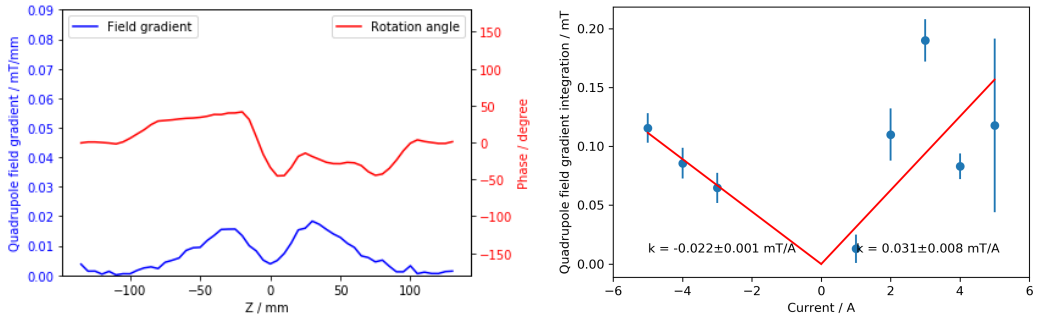

(a) (b)

Fig. 6.13 Quadrupole gradient and phase vs z at solenoid current 5 A (a); Quadrupole gradient integration vs current (b).

To cancel the influence from the parasitic quadrupole field, a group of correctors, consisting of one normal quadrupole and one skew quadrupole, is installed downstream from the center of the solenoid at 0.437 m distance in the SRF gun beamline. The corrector's effective length is 0.0672 m with a gradient of 0.012 T/m/A. The power supply has a maximum current of 3 A, and the setting range is now ± 2 A. Considering SRF gun III will be operated at a gradient of 12 MV/m, the SC solenoid current will be set up to 6 A for focusing the beam and compensate the transverse emittance. This means that the integrated quadrupole field gradient is as high as 0.186 mT with a peak gradient of 0.048 T/m and an effective length of 0.004 m. However, the quadrupole field phase is uncertain. Using these data, simulations were made with ASTRA. Fig.

6.14 shows the beam transverse emittance oscillation versus the quadrupole field rotation angle obtained in the standard x and y directions. The parasitic quadrupole field even can decrease the original emittance because it will correct the spherical aberration of the solenoid somehow when in the correct phase. However, it will increase the beam transverse emittance in most cases, and it is better to cancel this field. We assume the worst case, i.e. a quadrupole field phase of 45.8 degrees, as can be seen in Fig. 6.14, and the corrector is set to 0.5 A. Fig. 6.15 shows the beam transverse emittance oscillation as function of the corrector field phase. From the simulation results, the correctors can cancel the influence from the parasitic quadrupole field of the solenoid.

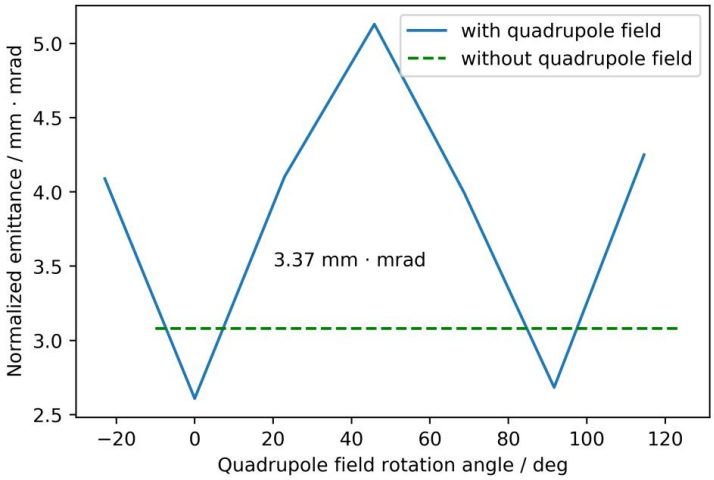

Fig. 6.14 Quadrupole field rotation angle vs normalized emittance obtained from ASTRA simulation for a uniform laser distribution of 2.5 mm on the cathode. The bunch change is 500 pC. The space charge is ignored when considering the quadrupole field of the solenoid. The beam kinetic energy is 6 MeV. The solenoid current is 6 A, the quadrupole component focal strength is 2.21 m^{-2} with an effective length of 0.004 m. They location is 0.55 m far from the cathode.

The sextupole field coefficient is smaller than the quadrupole field coefficient. The measurement accuracy of the sextupole field coefficient is lower than that of the dipole and quadrupole fields. The sextupole field can be written as

$$\mathbf{B}_s = \mathbf{B}_{sn} + \mathbf{B}_{ss} = [J_{sn}xy - \frac{1}{2}J_{ss}(x^2 - y^2)]\mathbf{e_x} + [\frac{1}{2}J_{sn}(x^2 - y^2) + J_{ss}xy]\mathbf{e_y}. \tag{6.3}$$

Fig. 6.16 (a) shows the sextupole field coefficient and phase along the longitudinal direction at 5 A of the solenoid. The amplitude of the sextupole field is nearly symmetric with respect to the center of the solenoid. The maximum values, around 0.0025 mT/mm^2, appear at the mirror planes. Also the phase changes strongly its sign at the center position and reaches the maximum and minimum values at the mirror planes. At the edges of the solenoid, the phase is not stable because the sextupole coefficient is too small for accurate fitting, and the noise dominates. It is intuitive that the z integral of the sextupole field coefficient is linear with the solenoid current. However, the results from the measurements are not, as shown Fig. 6.16 (b). The reason may come from the fact that the sextupole component is beyond the accuracy of

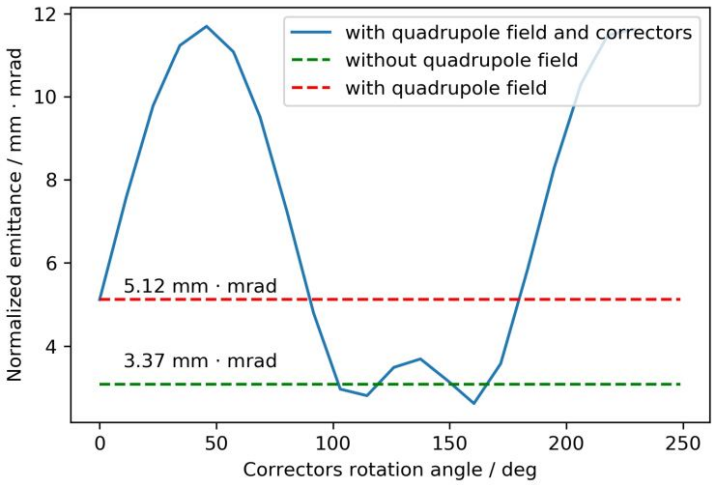

Fig. 6.15 Correctors rotation angle vs normalized emittance.

this measurement method. Therefore in Tab. 6.2, an estimation of the sextupole field strength is given based on the measurement results.

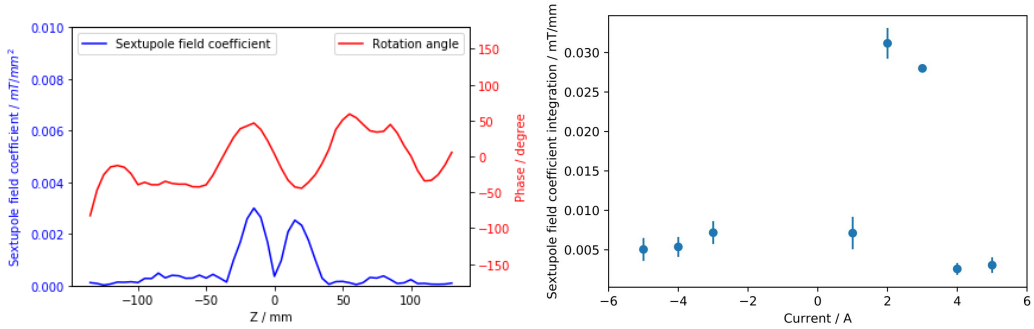

(a) (b)

Fig. 6.16 Sextupole field coefficient and phase vs z for a solenoid current of 5 A (a); Integrated sextupole field coefficient vs current (b).

Now we evaluate the sextupole field influence on the transverse emittance. From simulation for SRF gun III at 500 pC bunch charge, the beam RMS size at the solenoid is around 4 mm. The solenoid current will be set as 6 A, and the sextupole field amplitude is about 0.005 mT/mm^2 with an effective length of 0.006 m. If the beam has a Gaussian distribution, the additional normalized emittance is about 0.9 mm · mrad, and 0.52 mm · mrad in the case of an uniform distribution. Thus, the influence is about 20 %.

An overview of all the parameters of the solenoid are shown in table 6.2. The measured values of the main parameters satisfy the design requirements.

Table 6.2 Summary of SC solenoid field values, misalignment and multipole field measurement results.

Parameters	Simulation	Measured
B_z @ 8 A [mT]	286	282 ± 0.705
$\frac{dB_z}{dI}$ [mT/A]	35.7	35.232 ± 0.021
Effective Length [mm]	52.27	50.990 ± 0.068
Holder axis tilt x [mrad]	0	-0.667
Holder axis tilt y [mrad]	0	0.889
Field axis tilt x [mrad]	-	9.739 ± 7.239
Field axis tilt y [mrad]	-	-22.043 ± 2.262
Field axis offset x [mm]	-	1.599 ± 1.193
Field axis offset y [mm]	-	-0.798 ± 0.561
Max. integrated quadrupole field @ 5A	-	0.118 ± 0.060 mT
Max. integrated sextupole field @5 A	-	∼ 0.03 mT/mm

6.1.7 Magnetic field measurement error sources

The measurement uncertainties of the SC solenoid arise from four contributions: 1. not perfect Hall probe mechanical alignment; 2. not perfect degaussing of the yoke; 3. the Hall probe intrinsic error; 4. fitting error.

The field measurement was carried out within one week. Every complete field mapping needed about four and one half hours. Due to a technical deficiency of the measurement system (z movement range limit and initialization procedure) the Hall probe had to be realigned manually by means of a marker every day. This has resulted in a longitudinal position error of the Hall probe error below 0.8 mm, and a rotation error below 60 mrad. The solenoid longitudinal field error from this realignment error is less than 2 %. The transverse field uncertainty from the rotation error is less than 6 %.

The second error source is the incomplete degaussing of the yoke. The material of the yoke is a kind of soft iron (Fe 1.1003). Although the background field is recorded, it was not measured before every field mapping. The background field was recorded three times: before the whole measurement period, the second was before the solenoid current was increased to 4 and later 5 A, the third time was after the solenoid field was measured at -3 A. As shown in Fig. 6.17, the variation of the background field at the mechanical axis is about 0.125 mT. The background field was subtracted before multipole field analysis but due to its variations there are still uncertainties. The averaged differences of the multipole component integrals, for instance, for the dipole fields, quadrupole field gradients and sextupole field coefficients, are 18.4 %, 30.4 %, and 21.4 %, respectively.

The active area of the 1-D Hall probe possesses a diameter of 0.4 mm. The magnetic field value is an average of a circle area with 0.126 mm^2. The calibration of the 1-D Hall probe has 0.25 % uncertainty [97]. The core size of the 3-D Hall probe is $0.15 \times 0.1 \times 0.15$ mm^3. Total measuring precision is better than ± 0.1 % for the 3-D Hall probe [98]. The alignment of the inside sensor areas in the 3-D Hall probe has an intrinsic error less than about 17.45 mrad, shown as Fig. 6.18 [98].

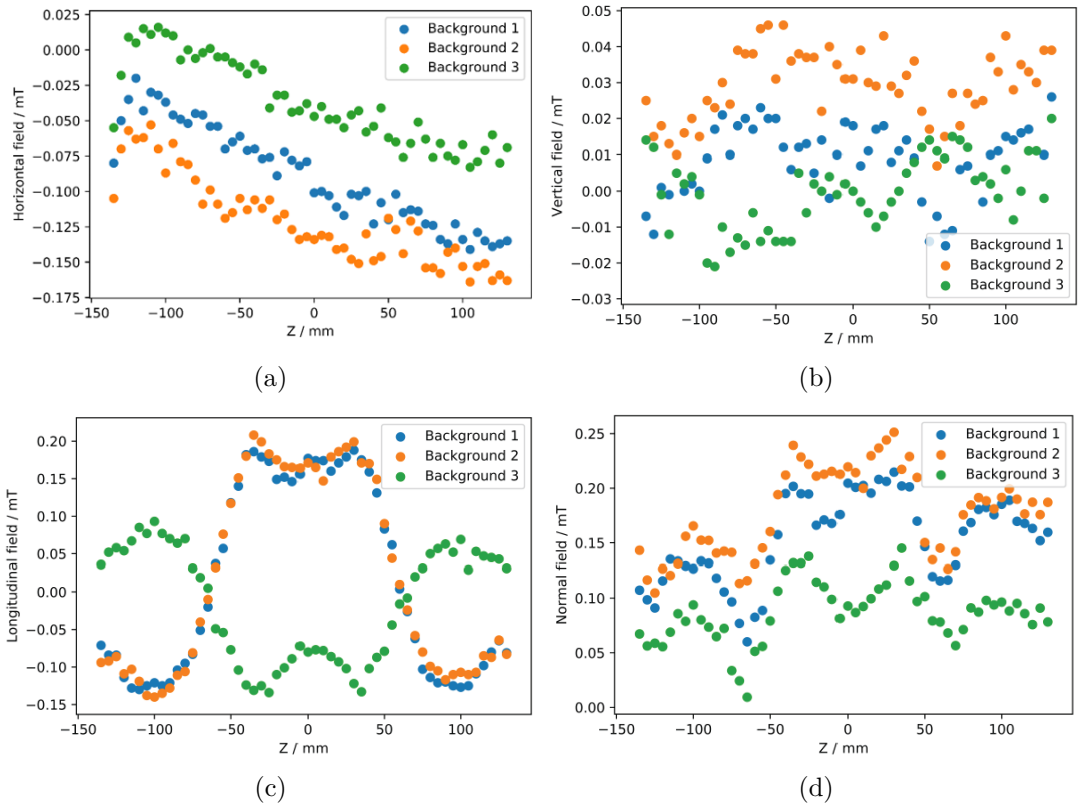

Fig. 6.17 Background field measurement results.

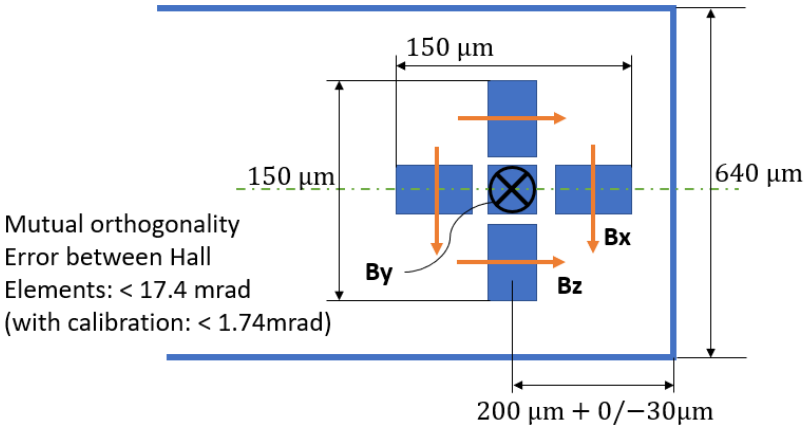

Fig. 6.18 3-D probe inside alignment.

From Fig. 6.11, the fitting errors are mainly in the quadrupole gradient and sextupole field coefficient. Comparing the average fitting error less than 1 % in simulation because of the finite grids size in computation, the fitting errors are 2 %, 73 % and 90 % for dipole field, quadrupole field gradient and sextupole field coefficients. The fitting error is a overall representation of the former three errors.

6.2 Quadrupole scan emittance measurements

Fig. 6.19 shows an overview of the diagnostic beamline and the ELBE beamline relevant for the presented measurements. There are three quadrupoles and two screens which are suitable for the quadrupole scan. Thus their combination allows measurements with six different drift lengths at otherwise nearly constant beam properties. The corresponding drift distances of each couple of quadrupole and screen are presented in Tab.6.5.

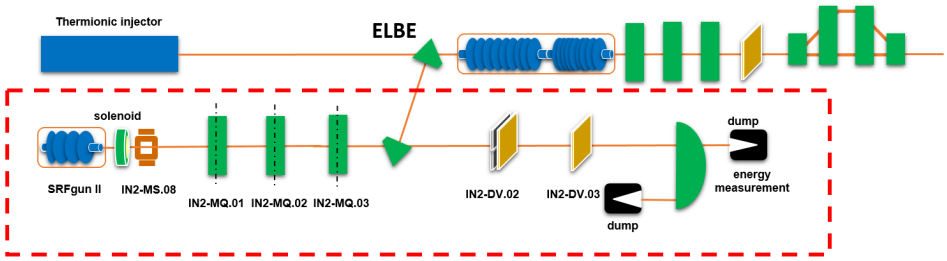

Fig. 6.19 Beamline at SRF gun and ELBE for quadrupole scan scheme.

6.2.1 Quadrupole strength calibration

Before the quadrupole scan, one should check the quadrupole focal strength. To calibrate the quadrupole magnetic field, one steerer is set up before the quadrupole, and one screen is in the downstream position. The beam spot position and divergence at the screen position can be derived from transport matrixes.

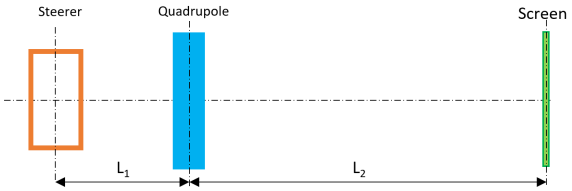

Fig. 6.20 Quadrupole strength calibration setup.

$$\begin{pmatrix} x_s \\ x_s^{'} \end{pmatrix} = \begin{pmatrix} R_{11} & R_{12} \\ R_{21} & R_{22} \end{pmatrix} \begin{pmatrix} x_0 \\ x_0^{'} \end{pmatrix}$$

$$R_{12} = \frac{dx_s}{dx_0^{'}} \tag{6.4}$$

In experiments one can obtain R_{12} using the Eq. 6.4, then compare this value with R_{12} in theory. One can find the difference between ideal conditions and reality by this method. For thin-lens approximation,

$$R_{12} = L_1 + L_2 - kL_{eff}L_1L_2, \tag{6.5}$$

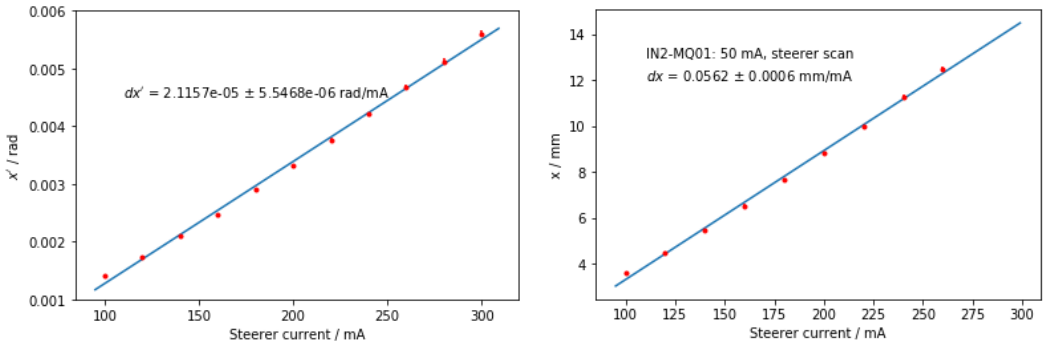

(a) (b)

Fig. 6.21 Calibration of steerer IN2-MS 08 (a) and quadrupole IN2-MQ01 with 50 mA (b).

For thick-lens focusing,

$$R_{12} = L_1 \left[C_f - L_2 \sqrt{k} S_f \right] + \frac{1}{\sqrt{k}} S_f + L_2 C_f, \tag{6.6}$$

For thick-lens defocusing,

$$R_{12} = L_1 \left[C_d + L_2 \sqrt{k} S_d \right] + \frac{1}{\sqrt{k}} S_d + L_2 C_d. \tag{6.7}$$

The definitions of C_f, S_f, C_d and S_d are as Eq. 5.6.

In the experiments, the steerer IN2-MS.08 is applied. The quadrupoles including IN2-MQ.01, the IN2-MQ.02 IN2-MQ.03 are needed to be calibrated, and the screen IN2-DV.02 gives the position and shape of the beam. The parameters of quadrupole calibration are in the Tab. 6.3. In the table, L_1 and L_2 mean the steerer to the quadrupole distance and the quadrupole to the screen distance, respectively.

The first step is to calibrate the steerer function. One should switch off all the quadrupoles. Then scan the steerer current and record the beam spot position on the screen. The steerer scans scale from 60 mA to 200 mA horizontally. The drift distance from steer to screen is 2.524 m. So the divergence per mA of the beam is 2.1157×10^{-5} rad/mA, as shown Fig. 6.21 (a). The second step is setting the quadrupole current from 50 mA to 300 mA with step 50 mA and then repeating the first step. Fig. 6.21 (b) shows an example of steer scan when IN2-MQ.01 is 50 mA, $dx = 0.0562$ mm/mA. The Third step is to calculate the R_{12} value by Eq. 6.4. The last step is to fit R_{12} with different quadrupole current using equation 6.6 fit and calculate the quadrupole focusing parameters. Fig. 6.22 shows the fitting curves from experiments. One can see that the measurement results from experiment have about 10% difference to the design

Table 6.3 Three quadrupole calibration beamline parameters.

	IN2-MQ.01	IN2-MQ.02	IN2-MQ.03
L_1 (m)	0.637	0.885	1.134
L_2 (m)	1.887	1.639	1.390

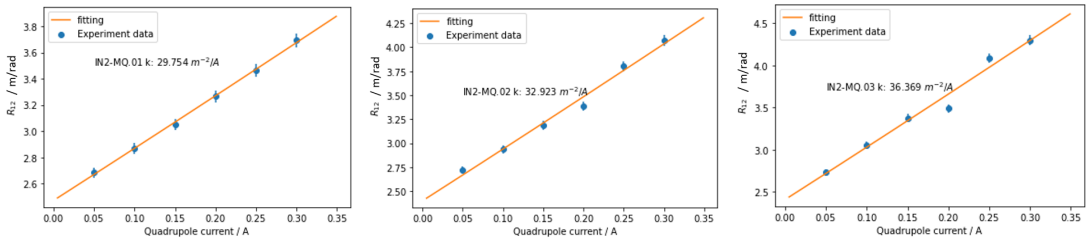

(a) (b) (c)

Fig. 6.22 Quadrupole calibration R_{12}. IN2-MQ.01 calibration (a); IN2-MQ.02 calibration (b); IN2-MQ.03 calibration (c).

Table 6.4 Three quadrupole k value.

	IN2-MQ.01	IN2-MQ.02	IN2-MQ.03
k_0 (m^{-2}/A)	32.62	32.62	32.62
k_{exp} (m^{-2}/A)	29.754	33.923	36.369
k_{exp} error (m^{-2}/A)	± 0.417	± 0.475	± 0.509

value. This difference may come from the hysteresis loop change in the experiment. As we talk about, the normalized emittance error is linear with this error and one should be carefull about the quaddrupole calibration.

6.2.2 Quadrupole scan emittance measurement results

Once the quadrupole parameters determined, the quadrupole scan emittance measurements were carried out. Beside the quadrupole to screen combination, the bunch charge, laser spot size at the photocathode, and the SC solenoid field strength were varied as it is given in Tab. 6.6. The other SRF gun parameters as the RF gradient of 8.0 MV/m and the RF phase of 44.5 degrees (3.99 MeV kinetic beam energy) remained constant. After each beam parameter change, the beam alignment with respect to the quadrupole centers were checked again. The experiments were limited to bunch charges less than 50 pC, where the expected phase space distributions should be have an approximately elliptical shape. Thus the evaluation approach for the quadrupole scan should be valid and the expected space charge effect in the drift area remains observable. Other nonlinear effects like space charge at the photocathode or solenoid

Table 6.5 The drift distance between the quadrupole and the screen.

Quad. scan No.	Quadrupole No.	Screen No.	Drift distance (m)
#1	IN2-MQ.01	IN2-DV.02	1.137
#2	IN2-MQ.01	IN2-DV.03	1.887
#3	IN2-MQ.02	IN2-DV.02	0.889
#4	IN2-MQ.02	IN2-DV.03	1.639
#5	IN2-MQ.03	IN2-DV.02	0.64
#6	IN2-MQ.03	IN2-DV.03	1.39

Table 6.6 Quadrupole scan parameters at ELBE SRF Gun beamline. D1: drift distance from quadrupole to screen; D0: distance from cathode to quadrupole; σ_{laser}: laser spot RMS size on the cathode; Q: Bunch charge; B_s: SC solenoid peak magnetic field.

Quad. scan No.	D_1 (m)	D_0 (m)	σ_{laser} (mm)	Q (pC)	B_s (T)
#1	1.137	1.624	0.625	12	0.165
#1	1.137	1.624	0.9735	16	0.1755
#1	1.137	1.624	0.625	30	0.165
#1	1.137	1.624	0.9735	45	0.1755
#2	1.887	1.624	0.625	12	0.165
#2	1.887	1.624	0.9735	16	0.1755
#2	1.887	1.624	0.625	30	0.165
#2	1.887	1.624	0.9735	45	0.1755
#3	0.889	1.872	0.625	12	0.165
#3	0.889	1.872	0.9735	16	0.1755
#3	0.889	1.872	0.625	30	0.165
#3	0.889	1.872	0.9735	45	0.1755
#4	1.639	1.872	0.625	12	0.165
#4	1.639	1.872	0.9735	16	0.1755
#4	1.639	1.872	0.625	30	0.165
#4	1.639	1.872	0.9375	45	0.1755
#5	0.64	2.121	0.625	12	0.165
#5	0.64	2.121	0.9375	16	0.1755
#5	0.64	2.121	0.625	30	0.165
#5	0.64	2.121	0.9735	45	0.1755
#6	1.39	2.121	0.625	12	0.165
#6	1.39	2.121	0.9735	16	0.1755
#6	1.39	2.121	0.625	30	0.165
#6	1.39	2.121	0.9735	45	0.1755

aberrations should not superpose the results and the possible use of fixed values of the image acquisition system in this limited bunch charge range prevented systematic errors from it.

During the measurements, the background image is subtracted from the beam images. The beam RMS size is defined as the second momentum of the beam distribution without Gaussian fitting. The image area for the calculation is defined from ROI (Region of Interest). Two evaluation methods, thin-lens approximation and thick-lens are used to obtain the experimental results. Besides the experiments, simulations with the same parameters were made, and the results were compared with the measurement results.

Fig. 6.23 shows the results. The errors of the emittance in experiments are calculated as mentioned in section 5.2.3. From the experiment results, one can see that the quadrupole calibration is necessary before the quadrupole scans. The influence of space charge in the drift space is enlarged with longer drift distances, even for a beam with about 10 pC charge. The normalized emittance of a shorter drift distance is closer to the result from the simulation. The trend of the experimental results in the case of calibrated quadrupoles agrees with that of the simulation results. The difference in the results between the experiment and simulation causes

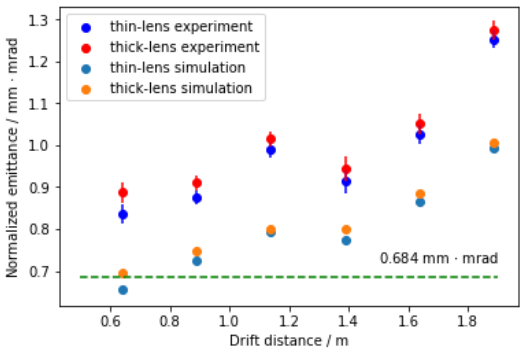

(a) 12 pC with quadrupole calibration

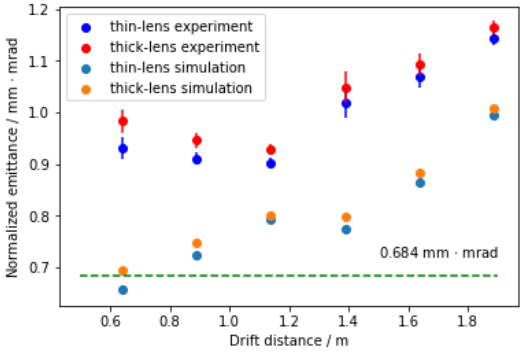

(b) 12 pC without quadrupole calibration

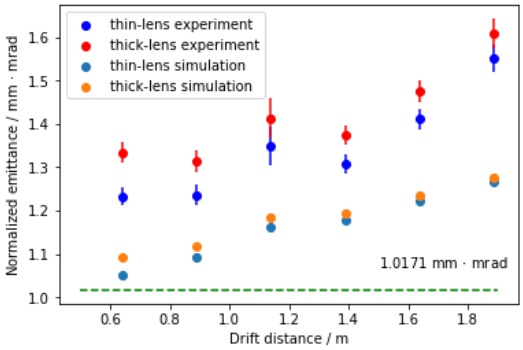

(c) 16 pC with quadrupole calibration

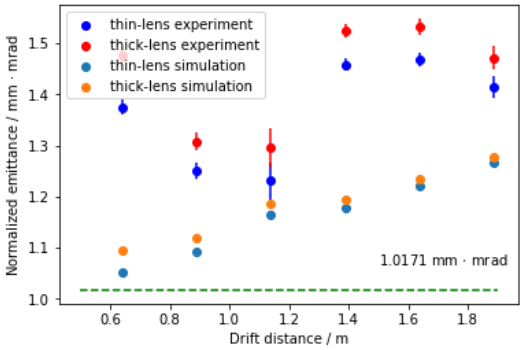

(d) 16 pC without quadrupole calibration

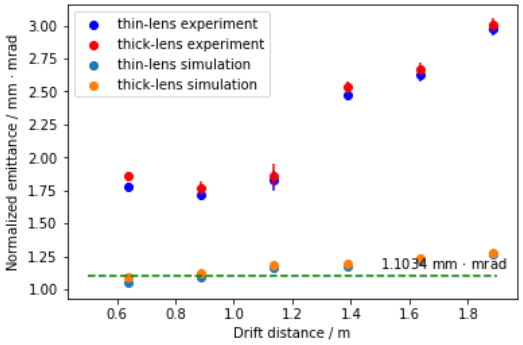

(e) 30 pC with quadrupole calibration

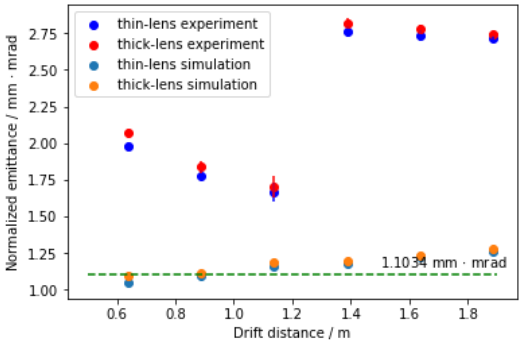

(f) 30 pC without quadrupole calibration

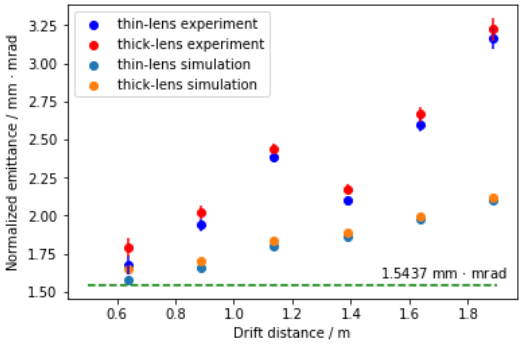

(g) 45 pC with quadrupole calibration

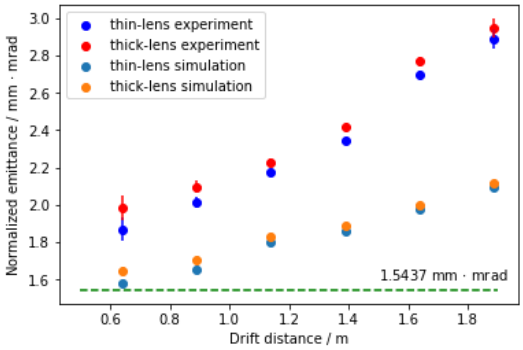

(h) 45 pC without quadrupole calibration

Fig. 6.23 Quadrupole scan at ELBE SRF Gun beamline.

from the inhomogeneous beam distribution. Two images of beam distributions on IN2-DV.02 and IN2-DV.03 without any quadrupole field, are shown in Fig. 6.26. This inhomogeneous distribution influencse the beam RMS size calculation and enlarges the calculated beam normalized emittance. However, along the drift length there are discontinuities in the measured results at the change from screen 2 to screen 3. Suspected inaccuracies in screen calibration or position values measurement proved not to be true. Thus that effect should be checked again in future.

From the simulation results in the former section, it finds that the space charge causes the unsymmetric fitting curve of quadrupole scan. The influence of the space charge will be enlarged by drift distance. So it indicates that the fitting curve for shorter drift distance has better symmetric than the longer drift distance. Fig. 6.24 shows the fitting curves by the left and right half points of the minimum point under drift distance 0.64 m and 1.887 m. It is visual that the unsymmetry with 1.887 m drift distance is more serious than that with 0.64 m drift distance except for the beam with 45 pC from fitting curves. The emittance difference between the fitting from the left side and right side of the minimum point becomes larger with the drift distance longer, shown as Fig. 6.25.

The other influence of space charge on quadrupole scan fitting curve is the shift of the curve from that without space charge influence, as talked about in the former section. From the experiment data, one can find that the difference of fitting curves between the left part and right part increases with the drift distance enlarges. However, some points, shown as the red dots in Fig. 6.25, do not agree with this trend. This phenomenon is from the unnormal beam RMS size in the experiments. Some unstable beam jitter maybe influences the RMS size calculation.

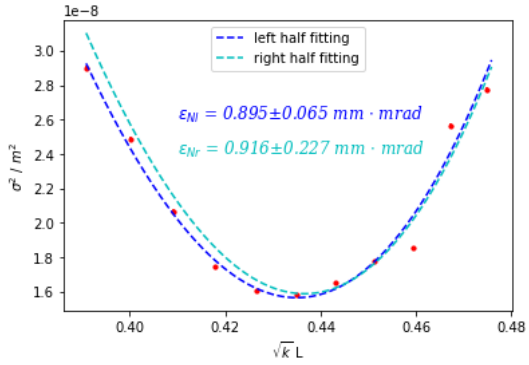

(a) 12 pC with drift distance 0.64 m

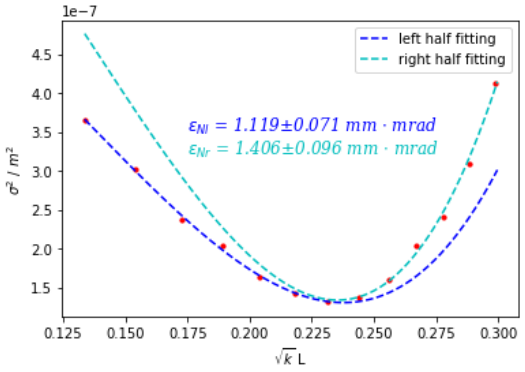

(b) 12 pC with drift distance 1.887 m

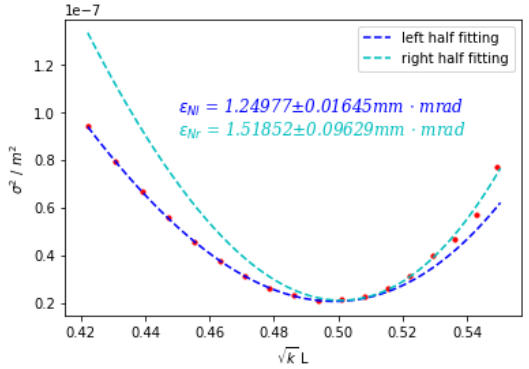

(c) 16 pC with drift distance 0.64 m

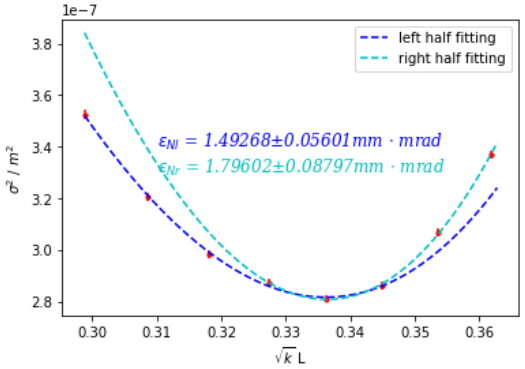

(d) 16 pC with drift distance 1.887 m

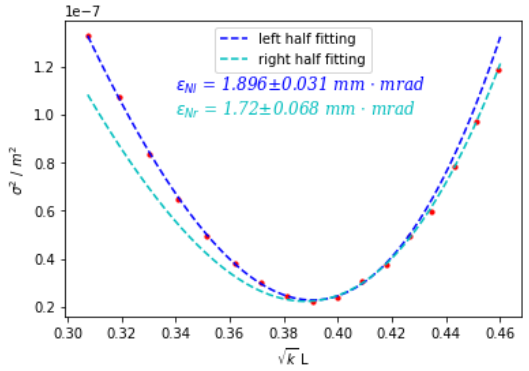

(e) 30 pC with drift distance 0.64 m

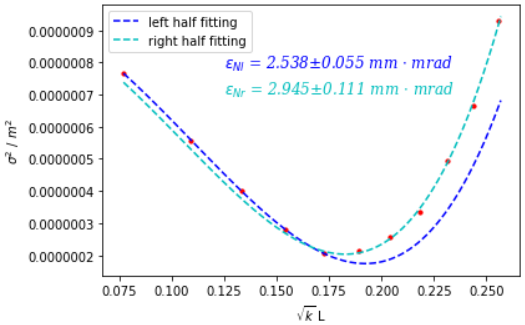

(f) 30 pC with drift distance 1.887 m

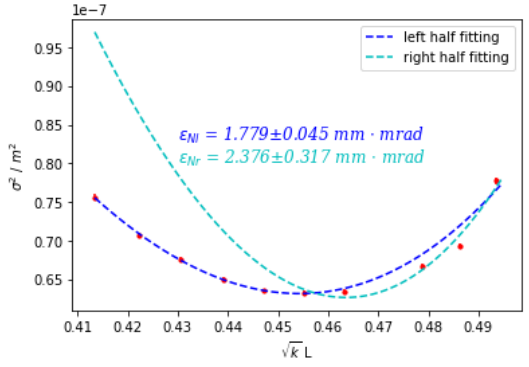

(g) 45 pC with drift distance 0.64 m

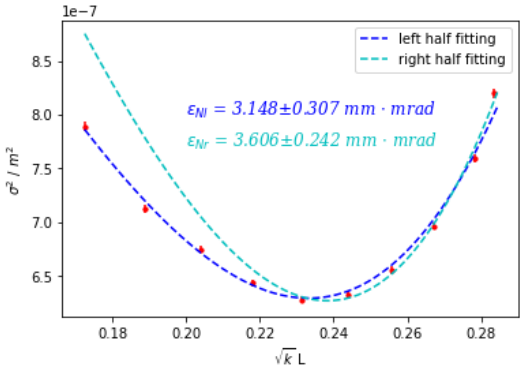

(h) 45 pC with drift distance 1.887 m

Fig. 6.24 Quadrupole scan fitting curves with different part comparison.

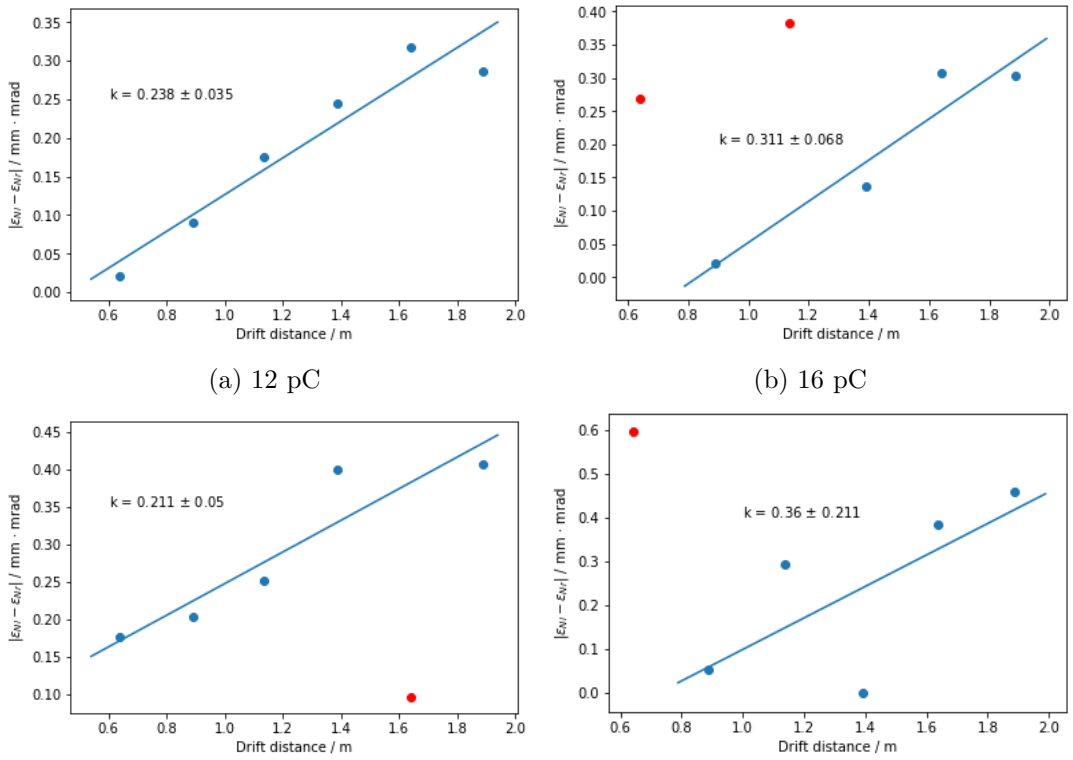

(a) 12 pC (b) 16 pC

(c) 30 pC (d) 45 pC

Fig. 6.25 Quadrupole scan emittance difference from left and right half fitting vs drift distance. In the figures, the dots are from experiments and lines are from fitting. The blue dots are the 'normal' dots and used in the linear fitting. The red dots are the 'unnormal' dots and excluded in the linear fitting.

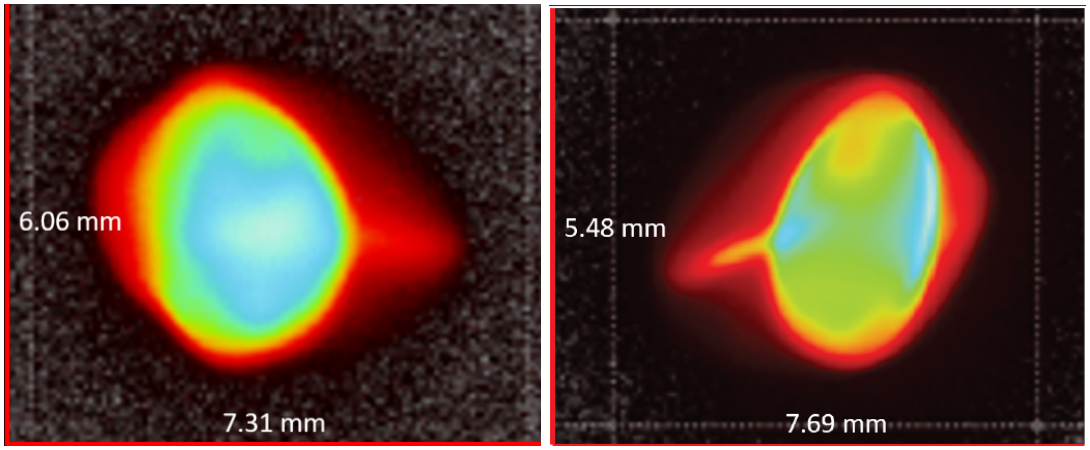

(a) (b)

Fig. 6.26 Beam distribution on IN2-DV.02 (a) and IN2-DV.03 (b).

6.3 Slit-scan emittance measurements

6.3.1 Slit-scan system setup and control system

To meet the requirements of emittance measurements at the ELBE SRF gun in connection with its user operation, i.e. speediness and accuracy, we upgraded the slit-scan setup in the diagnostic beamline (see Fig. 6.19). The slit mask is located at screen station 2 (IN2-DV.02), 2.76 m from the cathode, and the screen to get the beamlet images is located at screen station 3 (IN2-DV.03), 3.51 m from the cathode. Therefore the drift distance is 0.75 m. The ultra-high-vacuum (UHV) translation stage for the slit movement, drive motors, and control units have been replaced by advanced systems. The slit moving velocity with the new motor is now adjustable from 0 to 25 mm/s with a step resolution of 0.625 μm. The mask has one slit with 100 μm width in a sheet of 1 mm thickness. The screen used for measurements consists of YAG and has a size of 25.3 μm diameter. Considering a beam with 4 MeV kinetic energy, the minimum measured RMS emittance of this system is about 0.03 $mm \cdot mrad$. YAG is a scintillator material with high photon yield, fast decay time of 7 ns [99] and a saturation threshold, depending on the Ce doping, of about 100 fC/μm^2 [100]. The camera is a Basler scout with a maximum frame rate of 73 fps, with 659 $\times$ 494 pixels, and an analog-to-digital converter (ADC) bit depth of 12 bits. Fig. 6.27 shows the slit mask and screen at screen station 2 and 3. The calibration screen is a glass plate with a 1 cm cross scale for the calibration of the image scale of the cameras. The OTR screens were not used because of the low light emission at the beam energy of the gun. [100].

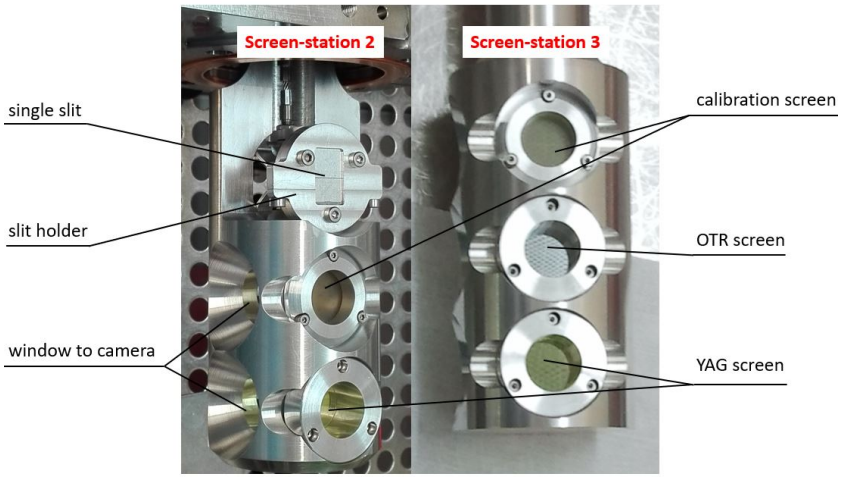

Fig. 6.27 Photograph of slit mask and screens at screen stations 1 and 2.

The control system is based on the phyMotion controller (phytron GmbH) for the slit motion and on Labview software tools for the cameras. The data processing is based on python and combined with control software in one Labview program to simplify the operations during the slit-scan emittance measurement. As shown in Fig. 6.28, the motor control and camera trigger control are two parallel loops. The beamlet images are captured while the slit is continuously moving. In the i-th loop, the slit position P_{ci} is recorded, typically at 10 Hz depending on the macro pulse trigger which indicates that the beam is on. At the same time T_{ci}, a command

is sent to the camera to capture one image. The trigger on the moment and trigger off the moment of the camera are recorded as T_{ti}, T_{ei}. During the camera exposure, the record time is T_{ri}. The camera exposure time is usually set as long as the macro pulse length to cover the full pulse and to reduce the background noise from the dark current. Taking the aforementioned into account, the exact position of the slit when the camera captures the image can be written as

$$P_{r_i} = \frac{P_{c_{i+1}} - P_{c_i}}{T_{c_{i+1}} - T_{c_i}} \cdot (T_{r_i} - T_{c_i}) + P_{c_i}. \tag{6.8}$$

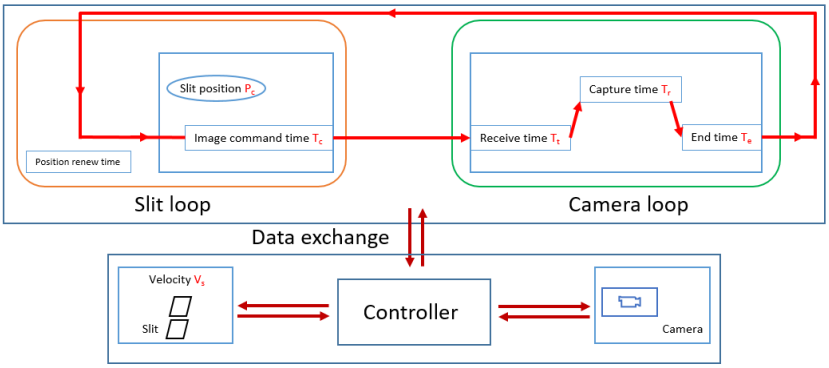

Fig. 6.28 Slit and camera control system scheme.

The time delay, coming from the PC operating system and the data exchange, is estimated to be sub-milliseconds on average, and will influence the slit position recording precision. The position of the slit according to Eq. 6.8 has around 0.2% jitter comparing with the slit widths of 100 μm and 0.25 mm/s velocity. The left diagram in Fig. 6.29 presents the slit recording position and the corresponding linear fitting line, which shows that the velocity from fitting agrees with the setting velocity. The right diagram depicts the slit step distance recorded when the camera captures the images. The standard deviation is 0.22 μm. The slit position recording jitter influences the emittance calculation, as it has been discussed in the former section. This is the only disadvantage of the fast, continuously moving slit.

6.3.2 Quadrupole corrector influence

In the former chapter, we talk about the fact that the multipole magnetic fields of the solenoid influence the beam symmetry, which can deteriorate the beam emittance. Fig. 6.30 shows a comparison of the beam shapes on screen IN2-DV.02 with the corrector switched off and on for different solenoid currents. The images show that the corrector can change the beam shape even with small currents. However, the beam spot still has a tail on the right side. This tail can not be changed with the corrector currents. It may be caused by the inhomogeneous electron emission of the cathode or the unknown anomalous field in the cavity.

This inhomogeneous beam shape has a strong influence on the transverse normalized emittance of the beam. The multiple fields, especially the quadrupole field, destroy the emittance compensation by the solenoid. The corrector can cancel the quadrupole field from the solenoid

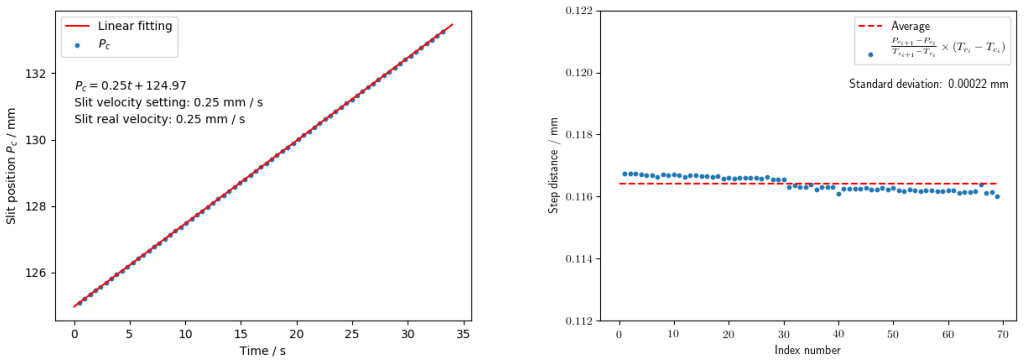

(a) (b)

Fig. 6.29 Slit moving step analysis. Recording values of slit position and slit velocity from fitting (a); Slit step jitter analysis (b).

applying suitable currents. If the corrector currents are not correct, it can increase the emittance, as analysed in the former chapter. Experimentally the variation of the normalized emittance in dependence on the corrector currents were proved, and the results are shown in Fig. 6.31. It is easy to see that the worst cases and the best cases are located in the opposite corners in Fig. 6.31 (a). It shows a periodic change with corrector currents. Fig. 6.31 (b) shows an alternative presentation of the results in (a) by using the the corrector rotation angle and the corrector focal length as axis values as calculated in the former chapter. To analyze the influence on the phase space distribution, three examples (without corrector currents, maximum, and minimum emitance) are shown in Fig. 6.32. From the beam spot images on the left in Fig. 6.32, it can be seen that the corrector can decrease the unsymmetry of the beam. The more symmetric is the beam, the smaller is its normalized emittance.

6.3.3 Beam normalized emittance versus bunch charge

The experiments were carried out with beams of different bunch charges. The SRF gun gradient was set as 8.0 MV/m with a RF launch phase of 55 degrees. The total energy of the beam was 4.45 MeV. As discussed in the former section, to subtract the dark current, every slit-scan was repeated twice where one scan was without beam and the other one with beam. The total measurement time was one and a half minutes. Tab. 6.7 shows the detailed measurement errors at four bunch charges as examples. The correction factor f_c was calculated by Eq. 5.45 and the influence of space charge, e1, was taken from the slit-scan simulation in section 5.3.8. The slit position uncertainty from the motor system was 0.2 %. The beamlet image intensity, center and RMS size uncertainties were mainly from the system uncertainty and image noise. In reality, the beamlet from the beam center was to be an evaluation of average of the whole beamlets. Fig. 6.33 shows examples of beamlet intensity, center and RMS size fluctuations at the screen position. The energy uncertainty was around 2 % in our facility due to magnet calibration and RF launch phase drift. The total error is calculated by Eq. 5.44. The normalized emittance for different bunch charges is shown in Fig. 6.34.

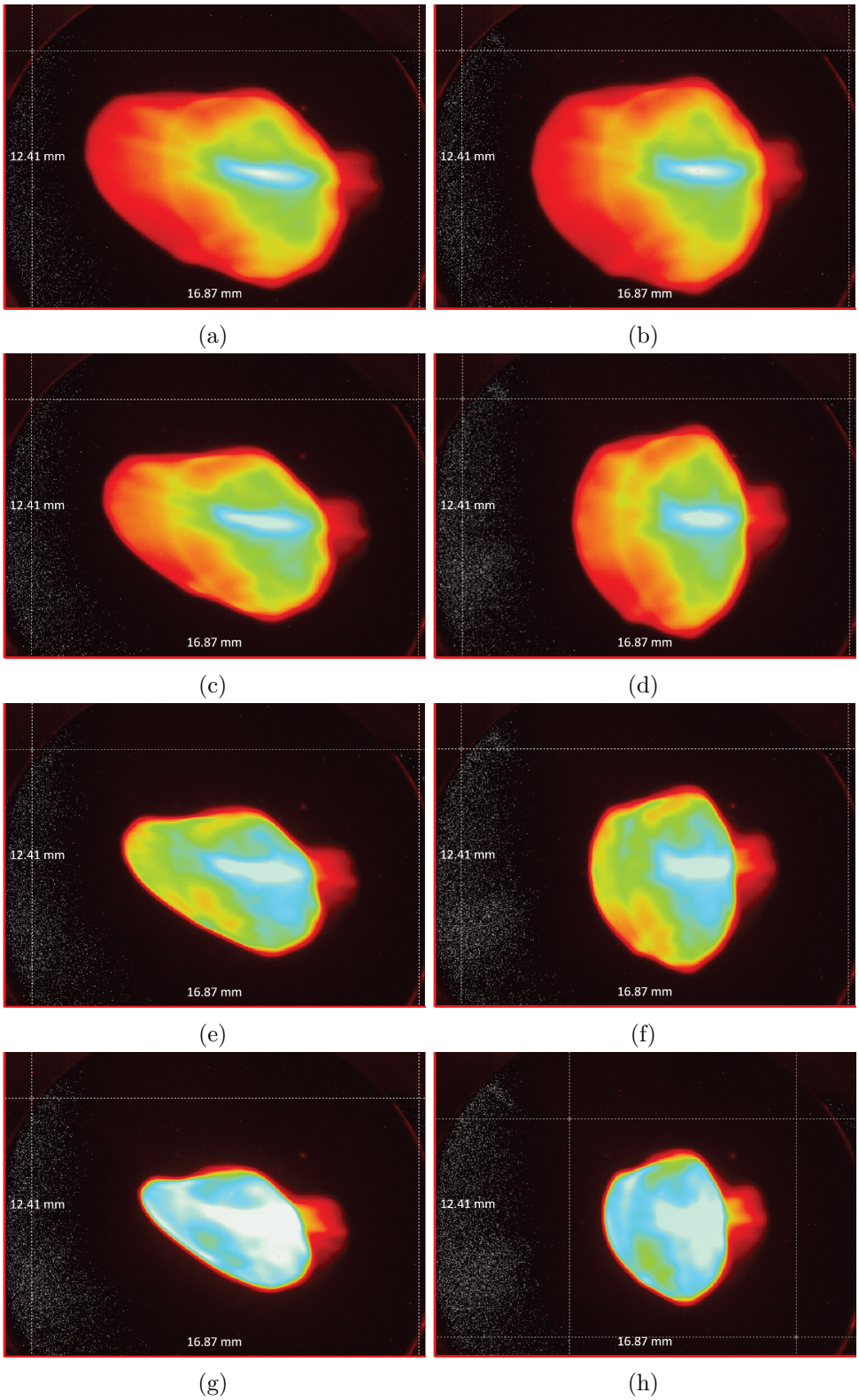

Fig. 6.30 Corrector influence on beam shape. From the first row to the fourth row, the currents of the SC solenoid are 3.6 A, 3.65 A, 3.7 A, and 3.75 A, respectively. In the left column, the currents of the corrector are 0 mA. The currents of the corrector in the right column are (514 mA, -494 mA), (1034 mA, -645 mA), (1034 mA, -645 mA), (928 mA, -645 mA).

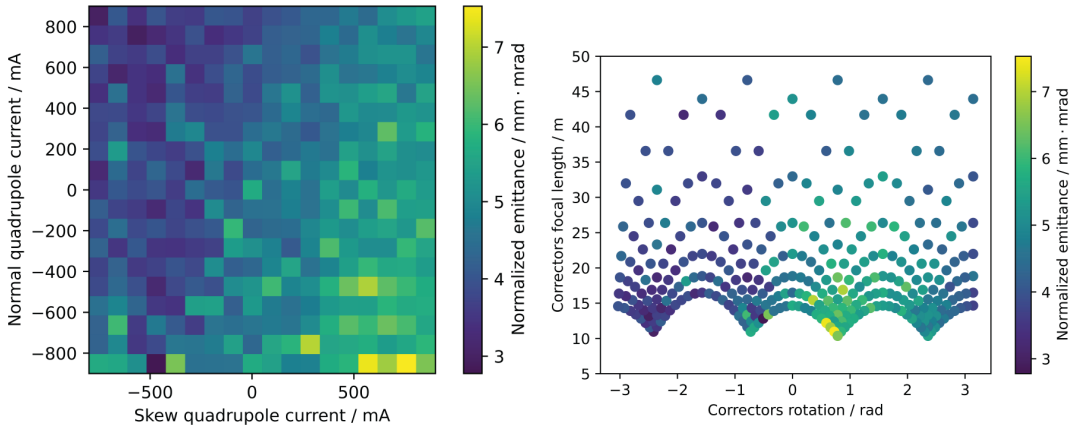

(a) (b)

Fig. 6.31 Correctors influence on beam normalized emittance. In figure (a), the dark blue point is a missing point. The bunch charge is 100 pC, kinetic energy is 3.99 MeV, gun phase is 40 degrees, solenoid current 3.66 A. The normal quadrupole current is from -900 mA to 900 mA and the skew quadrupole current is from -800 mA to 900 mA.

Table 6.7 Examples of measured normalized emittances, beam size correction factors f_c and errors.

Bunch charge / pC	f_c	$e_0(\%)$	$e_1(\%)$	$e_2(\%)$	$e_3(\%)$	$e_4(\%)$	$e_t(\%)$	ε_n / mm.mrad
50	1.07	1.8	7	0.2	8.8	2	19.8	1.90
100	1.06	0.0	8	0.2	5.0	2	15.2	3.65
159	1.04	0.0	5	0.2	4.9	2	12.1	4.04
200	1.11	0.0	3	0.2	2.5	2	7.7	4.29

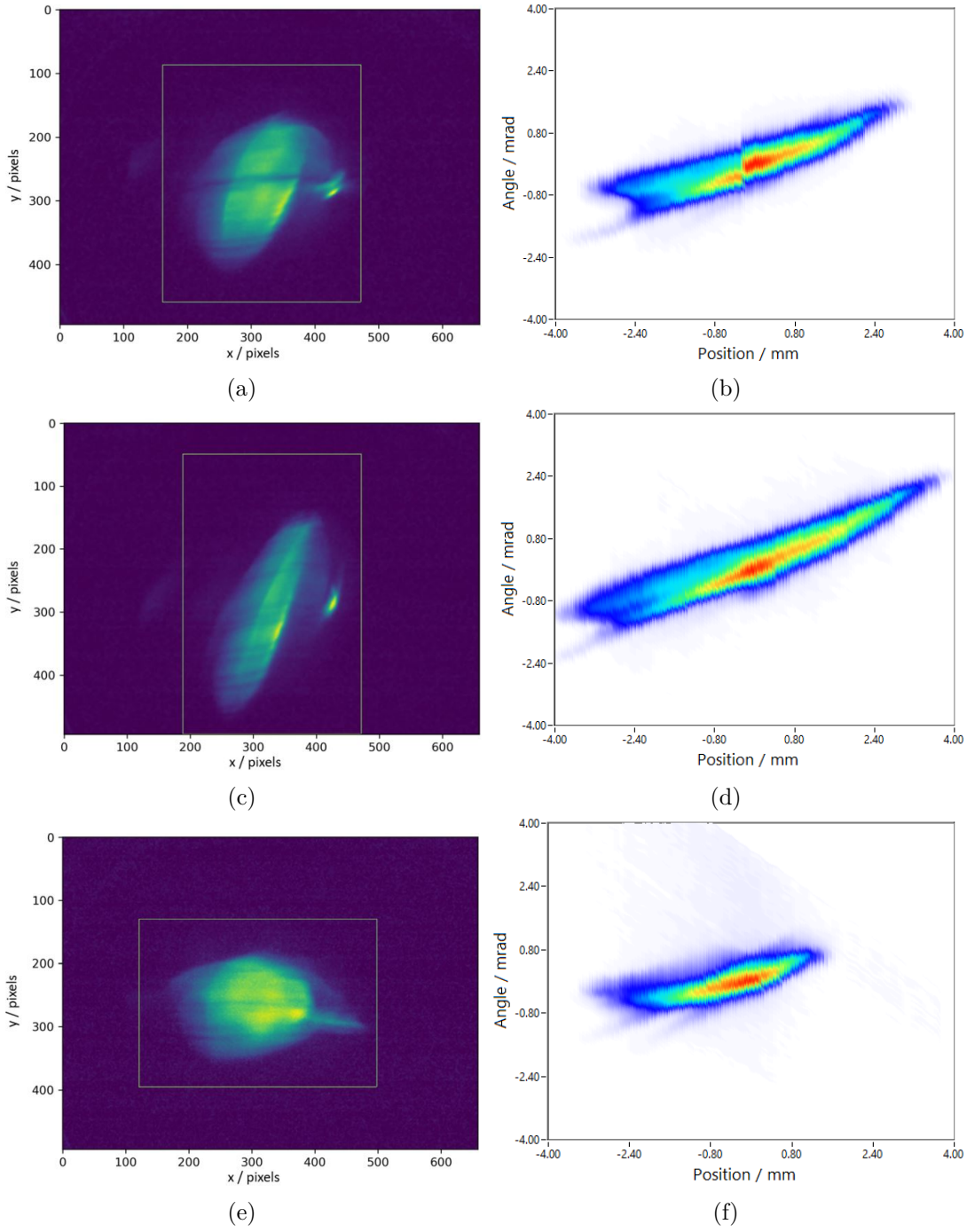

Fig. 6.32 Three types of phase space with different correctors settings. The bunch charge is 100 pC and solenoid current is 3.66 A. In figure (a) and (b), the normalized emittance is 5.68 ± 0.85 mrad · mm, without correctors; in figure (c) and (d), the normalized emittance is 7.4 ± 1.1 mrad · mm, the normal quadrupole current is 900 mA and skew quadrupole current is +600 mA; in figure (e) and (f), the normalized emittance is 2.98 ± 0.45 mrad · mm, the normal quadrupole current is -900 mA and skew quadrupole current is -800 mA; (a), (c) and (e) are the sum of all beamlet images. The pixel size is 25.3 μm (b), (d) and (f) are the phase space of the beam.

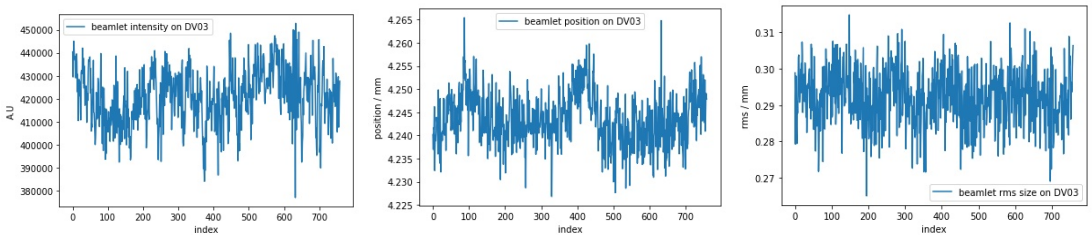

(a) (b) (c)

Fig. 6.33 Beamlet intensity (a), position (b) and RMS size (c) jitter at camera position.

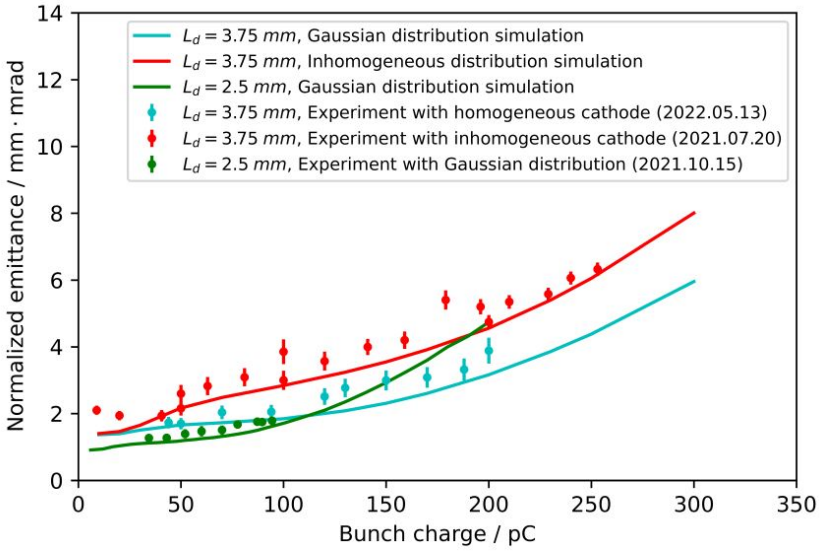

Fig. 6.34 Emittance vs bunch charge.

As a comparison with normalized emittance from experiments, ASTRA simulations with different bunch charges were performed. The initial spatial beam distribution at the cathode is defined by two effects, the QE distribution of the cathode and the transversal intensity distribution of the laser. Two different emission conditions of the cathode have been appeared in the experiments, and are shown in Fig. 6.35. In the first row of Fig. 6.35, the upper plot (a) shows an inhomogeneous QE map of the cathode. With the laser of 3.75 mm diameter with uniform distribution shown in (b), it generates a beam distribution as in (c), which is applied in the simulation with the results showing the red line in Fig. 6.34. With a smaller laser spot size of 2.5 mm, the homogenous part of the QE distribution could be selected and it produces a beam with Gaussian distribution like in Fig. 6.35 (f). In Fig. 6.34, the green line presents the emittance results of this situation. Fig. 6.35 (d) shows a well-distributed QE mapping from the experiment. Together with an uniform laser shape as in Fig. 6.35 (e), the beam at the cathode has then a Gaussian distribution. The cyan line in Fig. 6.34 is the result from this simulation with a Gaussian distribution beam. In simulation and experiments the temporal distribution of the laser was Gaussian with 2.3 ps RMS pulse length. The results from the experiments and simulation agree well with each other.

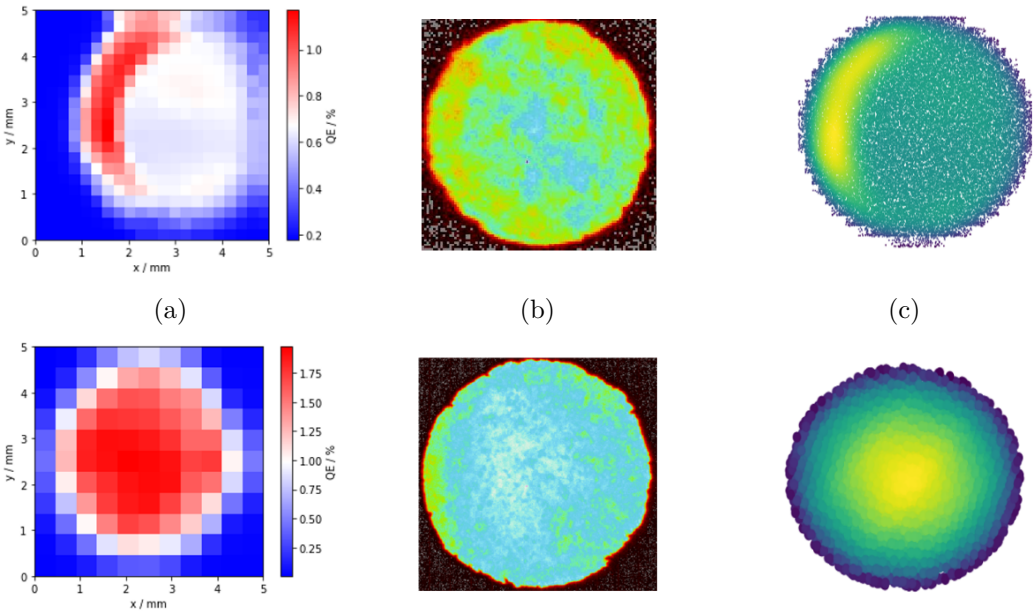

Fig. 6.35 Rebuild particles distribution from QE map and laser distribution.

6.3.4 The influence of dark current

Although during the slit-scan measurement, the background images including dark current were taken and subtracted from the beamlet images, it is meaningful to evaluate the influence of dark current. The main dark current in the SRF gun comes from the cathode and the cavity due to field emission and consist of electron pulses with a frequency of 1.3 GHz. The typical dark current is on order of 40 nA for Mg cathode [27] and 100 nA for Cs_2Te at 8 MV/m. The dark current during the measurements is stable at the same cathode, gun gradient, phase and solenoid current. Fig. 6.36 shows four different examples of dark current phase space with different conditions. Comparing the beam intensity, the influence of the dark current will be decrease when the beam bunch charge increases. Fig. 6.38 shows three groups of phase space. For the beam with bunch charge larger than 50 pC, the dark current intensity is negligible and the influence on emittance is lower than 5 %, shown in Fig. 6.37.

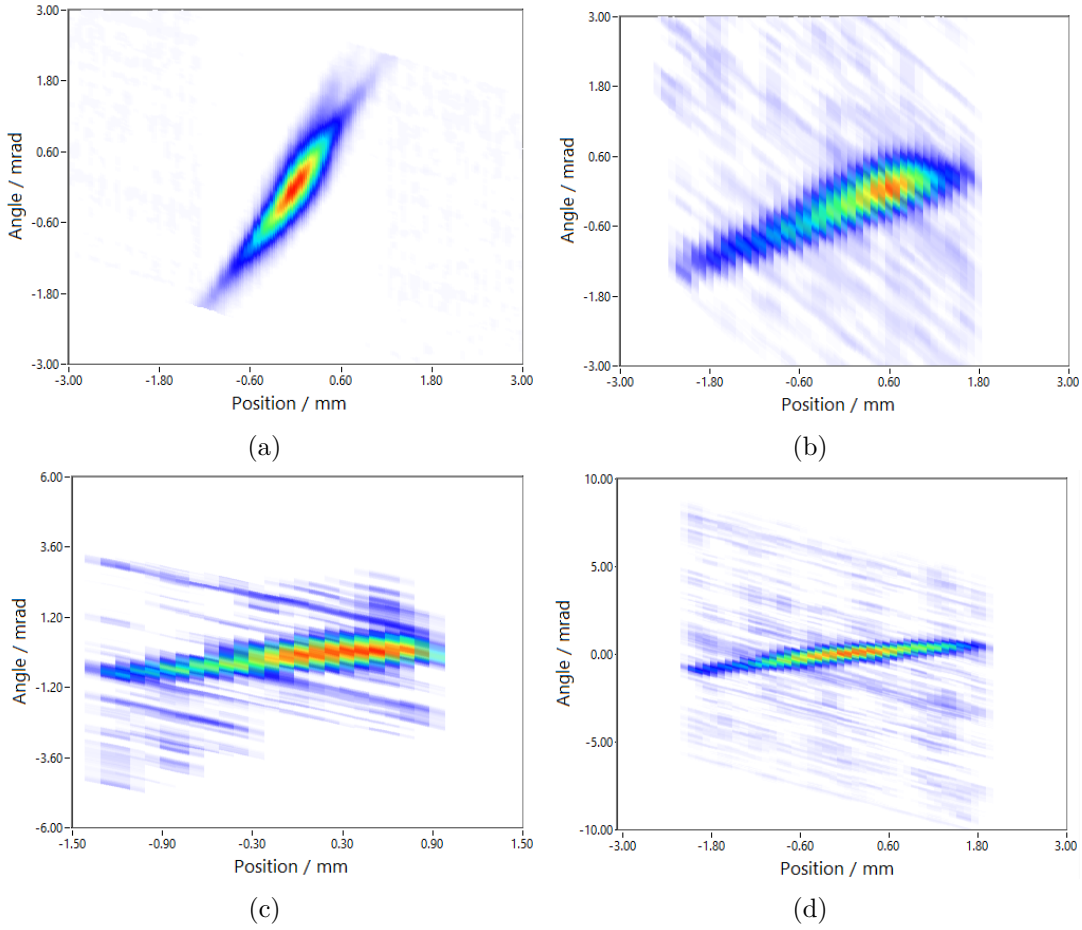

Fig. 6.36 Four different dark current phase space in different experiments.

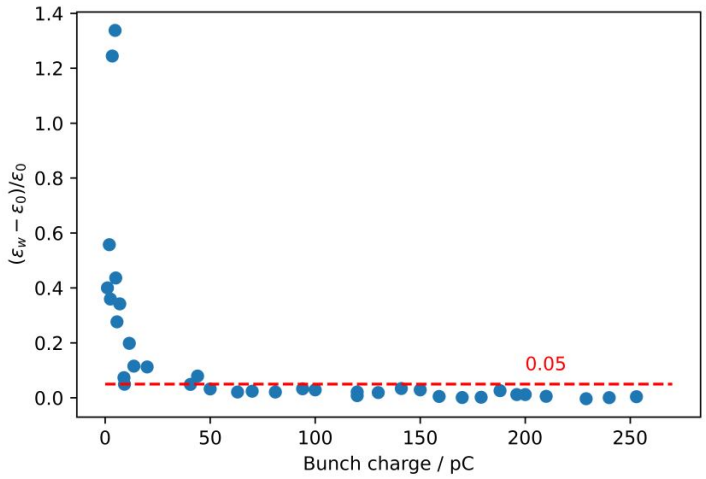

Fig. 6.37 Dark current influence on emittance vs bunch charge. ε_0 is the beam normalized emittance after subtracting the dark current. ε_w is the beam normalized emittance with dark current.

6.4 Cathode intrinsic emittance measurements

As an essential parameter of the photocathode, its intrinsic emittance is measured in the experiments. Since 2020, Cs_2Te photocathodes have been used in the SRF gun II to provide beams to ELBE for the production of coherent terahertz radiation. Here we measured the intrinsic emittance using both, the solenoid scan method, and the single shot transverse momentum imaging method to obtain the lateral distribution of the electron transverse momentum. The bunch charge was chosen as low as possible, i.e. between 50 fC to 100 fC and 120 fC. The SRF gun gradient was set to 8.0 MV/m with a RF phase of 50 degrees. To increase the SNR, the gun was operated in CW with 100 kHz repetition rate.

The first method consists of performing the solenoid scan at different laser spot sizes on the cathode. Three different laser spot diameters on the cathode, 0.5 mm, 1.25 mm, and 2.5 mm, are used. Combining the laser spatial distribution and the cathode QE map, the electron emission RMS size at the cathode is calculated as uniform distribution for all laser spot diameters.. The position of the laser spot on the cathode was at the center. The measured values of normalized emittance versus the effective laser spot RMS size and the fitting lines obtained at the YAG screens at IN2-DV.02 and IN2-DV.03 are shown in Fig. 6.39. From the results, the intrinsic emittances in horizontal and vertical directions are not the same. The vertical intrinsic emittance is about 20% to 40% higher than the horizontal one.

The second method for intrinsic emittance measurement is single shot transverse momentum imaging. In the experiments, the first step consists in the right tuning of the solenoid strength, i.e. to find its working current. For the solenoid working current, the beam spot position on the screen is independent of the laser spot position on the cathode. So the procedure are the followings: record the beam spot position on the screen while changing the solenoid current; change the laser spot position and repeat step 1; plot the beam spot position versus the solenoid current and find the cross point. The solenoid current at the cross point is the working current. Fig. 6.40 shows the solenoid current scan for different laser positions on the cathode. The

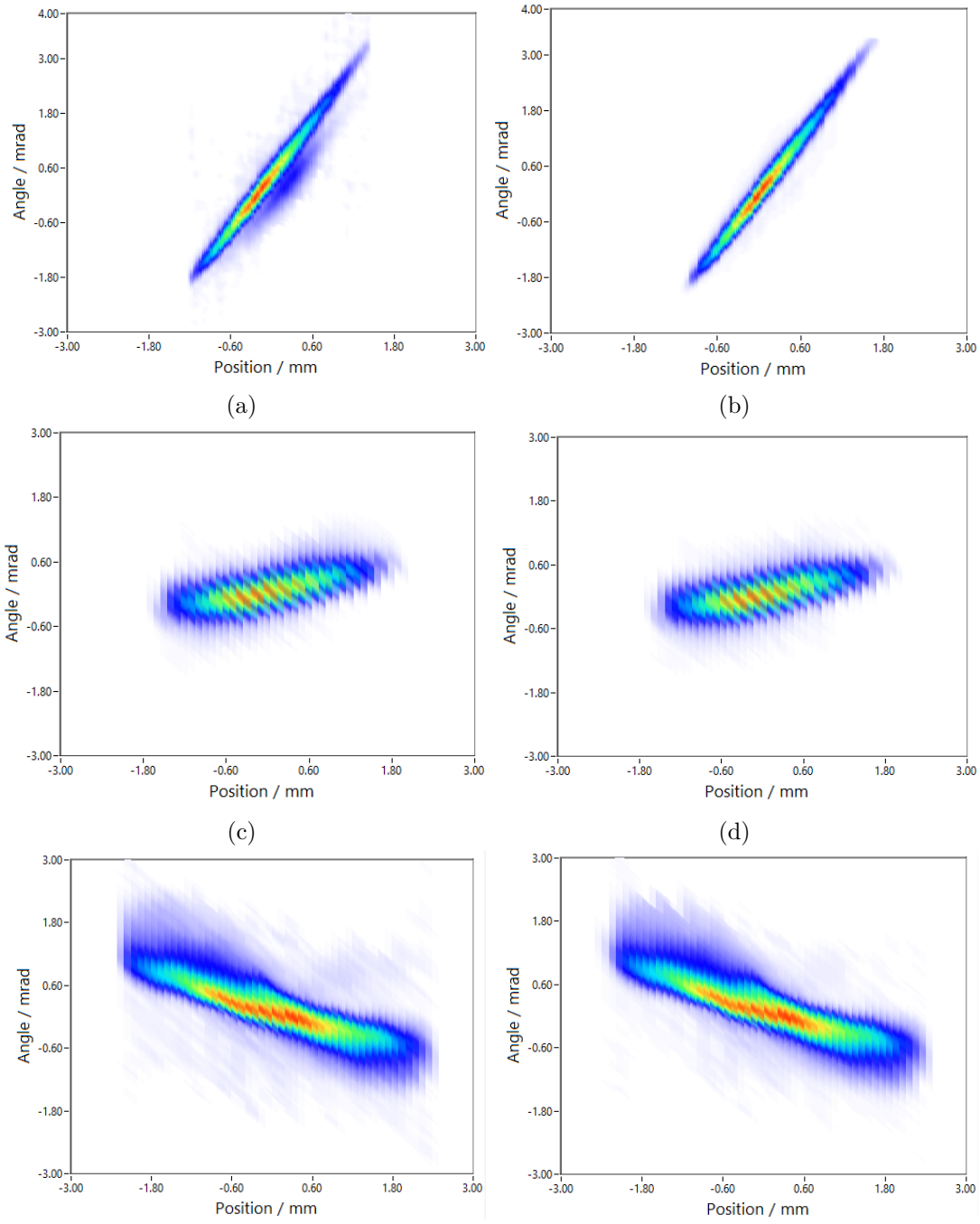

Fig. 6.38 Beam phase space of 5, 50 and 200 pC with and without dark current.

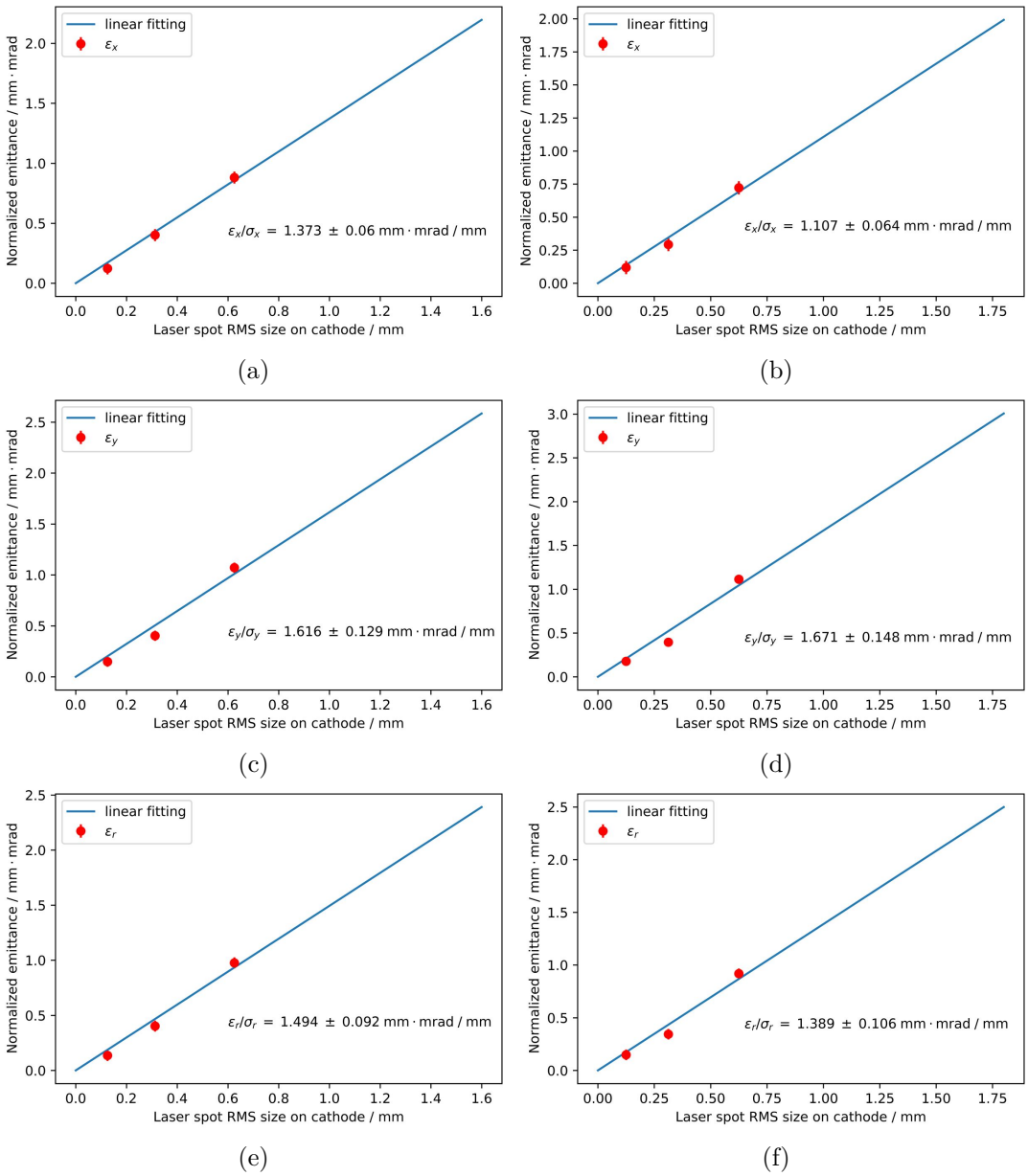

Fig. 6.39 Cathode intrinsic emittance from solenoid scan method at IN2-DV.02 and IN2-DV.03. The figures in the left column are the results from IN2-DV.02: (a) is the cathode horizontal intrinsic emittance; (c) is the cathode vertical intrinsic emittance; (e) is the cathode radius intrinsic emittance. The figures in the right column are the results from IN2-DV.03: (b) is the cathode horizontal intrinsic emittance; (f) is the cathode vertical intrinsic emittance; (f) is the cathode radius intrinsic emittance. ε_r is the average of ε_x and ε_y.

solenoid working currents for the horizontal and vertical directions are almost the same, 4.4 A (0.198 T) for screen IN2-DV.02. Using this value in simulation the M_{12} can be calculated to 0.212 $\text{mm}^2/(\text{mm} \cdot \text{mrad})$. Although for the vertical direction, the solenoid current has an uncertainty of about 0.07 A (0.004 T) for IN2-DV.02. At the end, the beam RMS size on the

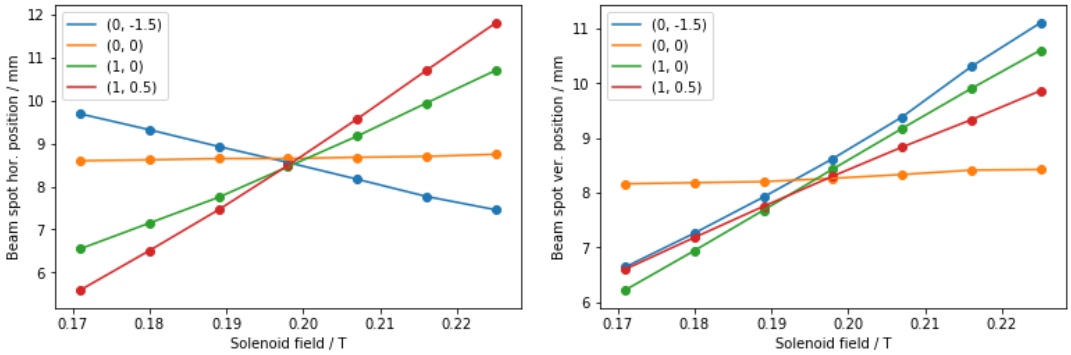

(a) (b)

Fig. 6.40 Solenoid working current for the screen at IN2-DV.02. (a) is the horizontal position and (b) is the vertical direction. The positions of the laser spot on the cathode are in the brackets with unit of mm. The original position, (0, 0), is center of the QE map. The cross point's horizontal axis are 0.196 ± 0.003 T.

Table 6.8 Thermmal emittance comparison between solenoid scan and sigle shot thermal emittance mapping with 1.2% QE.

	Theory	Solenoid scan			Mapping		
	10% QE	x	y	r	x	y	r
Thermal emittance (mm mmrad/mm)	0.9	1.373 ± 0.060	1.616 ± 0.129	1.494 ± 0.092	0.976 ± 0.137	1.011 ± 0.142	0.995 ± 0.139

screen is recorded while laser spot is scanned across the cathode, and the thermal emittance is calculated for these different positions on the cathode. Fig. 6.41 shows the intrinsic emittance mapping in horizontal and vertical directions at IN2-DV.02. The intrinsic emittance in radius is calculated and compared with the QE mapping of the cathode. In principle, the position with high QE will has high intrinsic emittance. The intrinsic emittance maps agree with the QE map well. The left part with higher QE has higher intrinsic emittance than the right part with lower QE.

6.4.1 The error of cathode intrinsic emittance measurement

The comparison of intrinsic emittance between the results from the solenoid scan and single shot intrinsic emittance mapping is shown in Tab. 6.8. The results of the single shot intrinsic emittance mapping in the table are the average of an area at the center with 1.25 mm radius. The intrinsic emittance from the solenoid scan is between 40% to 60% larger than that from the mapping method. In solenoid scan, the beam from the larger laser spot size on the cathode with 2.5 mm diameter experienced more anomalous or inhomogeneous fields which enlarge the emittance results [101]. One can see it obviously from Fig. 6.39. The laser spot diameter used for mapping is 0.5 mm, which gives more accurate results. Both the intrinsic emittances from the solenoid scan and frm mapping are larger than the theoretical value [63]. A possible source

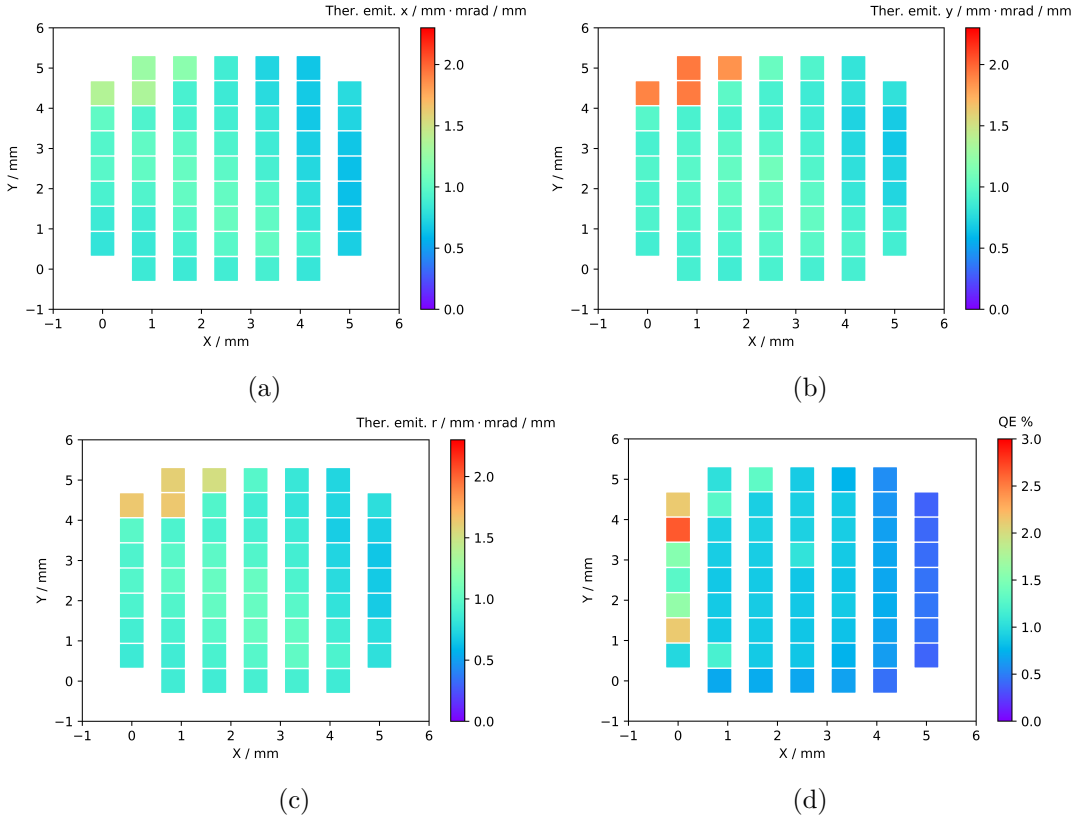

Fig. 6.41 Cathode intrinsic emittance mapping and QE mapping. (a), (b) and (c) are intrinsic emittance in horizontal, vertical and radius, respectively. The distance between the solenoid and the IN2-DV.02 is 2.011 m. The last figure is the QE map of the cathode.

could be the roughness of the cathode. The rough surface emittance together with the strong electric peak field of the applied RF field can increase the intrinsic emittance. The bunch charge for intrinsic emittance measurement is in the range of 50 fC to 100 fC to avoid the influence of space charge. However, due to this low beam current, the dark current can contribute to the emittance result if the contribution are not separated. Thus, the dark current should be substracted in these measurements to reduce its influence. For the single shot transverse momentum imaging method, one error results from the uncertainty of the solenoid current adjustment. A deviation from the working current arises a contribution of the initial beam size on the cathode. The beam spot center movements are 0.19 mm in horizontal and 0.36 mm in vertical direction when the laser spot is moved by 1.5 mm on the cathode with the solenoid field 0.196 T. This indicates that the M_{11} is less than 0.240. Considering that the initial beam RMS size is 0.125 mm, M_{12} is 0.212 $mm^2/(mm \cdot mrad)$, and the intrinsic emittance is 1.0 $mm \cdot mrad/mm$, then the error is less than 14.2 % calculated from Eq. 5.71.

Chapter 7

Conclusions and outlook

Conclusions

As the transverse emittance is an essential parameter to the photo injector, this Ph.D. work has optimized the SRF gun II transverse emittance further based on the SC solenoid emittance compensation. It contains four parts: SC solenoid field measurement and analysis, multipole fields of the SC solenoid analysis and optimization, beam transverse emittance measurement using fast slit-scan and quadrupole scan methods, and the cathode intrinsic emittance measurement and mapping.

The influence of SC solenoid spherical aberration on emittance is analyzed. It strongly relays on the beam RMS size at solenoid position with fourth power and is proportional to the spherical aberration coefficient. To minimize this kind of influence, not only does the beam RMS size at the solenoid position decreases by increasing the cathode and laser qualities in experiments, but also the SC solenoid is optimized in our group. It shows that the spherical aberration coefficient of the new design reduces by 44.4 % in this thesis. The newly designed SC solenoid fields are obtained using a 1-D longitudinal field Hall probe and a 3-D Hall probe for transverse fields. The newly designed SC solenoid simulation is made based on the finite element analysis software Comsol Multiphysics to demonstrate the effectivity of the formalism fitting and evaluate the accuracy in field analysis. The field measurement is conducted when the SC solenoid works at the superconducting condition in the cryomodule. From the 1-D longitudinal field Hall probe results, the longitudinal field is linear to the current with a slope of 35.232 $\pm$ 0.021 mT/A. The effective length is 50.990 $\pm$ 0.068 mm. These parameters agree with the designed requirements. The alignment and transverse multipole fields are analyzed based on the 3-D Hall probe data. The center of the SC solenoid has a tilt of 9.739 $\pm$ 7.239 mrad and an offset of 1.599 $\pm$ 1.193 mm in the horizontal direction, and a tilt of -22.043 $\pm$ 2.263 mrad and an offset -0.789 $\pm$ 0.561 mm in the vertical direction. Applying the formalism fitting method, the transverse multipole fields due to the tilt and offset are obtained. The coefficients of the dipole field and the quadrupole gradient are proportional to the current absolute value from the measured data. The sextupole coefficient remains low but is independent of the current. These results are a kind of magnitude evaluation rather than high accuracy due to four primary error sources analyzed in detail, including imperfect Hall probe mechanical alignment, imperfect degaussing of the iron yoke, the Hall probe intrinsic error, and the fitting error. At 5 A, the integrations

of the dipole field, quadrupole gradient, and sextupole field coefficient of the SC solenoid are about 200 ± 40 mT·mm, 0.166 ± 0.085 mT, and 0.03 ± 0.027 mT/mm, respectively.

Furthermore, the influence of the anomalous quadrupole field in the solenoid on beam transverse emittance is analyzed using beam linear transport theory and ASTRA simulation. The quadrupole focal strength and the phase change the influence. According to the quadrupole field of the SC solenoid field measurement result, it is possible to enlarge the beam transverse emittance almost 2.5 times in the worst situation. In the experiments, the beam shape can reflect the influence of the anomalous quadrupole field from the solenoid. It becomes asymmetric when the quadrupole field influence is strong. The correctors have been installed in the beamline to cancel the influence of the quadrupole field from the solenoid and correct the asymmetric beam shape. Visible from the slit-scan emittance measurement results, the installed correctors can clearly decrease the influence of the quadrupole field mode of the SC solenoid, especially for the high bunch charges. The correctors can correct the beam asymmetry at appropriate settings. The beam shape at the slit position is closer to a round spot, and the emittance reduces by 47.5 % for 100 pC. The influence of the sextupole field on the emittance is analyzed qualitatively, and shows that the additional emittance is linear with beam RMS size to the third power and the second differential of the longitudinal solenoid field. For instance, in a beam with 500 pC bunch charge and RMS size of 4.0 mm at the solenoid position, the sextupole field of the solenoid with 5 A will increase the emittance by 16 % and 25 % higher for uniform and Gaussian distributions.

The fast slit-scan transverse emittance measurement equipment has been constructed in the beamline based on a continuously moving slit and a YAG screen. It takes about 90 seconds for one measurement. The control system and data processing are programmed by Labview and Python and combined in one user interface. The control system has two parallel subsystems, one for the motor of the slit and the other for the camera. The beamlet images are captured continuously during the slit moving. Two kinds of machine learning algorithms are applied to shorten the beamlet image processing time and improve the beamlet center position and RMS size accuracy. The first one is a classified neural network to distinguish beamlet images from the whole captured images. The accuracy of this network is 98.2 % after training. The second is an autoencoder neural network that can abstract the beamlet features from the images and reconstruct the beamlet distribution in 1-D to depress the noise and increase the signal-noise ratio. A dataset including 0.17 million beamlet images based on experiments is built, and 80 % for training and left 20 % for evaluation. The training and evaluation work is completed on the Maxwell HPC Cluster at DESY. It has been demonstrated that ML algorithms can work efficiently with beamlet images for image classification and depressing image noise better than traditional methods. Additionally, slit-scan emittance measurement simulations are made using ASTRA to study the three factors influencing the emittance result: the slit width, drift distance, and space charge. In general, a slit with smaller width gives a better beam emittance resolution and minor emittance error, especially for a beam with a small emittance. An experimental equation is concluded to evaluate the error from the slit width. It is necessary to consider the influence of the space charge for the beamlet density to keep the same after the slit. From the simulation results, the space charge influence on emittance measurement results will be enlarged as the drift distance becomes long. However, for the shorter drift distance, the resolution of the beam divergence should be higher. At the present conditions in the SRF gun diagnostic beamline, the error of slit-scan emittance resulting from the space charge is less than 3 %. The

other emittance error sources of the slit-scan are analyzed carefully, including the slit position recording uncertainty, beamlet center error, RMS size uncertainty, beamlet total intensity uncertainty, and beam energy uncertainty. To simplify the calculations, the independence of every source is assumed in the analysis. Two coordinates located at the slit and screen positions will be coupled due to the beamlet center, RMS, and intensity uncertainties. The emittance error is proportional to these uncertainties ignoring the higher order small terms. Besides these sources, the intensity loss of weak beamlets is considered by introducing a coefficient for the beam RMS size at slit position which scales the reconstructed beam RMS size. In most cases, this factor is larger than one. As seen from the simulation, the beamlet has a halo and reduces the signal-to-noise ratio. This result in the rebuild beam RMS size being smaller than the original size. At the end of this part, two kinds of beam original distributions from experiments, one Gaussian distribution and one inhomogeneous distribution, are applied in ASTRA simulation. The beam normalized emittance results from the slit-scan are compared with the ASTRA original emittance, and they are coincident.

The other traditional emittance measurement method, the quadrupole scan, is analyzed. It is necessary to calibrate the quadrupole focal strength before scanning the quadrupole and measuring the beam RMS size. A straightforward quadrupole focal strength calibration method without intervention is applied and works effectively in the experiments. It consists of a steerer upstream of the quadrupole and a screen downstream. Based on the transport matrix between the quadrupole and the screen, one can calculate R_{12} in theory and experiments and calibrate the quadrupole focal strength by comparing these two terms. The results show a 10% difference between the experiment and the design value. The next step is to record the beam RMS sizes along different quadrupole focal strengths. Because the data analysis is based on linear beam transport theory, it ignores the influence of the space charge in the calculation. The quadrupole scan simulation based on ASTRA shows that the influence of space charge will be enlarged as the drift distance becomes larger. Moreover, the space charge will destroy the fitting curve symmetry and enlarge the emittance calculation result. Two fitting methods, thin-lens, and thick-lens, are carried out in the quadrupole scan data analysis. The simulation results show that the thick-lens fitting has a better performance at a small drift distance. However, the thin-lens fitting gives a more precise emittance result for long drift distances. The errors of quadrupole scan are from curve fitting and quadrupole focal strength uncertainty. The fitting error is based on the covariance matrix from the fitting and the beam RMS size standard deviation. The emittance error is linear with the quadrupole focal strength error.

The last part measures the intrinsic emittance of the Cs_2Te cathode using solenoid scan and single shot transverse momentum imaging. In theory the intrinsic emittance of Cs_2Te is 0.9 $mm \cdot mrad/mm$. The bunch charge during the measurements is in the range of 50 fC to 100 fC to avoid the influence of the space charge in the solenoid scan. Three different laser spots are used in the solenoid scan with diameters of 0.5 mm, 1.25 mm, and 2.5 mm. After linear fittings, the intrinsic emittance at QE of 1.2 % are 1.373 ± 0.030 $mm \cdot mrad/mm$ in horizontal direction, and 1.616 ± 0.129 $mm \cdot mrad/mm$ in vertical direction. The average intrinsic emittance is 66 % higher than that given in theory. The solenoid scan method can only measure one average intrinsic emittance of a given area. The single shot intrinsic emittance method is applied to map the whole cathode. At a suitable solenoid current, the term M_{11} in the matrix from the cathode to the screen becomes zero. Then the beam RMS size only depends on the beam's initial transverse momentum. Combining the ASTRA simulation, M_{12} is calculated as 0.212

$mm^2/(mm{\cdot}mrad)$. The smallest size of laser spot of a diameter of 0.5 mm is adopted in the mapping to avoid the nonlinear factors. The intrinsic emittance maps in horizontal and vertical directions are obtained in a range of 5 mm on the cathode, similar to the QE map. The intrinsic emittance at the cathode center position is 0.976 ± 0.137 mm $\cdot$ mrad/mm in horizontal direction and 1.011 ± 0.142 mm $\cdot$ mrad/mm, which is 10.6 % higher than the theory value. The error source of this method is mainly from the uncertainty of the solenoid working current, which will introduce an influence of M_{11}, i.e. of the beam size at the cathode. During the measurements, this error is less than 14.2 %.

Outlook

A group of quadrupoles has corrected the parasitic quadrupole mode of the SC solenoid, but the effect of the sextupole field of the SC solenoid is ignored. The study of the sextupole field influence on the transverse emittance is still insufficient. Some fundamental analysis is done under idealized conditions. However, simulations are needed as replenishment. Furthermore, installing a group of sextupole magnets should be considered to correct the sextupole field from the SC solenoid if necessary.

The other part is related to the machine learning algorithms. Artificial neural networks possess a wide potential application in beamlet images processing. It is possible to distinguish the dark current in the beamlet images automatically. Also, such an algorithm can be used to reconstruct the beam phase space directly from the beamlet images and calculate the beam emittance from the phase space. For these applications, the key points are reliable data sets and robust network structures.

It is necessary to find a method, how the corrector currents can be optimized based on the measured beam shape automatically. At present, this work is manually performed based on the beam roundness on the YAG screen. An automatic control system for the correctors should be constructed to speed up the preparation of the emittance measurement and of the user beamline settings. The cathode intrinsic emittance mapping can be combined with the QE mapping, giving a full overview of the cathode performance during its life time.

Bibliography

[1] E. M. McMillan. The synchrotron-a proposed high energy particle accelerator. *Physical Review*, 68(5-6):143, 1945.

[2] A. Sessler. *Engines of discovery: a century of particle accelerators*. World Scientific, 2014.

[3] P. Willmott. *An introduction to synchrotron radiation: techniques and applications*. John Wiley & Sons, 2019.

[4] M. Reiser. *Theory and design of charged particle beams*. John Wiley & Sons, 2008.

[5] U. Bergmann et al. Science and technology of future light sources: A white paper. Technical report, SLAC National Accelerator Lab., Menlo Park, CA (United States), 2009.

[6] Light sources. https://lightsources.org/.

[7] G. Brown et al. Wiggler and undulator magnets - a review. *Nuclear Instruments and Methods in Physics Research*, 208(1-3):65–77, 1983.

[8] B. Buras and G. Materlik. The European synchrotron radiation facility: an overview. *Nuclear Instruments and Methods in Physics Research Section A: Accelerators, Spectrometers, Detectors and Associated Equipment*, 246(1-3):21–31, 1986.

[9] R. Hettel. DLSR design and plans: an international overview. *Journal of synchrotron radiation*, 21(5):843–855, 2014.

[10] M. Eriksson et al. Diffraction-limited storage rings–a window to the science of tomorrow. *Journal of synchrotron radiation*, 21(5):837–842, 2014.

[11] H. Motz. Applications of the radiation from fast electron beams. *Journal of Applied Physics*, 22(5):527–535, 1951.

[12] P. Schmüser et al. Free-electron lasers in the ultraviolet and X-ray regime. *Springer Tracts in Modern Physics*, 258, 2014.

[13] Claudio Pellegrini. The history of x-ray free-electron lasers. *The European Physical Journal H*, 37(5):659–708, 2012.

[14] S. Humphries. *Charged particle beams*. Courier Corporation, 2013.

[15] B. Dunham et al. Record high-average current from a high-brightness photoinjector. *Applied Physics Letters*, 102(3):034105, 2013.

[16] A. Bartnik et al. Operational experience with nanocoulomb bunch charges in the Cornell photoinjector. *Physical Review Special Topics-Accelerators and Beams*, 18(8):083401, 2015.

[17] C. Gulliford et al. Demonstration of cathode emittance dominated high bunch charge beams in a DC gun-based photoinjector. *Applied Physics Letters*, 106(9):094101, 2015.

[18] N. Nishimori et al. Operational experience of a 500 kV photoemission gun. *Physical Review Accelerators and Beams*, 22(5):053402, 2019.

[19] F. Stephan and M. Krasilnikov. High brightness photo injectors for brilliant light sources. *Synchrotron Light Sources and Free-Electron Lasers: Accelerator Physics, Instrumentation and Science Applications*, pages 603–646, 2020.

[20] F. Sannibale et al. High-brightness beam tests of the very high frequency gun at the Advanced Photo-injector EXperiment test facility at the Lawrence Berkeley National Laboratory. *Review of Scientific Instruments*, 90(3):033304, 2019.

[21] J. Sekutowicz et al. SRF gun development overview. In *Proc. 17th Int. Conf. RF Superconductivity (SRF'15)*, pages 994–1000, 2015.

[22] E. Vogel et al. Status of the all superconducting gun cavity at DESY. *SRF'19*, pages 1087–1090, 2019.

[23] R. Xiang et al. Review of superconducting radio frequency gun. In *12th Int. Particle Accelerator Conf.(IPAC'21), Campinas, Brazil*, 2021.

[24] H. J. Qian et al. Overview of CW RF guns for short wavelength FELs. In *39th International Free-Electron Laser Conference, number PUBDB-2019-04439 in Photoinjektor*, 2019.

[25] J. K. Hao et al. Recent progresses on DC-SC photoinjector at Peking University. 2005.

[26] P. Michel et al. The Rossendorf IR-FEL ELBE. In *Proc. FEL*, page 488. Citeseer, 2006.

[27] J. Teichert et al. Successful user operation of a superconducting radio-frequency photoelectron gun with Mg cathodes. *Physical Review Accelerators and Beams*, 24(3):033401, 2021.

[28] J. Klug et al. Development of a neutron time-of-flight source at the ELBE accelerator. *Nuclear Instruments and Methods in Physics Research Section A: Accelerators, Spectrometers, Detectors and Associated Equipment*, 577(3):641–653, 2007.

[29] B. Green et al. High-field high-repetition-rate sources for the coherent THz control of matter. *Scientific reports*, 6(1):1–9, 2016.

[30] A. Jochmann et al. High resolution energy-angle correlation measurement of hard X rays from laser-Thomson backscattering. *Physical review letters*, 111(11):114803, 2013.

[31] R. Xiang et al. Running status of SRF gun-II at ELBE center. In *29th Linear Accelerator Conf*, 2018.

[32] A. Arnold et al. RF Perfomance Results of the 2nd ELBE SRF Gun. Technical report, Thomas Jefferson National Accelerator Facility (TJNAF), Newport News, VA (United States), 2015.

[33] H. Vennekate et al. Emittance compensation schemes for a superconducting rf injector. *Physical Review Accelerators and Beams*, 21(9):093403, 2018.

[34] P. Lu et al. Simulation of ELBE SRF gun II for high-bunch-charge applications. *Nuclear Instruments and Methods in Physics Research Section A: Accelerators, Spectrometers, Detectors and Associated Equipment*, 830:536–544, 2016.

[35] Vladimir Igorevich Arnol'd. *Mathematical methods of classical mechanics*, volume 60. Springer Science & Business Media, 2013.

[36] H. Wiedemann. *Particle accelerator physics*. Springer Nature, 2015.

[37] D. H. Dowell. Sources of emittance in RF Photocathode injectors: intrinsic emittance, space charge forces due to non-uniformities, RF and solenoid effects. *arXiv preprint arXiv:1610.01242*, 2016.

[38] T. W. Reynolds and E. A. Richley. Thermionic emission from cesium-coated electrostatic ion-thruster electrodes. Technical report, 1963.

[39] S. Nirantar et al. Electron emission devices for energy-efficient systems. *Advanced Intelligent Systems*, 1(4):1900039, 2019.

[40] W. E. Spicer. Photoemissive, photoconductive, and optical absorption studies of alkali-antimony compounds. *Physical review*, 112(1):114, 1958.

[41] D. H. Dowell and J. F. Schmerge. Quantum efficiency and thermal emittance of metal photocathodes. *Physical Review Special Topics-Accelerators and Beams*, 12(7):074201, 2009.

[42] K. J. Kim. RF and space-charge effects in laser-driven RF electron guns. *Nuclear Instruments and Methods in Physics Research Section A: Accelerators, Spectrometers, Detectors and Associated Equipment*, 275(2):201–218, 1989.

[43] H. J. Qian et al. Experimental investigation of thermal emittance components of copper photocathode. *Physical Review Special Topics-Accelerators and Beams*, 15(4):040102, 2012.

[44] M. Ferrario et al. Space charge effects. *arXiv preprint arXiv:1601.05214*, 2016.

[45] K. Flöttmann et al. ASTRA: A space charge tracking algorithm, 2011.

[46] COMSOL Multiphysics. https://www.comsol.com/acdc-module.

[47] A. Arnold et al. Development of a superconducting radio frequency photoelectron injector. *Nuclear Instruments and Methods in Physics Research Section A: Accelerators, Spectrometers, Detectors and Associated Equipment*, 577(3):440–454, 2007.

[48] J. Teichert et al. Status of the SRF gun operation at ELBE. Technical report, 2010.

[49] J. Teichert et al. Free-electron laser operation with a superconducting radio-frequency photoinjector at ELBE. *Nuclear Instruments and Methods in Physics Research Section A: Accelerators, Spectrometers, Detectors and Associated Equipment*, 743:114–120, 2014.

[50] A. Arnold et al. Commissioning results of the 2nd 3.5 cell SRF gun for ELBE. Technical report, Thomas Jefferson National Accelerator Facility (TJNAF), Newport News, VA (United States), 2014.

[51] M. Kuntzsch et al. Microtca. 4-based llrf for cw operation at ELBE–status and outlook. *JACOW*, pages 101–103, 2018.

[52] D. H. Dowell et al. Cathode R&D for future light sources. *Nuclear Instruments and Methods in Physics Research Section A: Accelerators, Spectrometers, Detectors and Associated Equipment*, 622(3):685–697, 2010.

[53] D. R. Lide. *CRC handbook of chemistry and physics*, volume 85. CRC press, 2004.

[54] H. J. Qian et al. Surface photoemission in a high-brightness electron beam radio frequency gun. *Applied Physics Letters*, 97(25):253504, 2010.

[55] R. Xiang et al. SRF Gun and SRF linac driven THz at ELBE successfully in user operation. In *19th International Conference on RF Superconductivity (SRF'19), Dresden, Germany, 30 June-05 July 2019*, pages 915–917. JACOW Publishing, Geneva, Switzerland, 2019.

[56] J. Kühn et al. A Cu photocathode for the Superconducting RF photoinjector of bERLinPro. In *9th Int. Particle Accelerator Conf.(IPAC'18), Vancouver, British Columbia, Canada*, 2018.

[57] S. H. Kong et al. Cesium telluride photocathodes. *Journal of applied physics*, 77(11):6031–6038, 1995.

[58] R. Xiang et al. Metal and semiconductor photocathodes in HZDR SRF gun. 2019.

[59] T. Kamps et al. Electron beam diagnostics for a superconducting radio frequency photoelectron injector. *Review of scientific instruments*, 79(9):093301, 2008.

[60] E. B. Carlsten. New photoelectric injector design for the Los Alamos National Laboratory XUV FEL accelerator. *Nuclear Instruments and Methods in Physics Research Section A: Accelerators, Spectrometers, Detectors and Associated Equipment*, 285(1-2):313–319, 1989.

[61] L. Serafini and J. B. Rosenzweig. Envelope analysis of intense relativistic quasilaminar beams in rf photoinjectors: mA theory of emittance compensation. *Physical Review E*, 55(6):7565, 1997.

[62] M. Ferrario et al. Direct measurement of the double emittance minimum in the beam dynamics of the sparc high-brightness photoinjector. *Physical review letters*, 99(23):234801, 2007.

[63] T. Rao and D. H. Dowell. An engineering guide to photoinjectors. *arXiv preprint arXiv:1403.7539*, 2014.

[64] H. Vennekate. Emittance compensation for SRF photoinjectors. 2017.

[65] M. E. Schulze. Spherical aberrations-final focus and solenoid scans. Technical report, Los Alamos National Lab.(LANL), Los Alamos, NM (United States), 2020.

[66] L. Walckiers. Magnetic measurement with coils and wires. *arXiv preprint arXiv:1104.3784*, 2011.

[67] C. Petrone. *Wire methods for measuring field harmonics, gradients and magnetic axes in accelerator magnets*. PhD thesis, CERN, 2013.

[68] E. Hall et al. On a new action of the magnet on electric currents. *American Journal of Mathematics*, 2(3):287–292, 1879.

[69] D. H. Dowell et al. Exact cancellation of emittance growth due to coupled transverse dynamics in solenoids and RF couplers. *Physical Review Accelerators and Beams*, 21(1):010101, 2018.

[70] J. Qiang et al. Beam dynamics simulation of the solenoid sextupole error in the LCLS-II injector. Technical report, SLAC National Accelerator Lab., Menlo Park, CA (United States), 2018.

[71] D. H. Dowell. Correcting emittance growth due to stray sextupole fields. *arXiv preprint arXiv:1810.00086*, 2018.

[72] H. Wiedemann. Particle accelerator physics: Basic principles and linear beam dynamics. *Berlin Heidelberg New York,*, 2003.

[73] S. G. Anderson et al. Space-charge effects in high brightness electron beam emittance measurements. *Physical Review Special Topics-Accelerators and Beams*, 5(1):014201, 2002.

[74] P. G. O'Shea et al. The University Maryland Electron Ring (UMER). *Nuclear Instruments and Methods in Physics Research Section A: Accelerators, Spectrometers, Detectors and Associated Equipment*, 464(1-3):646–652, 2001.

[75] S. R. Deans. *The Radon transform and some of its applications*. Courier Corporation, 2007.

[76] C. B. McKee et al. Phase space tomography of relativistic electron beams. *Nuclear Instruments and Methods in Physics Research Section A: Accelerators, Spectrometers, Detectors and Associated Equipment*, 358(1-3):264–267, 1995.

[77] D. Stratakis et al. Tomography as a diagnostic tool for phase space mapping of intense particle beams. *Physical Review Special Topics-Accelerators and Beams*, 9(11):112801, 2006.

[78] D. Xiang et al. Transverse phase space tomography using a solenoid applied to a thermal emittance measurement. *Physical Review Special Topics-Accelerators and Beams*, 12(2):022801, 2009.

[79] K. M. Hock et al. Beam tomography research at Daresbury Laboratory. *Nuclear Instruments and Methods in Physics Research Section A: Accelerators, Spectrometers, Detectors and Associated Equipment*, 753:38–55, 2014.

[80] K. M. Hock and A. Wolski. Tomographic reconstruction of the full 4D transverse phase space. *Nuclear Instruments and Methods in Physics Research Section A: Accelerators, Spectrometers, Detectors and Associated Equipment*, 726:8–16, 2013.

[81] M. Zhang. Emittance formula for slits and pepper-pot measurement. Technical report, Fermi National Accelerator Lab.(FNAL), Batavia, IL (United States), 1996.

[82] R. Ganter et al. Electron beam characterization of a combined diode rf electron gun. *Physical Review Special Topics-Accelerators and Beams*, 13(9):093502, 2010.

[83] T. L. Lai et al. Strong consistency of least squares estimates in multiple regression II. *Journal of multivariate analysis*, 9(3):343–361, 1979.

[84] S. B. Kotsiantis et al. Supervised machine learning: a review of classification techniques. *Emerging artificial intelligence applications in computer engineering*, 160(1):3–24, 2007.

[85] N. K. Kalantari et al. A machine learning approach for filtering Monte Carlo noise. *ACM Trans. Graph.*, 34(4):122–1, 2015.

[86] K. P. Murphy. *Machine learning: a probabilistic perspective*. MIT press, 2012.

[87] A. Ng et al. Sparse autoencoder. *CS294A Lecture notes*, 72(2011):1–19, 2011.

[88] M. Belkin et al. Reconciling modern machine-learning practice and the classical bias–variance trade-off. *Proceedings of the National Academy of Sciences*, 116(32):15849–15854, 2019.

[89] M. A. Kramer. Nonlinear principal component analysis using autoassociative neural networks. *AIChE journal*, 37(2):233–243, 1991.

[90] J. Zhu et al. High-fidelity prediction of megapixel longitudinal phase-space images of electron beams using encoder-decoder neural networks. *Physical Review Applied*, 16(2):024005, 2021.

[91] A. Paszke et al. PyTorch: An Imperative Style, High-Performance Deep Learning Library. In *Advances in Neural Information Processing Systems 32*. 2019.

[92] I. Goodfellow et al. *Deep learning*. MIT press, 2016.

[93] M. Krasilnikov et al. Experimentally minimized beam emittance from an L-band photoinjector. *Physical Review Special Topics-Accelerators and Beams*, 15(10):100701, 2012.

[94] S. Rimjaem et al. Optimizations of transverse projected emittance at the photo-injector test facility at DESY, location Zeuthen. *Nuclear Instruments and Methods in Physics Research Section A: Accelerators, Spectrometers, Detectors and Associated Equipment*, 671:62–75, 2012.

[95] P. W. Huang et al. Single shot cathode transverse momentum imaging in high brightness photoinjectors. *Physical Review Accelerators and Beams*, 23(4):043401, 2020.

[96] P. Murcek et al. The SRF photoinjector at ELBE–design and status 2013. In *MOP025, Proc. 16th Int. Conf. on RF Superconductivity, Paris, France*, 2013.

[97] Magnet-Physik Dr. Steingroever GmbH. *USB Hall probes*. Köln, 2008.

[98] SENIS magnetic & current measurement. *Fully integrated 3-Axis Hall Probe HL, HM, HS*. SENIS AG, Switzerland, 2017.

[99] E. Mihóková et al. Luminescence and scintillation properties of YAG: Ce single crystal and optical ceramics. *Journal of luminescence*, 126(1):77–80, 2007.

[100] R. Yang et al. Development of a YAG/OTR monitor for beam halo diagnostics. *Proc. of the IBIC2018, Shanghai, China*, pages 429–432, 2018.

[101] L. Zheng et al. Overestimation of thermal emittance in solenoid scans due to coupled transverse motion. *Physical Review Accelerators and Beams*, 21(12):122803, 2018.

Appendix A

Some symbols

ε_x, ε_y	beam normalized emittance in transverse planes
ε	beam geometric emittance
ε_{rms}	beam RMS emittance
ε_n	beam normalized emittance or beam RMS normalized emittance
$\Delta\varepsilon_{n,rf}$	beam additional normalized emittance increasing from RF field
$\Delta\varepsilon_{n,sc}$	beam normalized emittance from space charge
$\Delta\varepsilon_{sph}$	beam additional emittance from solenoid spherical aberration
$\Delta\varepsilon_{n,quad+sol}$	beam additional emittance from the quadrupole field in the solenoid
$\Delta\varepsilon^{E}_{roughness}$	the additional emittance from cathode surface roughness
$\Delta\varepsilon_{chro}$	beam additional emittance from chromatic aberration
e	basic unit of electrical charge
e	the total emittance error of slit-scan
e_0	the emittance error of slit-scan from slit width
e_1	the emittance error of slit-scan from beamlet space charge
e_2	the emittance error of slit-scan from slit position recording jitter
e_3	the emittance error of slit-scan from beamlet images center and RMS size uncertainty
e_4	the emittance error of slit-scan from beam energy uncertainty
λ_{min}	the minimally achievable radiation wavelength
p_x, p_y	particle transverse momentum components values in x and y directions
p_0	reference particle momentum value
p	particle momentum value
Δp	individual particle momentum difference from p_0
v	particle velocity
E	beam total energy
E	electric field value
E_{acc}	cavity average accelerated electric field
E_{kin}	beam kinetic energy
E_{rf}	the peak electric field of the cavity on axis
$\vec{E}$	electric field
$\vec{B}$	magnetic flux density, named as magnetic field in thesis

B_x, B_y	magnetic field components in x and y directions
B_{x0}, B_{y0}	bending field in x and y directions
B_s	solenoid longitudinal field maximum on axis
g	quadrupole field gradient
k	quadrupole focusing strength
k	quadrupole strength
K	focusing function
K	solenoid strength
d	drift distance from the quadrupole center to the screen
q	particle charge
$\vec{\kappa}$	the trajectory local curvature vector
$\kappa_{x,y}$	the trajectory local curvature components in x and y directions
$\rho_{x,y}$	the local bending radius of the trajectory
$\beta(z)$	beam transverse size amplitude at position z
$\theta(z)$	beam transverse size phase at position z
β, γ, α	Courant-Snyder parameters or Twiss parameters
β, γ	Lorentz factors
m_0	electron rest mass
c	speed of light
σ_u	beam RMS size, $\sqrt{\langle u^2 \rangle}$, u means x or y
σ_{laser}	laser spot RMS size
σ_{11}	$\langle u^2 \rangle$
σ_{12}	$\langle uu' \rangle$
σ_{22}	$\langle u'^2 \rangle$
σ_{px}	beam dimensionless RMS momentum
$\hbar\omega$	the photon energy
ϕ_{eff}	metal effective work function
C_s	solenoid spherical aberration coefficient
ϕ_e	the relative phase of the electron with respect to the RF waveform
σ_ϕ	bunch length in radian unit
X_g	the geometry factor related to the cathode roughness
ϵ_0	vacuum permittivity
μ_0	vacuum permeability
λ_0	bunch longitudinal charge density
a	uniform beam radius
σ_z	beam RMS longitudinal size
r_0	round beamlet radius
I_p	beam peak current
I_0	the characteristic current
Q	bunch charge
Q_0	cavity quality factor
f	quadrupole focusing strength
f_c	beam normalized emittance correction factor
f_{sol}	solenoid focusing strength
α_1, α_2	quadrupole field rotation angles
L	drift distance from the slit to the screen

L_s	solenoid effective length
L_{eff}	quadrupole effective length
θ	pole angle
ϕ	azimuthal angle
Φ_B	magnetic flux
$\mathcal{E}$	electromotive force
J	cost function
J_{dn}	dipole field normal component coefficient
J_{ds}	dipole field skew component coefficient
J_{qn}	quadrupole field normal component coefficient
J_{qs}	quadrupole field skew component coefficient
J_{sn}	sextupole field normal component coefficient
J_{ss}	sextupole field skew component coefficient
J_t	solenoid transverse field component coefficient
R_0	the ratio of the space charge term and the emittance term in beam envelope equation
R_b	the ratio of the space charge term and the emittance term in beamlet envelope equation
n_i	beamlet particle intensity
b	bias term in network layer
w	weight vector between network layers